A doctoral dissertation

Studies on inverse opal-structured titania with gold nanoparticles as novel design for photoabsorption-efficiency enhancement in photocatalysis

光吸収効率増大のための新規デザインとしての金ナノ粒子含有逆オパール構造酸化チタン光触媒に関する研究

Tharishinny Raja Mogan

Division of Environmental Materials Science, Graduate School of Environmental Science, Hokkaido University

2021

List of abbreviation

ALD	atomic layer deposition
DRS	diffuse reflectance spectroscopy
EDX	energy dispersive X-ray spectroscopy
FAAS	flame atomic absorption spectroscopy
HM	hydrothermal
PC	photonic crystal
PD	photodeposition
NP	nanoparticle
LV-SEM	low vacuum-scanning electron microscopy
TEM	transmission electron microscopy
UV	ultraviolet
XRD	X-ray diffraction
PBG	photonic band gap
LSPR	localized surface plasmon resonance
IOT	inverse-opal titania
IO	inverse opal
LED	light-emitting diode

Table of Contents

Chapter 1

General introduction

1-1 Heterogeneous Photocatalysis

1-1-1 Development in photocatalysis

Photocatalysis is defined as photochemical reactions that proceeds on a catalyst that absorbs light and remains unchanged throughout the process. Discovery on photocatalysis related studies was started in early 1920s when metallic Ag was formed on zinc oxide (ZnO) semiconductor, resulting from the photocatalytic deposition of a silver salt precursor [Baur 1924], followed by observation on photoinduced evolution of hydrogen peroxide (H_2O_2) from photo irradiated ZnO [Baur 1927]. However, the term of photocatalyst has not been defined and utilized except for the words as photosensitizer in most of the photocatalysis related studies [Ohtani 2014].

In the late 70s, oil crisis led to tremendous development of other energy sources, including photocatalysis studies. Subsequently, famous photochemical effect known as "Honda–Fujishima effect" was reported, i.e., promising electrochemical water splitting into O_2 and H_2 gaseous could proceed upon photoirradiation of TiO_2 electrode [Fujishima 1972], which has opened a wider scope in photocatalysis field. Later, studies have evolved to purify water through photocatalytic decomposition of pollutants, such as cyanide and sulphate by using various semiconductors, including ZnO, CdS, Fe_2O_3 and WO_3 [Frank 1977a / Frank 1977b]. Gradually, applications based on photocatalysis developed such as oxidative

photodecomposition of organic compunds [Fox 1993], water purification [Pelizzetti 1988] and also air purification [Peral 1992].

Among many semiconductors, titania (titanium (IV) oxide, TiO_2) has been considered as one of the most promising photocatalysts in hetergeneous photoctalysis field. One of the major drawbacks of TiO_2 is the limited light absorption, i.e., TiO_2 could be activated only under UV irradiation, which covers only 3-5% of solar spectrum. This drawback affected the potential of TiO_2 in energy production, despite its efficiency and stability, as compared to other semiconductors with narrower band gap, such as CdS and CdSe. In this regard, TiO_2 has been explored in applications that could use its limited ability of photoabsorption, such as photocatalytic cleaning material, as shown in **Fig. 1-1** [Honda 1998]. Apart from that, photocatalytic antibacterial effect by TiO_2 has been observed [Matsunaga 1985 / Sunada 2003] and broadly applied. The wonders of TiO_2 as photocatalyst go on in self-cleaning and anti-fogging applications, due to its wettability and superhydrophilicity [Fujishima 1999].

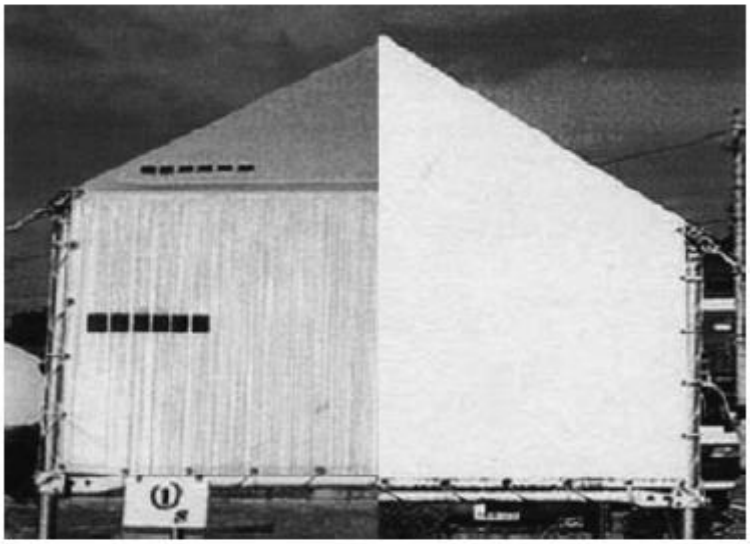

Fig. 1-1. Image of ordinary tent (left) and tent coated with TiO_2 (right) showing the effectiveness of the self-cleaning ability by TiO_2 photocatalyst.

Over the years, many studies have been carried out on TiO_2 to improve efficiency of light harvesting. Introduction of other elements, such as metals, non-metals, metal oxides and also modification of TiO_2 structure itself are the alternative pathways that have been effective. Along that line, nitrogen (N) doping has been found to support TiO_2 in light-harvesting at 400 nm – 530 nm, although the photocatalytic activity has been reported not to be high enough as compared to that under UV irradiation [Asahi 2001]. Other non-metal dopants such as carbon

(C) and sulphur (S), have been also reported as visible active photocatalysts [Umebayashi 2003].

1-1-2 Principle of photocatalysis

The basic theory of photocatalysis could be defined by the band model, as shown in **Fig. 1-2**, which could represent the electronic structure of most semiconductors. There are two main aspects that drive the overall photoreaction which are photoabsorption, i.e., bright-part and chemical reactions that proceed after the photoexcitation of charge carriers, i.e., dark-part. The photocatalyst materials absorb photon with an energy of equal or greater than the existing band gap (forbidden-band) to be able to witness an electron in electron-filled valence band (VB) to be excited by overcoming the band gap, subsequently leaving a positive hole in the VB. Those charge carriers drive the oxidation and reduction reactions simultaneously for the compounds that are adsorbed on the photocatalyst surface. Along these, recombination of charge-carries could take place, which becomes one of the drawbacks of semiconductor photocatalyst. The rate of recombination process is reported to take place in fast manner, about 10 ns-100 ns in TiO_2 photocatalyst, which affects the overall photocatalytic activity performance [Hoffmann 1995].

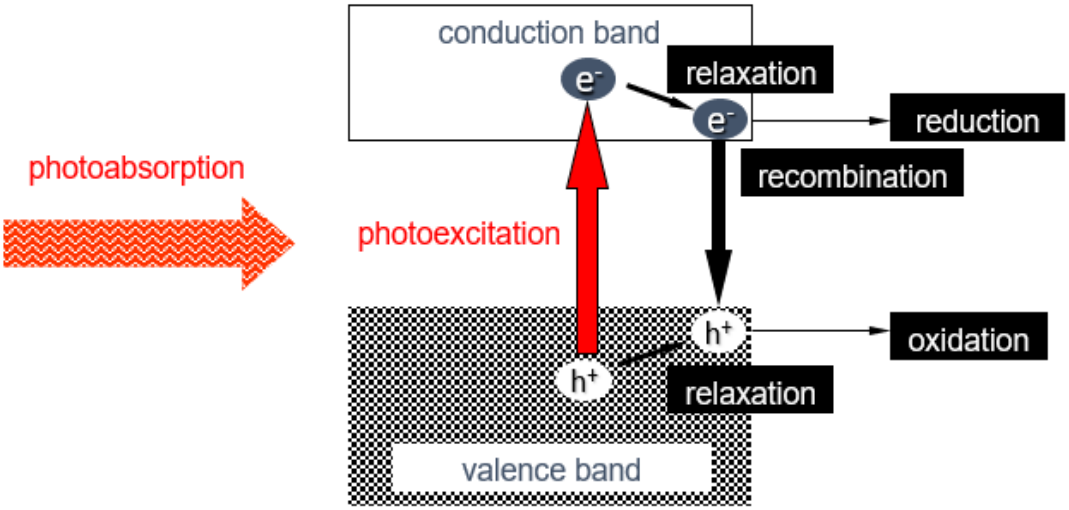

Fig. 1-2. General principle of photocatalysis.

The overall efficiency of reactions under photoirradiation is, therefore, a product of efficiencies of photoabsorption and utilization of the excited states for chemical reaction, i.e., quantum efficiency. In order to improve the apparent quantum efficiency, the drawbacks of photocatalyst such as lack of visible light absorption and recombination of charge-carriers in TiO_2 have been proposed by many alternatives. For example, many dark-part designs have been reported, including doping [Zheng 2016] and utilization of surface modification [Kowalska 2012 / Islam 2018] to enhance the photocatalytic activity**.**

Somehow very less attention has been given on the aspect of photoabsorption efficiency. The term could be defined as the ability of the photocatalyst itself to absorb significant amount of incident photons upon the irradiated light intensity. In the general cases, not all the incident photons could be absorbed by the photocatalyst material as the light intensity might be reduced upon reaching the material [Ohtani 2010]. Photoabsorption efficiency is an important aspect to be considered in light harvesting process as the ability of the photocatalyst to absorb photons is directly correlated to the quantum yield and the photocatalytic performance. It is expected that photocatalyst with a good photoabsorption efficiency could give significant photocatalytic performance and enhancement in light harvesting could be evident.

1-2 Titania polymorphs in photocatalysis

As introduced earlier, TiO_2 is one of the most famous and widely studied photocatalysts. Titania is naturally occurring oxide of titanium, including anatase, rutile and brookite polymorphs. However, in nature, various mixtures of titania could be found, e.g., ilmenite (a black iron-titanium oxide with a chemical composition of $FeTiO_3$, commonly used for titania synthesis via sulfate method), rather than its pure crystals. Titania has been used extensively in our daily life, i.e., as a pigment, in textile and paper industry, food, drugs, cosmetics and as a photocatalysts.

Two main polymorphs of titania, i.e., anatase and rutile, have been extensively investigated both for photocatalysis and other applications (pigments, sunscreen creams), and recently, the high photocatalytic activities of brookite have been also reported [Kandiel 2010 / Di Paola 2013]. Anatase and rutile belong to tetragonal system whereas brookite to

orthorhombic one. Rutile is known as the most abundant and thermodynamically stable polymorphs of TiO_2, widely used in pigments and cosmetic products, mainly due to its high refractive index. In contrast, anatase and brookite are metastable, and thus thermal treatment results in their phase transition into rutile. The properties of TiO_2 polymorph has been presented in **Table 1-1**.

Anatase has been commonly reported as the most photocatalytically active form of titania, and thus mainly investigated and used for many photocatalytic reactions. Various reasons of its higher activity than other phases (including amorphous titania) have been proposed, such as wider bandgap (and thus high oxidation and reduction ability), lower content of defects, higher content of hydroxyl groups on the surface, higher mobility of charges (i.e., mainly electrons), lower content of deep electron traps (ETs; and thus, lower rate of charge carriers' recombination). It should be also mentioned that usually anatase has much larger specific surface area than rutile (higher temperatures of rutile preparation results in NPs' sintering and aggregation), and thus larger content of adsorption sites for reacting molecules on its surface has been also proposed as another reason of its high photocatalytic efficiency.

The comparison of 35 titania photocatalysts showed that the photocatalytic efficiency did not depend only on the titania properties (specific surface area, polymorphic composition, defects' content, crystallite and particle sizes), but also on the kind of photocatalytic reaction [Prieto-Mahaney 2009]. Accordingly, it has been proposed that: (i) large particle size results in efficient oxygen evolution, (ii) large specific surface area (small crystallite and particle sizes) in methanol dehydrogenation, (iii) anatase presence in oxidative decomposition of acetic acid, (iv) rutile presence and defects' content in oxidative decomposition of acetaldehyde, and (v) rutile presence in synthesis of pipecolinic acid. Moreover, it should be pointed that rather mixed-phase than single-phase titania photocatalysts have been used in photocatalysis (as pure phase samples are rather rare), and thus the impact of the minor phase on the overall activity cannot be omitted. Interestingly, "phase-mixed" titania samples have been proposed as more active than single phase samples [Oyama 1996 / Ohno 2003].

Table 1-1. Properties of titania polymorphs.

		rutile	anatase	brookite
atomic spacing (Å) [a]		a = 4.596 c = 2.958	a = 3.793 c = 9.51	a = 5.456 b = 9.182 c = 5.143
axial ratios		a:c = 1:0.64388	a:c = 1:2.50725	a:b:c = 0.5942:1:0.5601
molecule/unit cell [a]		2	4	8
density (g cm^{-3}) [a]		4.25	3.88	4.12
crystal system [a]		tetragonal-(ditetragonal dipyramidal)	tetragonal (ditetragonal dipyramidal)	orthorombic-(dipyramidal)
bandgap (eV)		3.02 [d]	3.23 [d]	3.14 [e]
absorption edge (nm)	calculated [b]	410	384	395
	measured [c]	413 [f]	388 [f]	395 [e]

a - data from webmineral.com; b – calculated from bandgap energy; c – experimentally estimated from absorption spectra; d-f – exemplary data (might slightly differ depending on properties): d –[Rao 1980]; e – [Gratzel 1985] ; f – [Yang 2004]

1-3 Titania nanostructures: Zero-, one-, two- and three-dimensional structure

Titania and other nanomaterials could be classified according to their dimension confinement in nanoscale (< 100 nm) measurement, and thus 0-dimensional (0D) might be referred to NPs, and nanospheres, whereas 1D and 2D have one and two dimensions larger than 100 nm, e.g., nanotubes and nanoplates, respectively. The structures with repeated bulk arrays could be designed as 3D titania, where none of their dimension is confined to nanoscale, except for their inner structure, e.g., composed of fine NPs, nanovoids, etc. Based on this concept, various types of titania nanostructures have been designed and reported.

1-3-1 Zero-dimensional titania

Titania NPs, nanospheres, nanorods, nanorice NPs have been commonly used for photocatalytic reactions. Here, two kinds nanostructures are shortly described, i.e., core-shells and faceted NPs. Core-shell titania nanostructures belong to titania composites, i.e., titania and

other materials as mixed-phase composites. There are two main reasons for preparation and usage of core-shells in photocatalysis, i.e., (i) reusability and (ii) enhanced activity. Although nanoparticulate titania is highly recommended for application, due to high activity (large specific surface area), the separation of suspended photocatalyst might be costly (ultrafiltration). Therefore, photocatalyst supports, e.g., steel plates, molecular sieves, glass plates, Raschig rings, zeolites, activated carbon and silica [Brigden 2001 / Zielinska-Jurek 2017], have been applied. Glass microspheres, recovered from fly ash were also used as titania support, and interestingly higher activity was found for phenol degradation on microsphere/titania despite much lower surface area than that of particulate titania samples [Hupka 2006 / Kowalska, 2004]. It was proposed that composition of microsphere (the presence of Fe_2O_3) could influence the overall activity, i.e., the possible transfer of charges (both electrons and holes) from titania to Fe_2O_3 hindering charge carriers' recombination. However, it should be pointed that there is a risk that titania support might be mechanically destroyed during photocatalytic tests (pumps, stirrers, etc.), as has been observed for these microspheres [Hupka 2006 / Kowalska 2010. Therefore, mechanically stable core has been proposed, such as magnetic Fe_3O_4, which additionally allows fast and easy separation of photocatalyst after reactions in the magnetic field [Zielinska-Jurek 2017 / Wysocka 2018]. However, the photoreaction between a core and a shell might result in instability of photocatalyst (e.g., dissolution of iron), and thus an insulator interlayer has been applied between a magnetic core and titania shell.

The concept of titania synthesis as crystals with specific facets has been a hot research topic, especially since 2008 when Yang et al. prepared anatase crystals with large percentage of reactive {001} facets [Yang 2008]. Earlier in 1998, Vittadini et al. theoretically predicted the exceptional dissociative adsorption of water on anatase {001} surface [Vittadini 1998]. It is known that the reactivity of photocatalysts is strictly connected with a surface atomic arrangement and coordination what determines the adsorption of reactant molecules, surface transfer between photoexcited electrons and reactant molecules, and finally desorption of product molecules. Arrangement of crystal facets with different orientations changes the surface atomic arrangement and coordination, influencing the photocatalytic activity [Liu 2011[. Pertaining to this, crystal facets engineering might be the solution how to improve the usually poor selectivity of heterogeneous photocatalytic transformations by minimization of dispersity of surface atomic structure [Kou 2017]. Main crystal shapes of anatase, rutile and brookite are presented in **Fig. 1-3.**

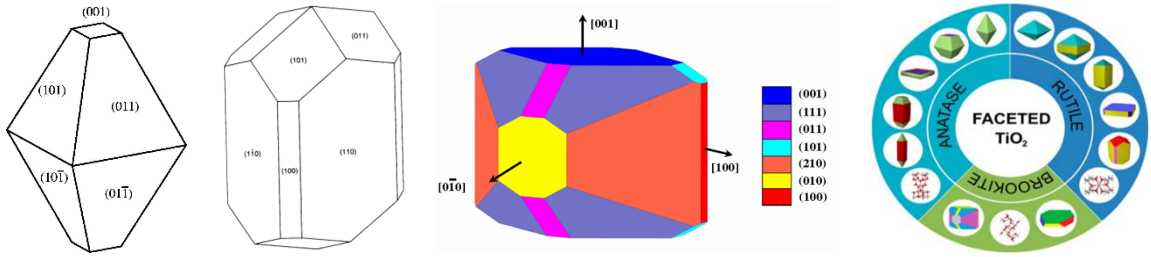

Fig. 1-3. Equilibrium crystal shape of: (**a**) anatase (adapted with permission from [Lazzeri 2001]. Copyright American Physical Society, 2001); (**b**) rutile (adapted with permission from [Ramamoorthy 1994]. Copyright American Physical Society, 1994); (**c**) brookite (adapted with permission from [Gong 2007]. Copyright American Physical Society, 2007); (**d**) Main crystal shapes of titania (adapted with permission from [Liu, 2014]. Copyright American Chemical Society, 2014

One of the most important properties resulting from the presence of different predominant crystal facets is photocatalytic activity connected with synergistic effects of different facets. Majority of studies reported that photocatalytic activity of anatase crystals in the reaction of oxidation of organic compounds increased with an increase in the percentage of {001} facets [Han 2012]. It has been proposed that coexistence of different crystal facets, e.g. {101} and {001}, might result in enhanced activity, due to the synergistic effects between different facets. First, in the early studies, Ohno et al. reported selective photodecomposition of Pt and PbO_2 particles on different facets of anatase and rutile crystals [Ohno 2002]. They postulated the existence of oxidation and reduction sites on {001} and {101} facets of anatase, and {011} and {110} facets of rutile, respectively.

Although, DAP particles showed extremely high photocatalytic activity for both oxidation and reduction reactions (even higher than famous P25) [Janczarek 2016], single-facet titania seems to be very attractive for mechanism study. For example, octahedral anatase particles (OAP) with eight {101} facets showed very high photocatalytic activity for oxidation of acetic acid [Wei 2015 / Wei 2014] Although, various reports have claimed that faceted morphology was beneficial for photocatalytic activity, the direct proof was not presented till study by Wei et al. [Wei 2015 / Wei 2014]. In that study, OAP-containing samples, which differed only by morphology (same specific surface area, crystalline size, crystallinity,

composition, etc.), i.e., the content of faceted particles in the final product, were prepared by hydrothermal-ultrasonic reaction. Indeed, it was proved that faceted morphology was beneficial since with an increase in the content of faceted NPs, activity increased. Moreover, it was proposed that faceted NPs contained larger content of shallow than deep electron traps (ETs), which facilitated electrons' migration instead of their permanent trapping, as assumed by photoacoustic spectroscopy (total content of ETs) and time-resolved microwave conductivity (electron mobility and lifetime; shallow ETs) [Wei 2015].

1-3-2 One-dimensional titania

Titania nanotubes, nanowires, 1D-oriented nanopores and other 1D nanostructures have been extensively investigated for various applications, including solar cells, photocatalysis, batteries, filtration membranes, biomedical use and as templates for synthesis of other nanostructures [Kowalski 2013/ Kowalski 2010 / Mazierski 2017] Kasuga et al. were probably first who prepared titania nanotubes (TNTs) by chemical method [Kasuga 1999], whereas Imai et al obtained TNTs in porous alumina membrane by a deposition technique [Imai 1999]. Since then, huge effort has been put on preparation of highly-uniform and well-oriented TNTs. The most famous and popular is probably preparation of TNTs by electrochemical method, i.e., anodization of titanium film, started by Grimes and Schmuki [Gong 2001 / Beranek 2005 / Balaur 2005]. It should be pointed that different morphologies could be obtained by changing of conditions of anodization, e.g., TNTs, and mesoporous and nanoporous structures, as shown in **Fig. 1-4.** Recently, very interesting approach has been proposed by Zaleska-Medynska group, i.e., anodization of titanium alloys to prepare modified titania by one-step reaction, e.g., $TiO_2/Ag_2O/Ag$ [Mazierski 2017] and TiO_2/Cu_xO_y [Kozak 2018] from Ti/Ag and Ti/Cu alloys, respectively.

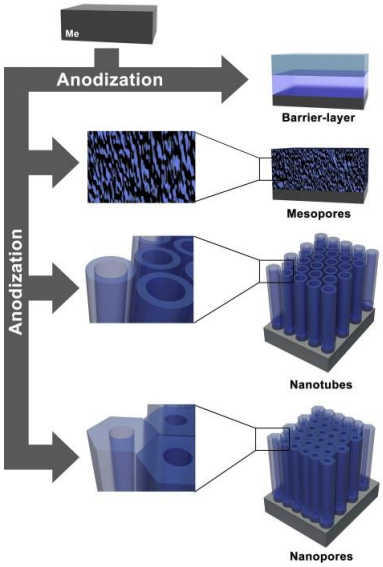

Fig. 1-4. Different morphologies of metal oxides obtained by metal anodization, adapted with permission from [Kowalski 2013].

TNTs photonic crystals (PCs) is presented as novel and not-well explored titania nanostructures. Designing of PCs, periodic optical nanostructures that affect the motion of photons, have been identified as an efficient method to enhance light harvesting, i.e., by using longer wavelengths (vis and IR). Uniqueness of PCs arises from the consistent spatial periodicity of the refractive index (n) in the well-ordered structure, which prevents the electromagnetic wave pathway at certain frequencies resulting in the formation of the stop band and the photonic band gap (PBG) [Yablonovitch 1993]. The presence of PBG results in formation of "slow photons" at the both red and blue edges of PBG (as illustrated in **Fig. 1-5**), whereby the photons are scattered and reflected causing the reduction of photons' group velocity [Yablonovitch 1993 / Lopez 2003, which might be utilized for light absorption enhancement in TiO_2 based photocatalysts.

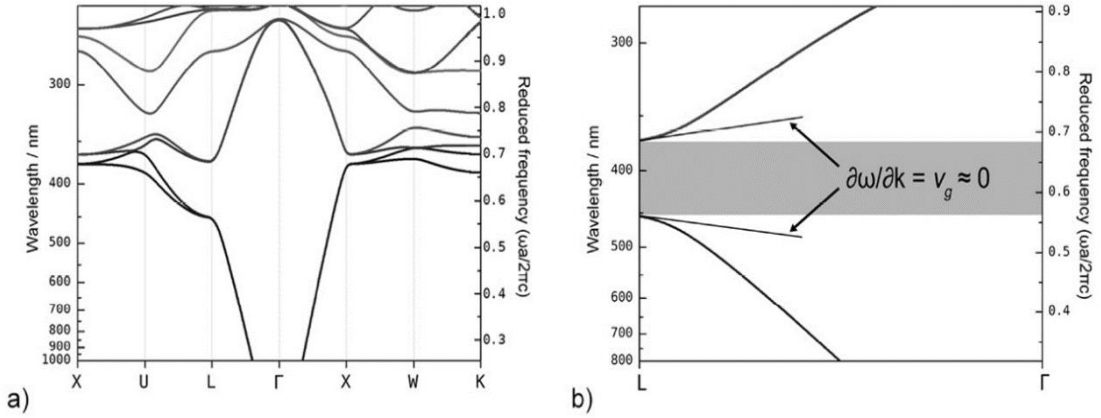

Fig. 1-5. Photonic band structure of TiO_2 inverse opal [Curti 2015].

Although, PCs are usually designed as 3D nanostructures (e.g., opal and inverse opal), TNT-PCs have been also reported [Kim 2017 / Chiarello 2016] TNT-PCs have been prepared by applying basic electrochemical anodization methods by alternating current and voltage, e.g., anodic oxidation [Kim 2017] or two-step anodization [Zhang 2014 / Li 2016]. The preparation techniques is critical for TiO_2-based PCs, e.g., the roughness of the Ti foil before anodization has affected the light absorption properties, which are directly related to the periodic modulation properties [Kim 2017 / Zhang 2014]. The smoothness of the material surface after anodization would reflect the unique formation of PCs, observed by the appearance of various shiny colours, as illustrated in **Fig. 1-6 (a)** [Zhang 2014]. TNT-PCs have been designed and explored in terms on the enhancement of the light harvesting. Many parameters of their preparation have been investigated, especially in consideration of the correlation between the photocatalytic activity and the PBG effects. For example, bamboo-like TNT-PC arrays with different nodes' lengths were designed by adjusting and maintaining the applied voltage, as shown in **Fig. 1-6 (b-c)** [Kim 2017]. Interestingly, it was found that PBG was bathochromic shifted with shortening of TNT. Moreover, Chiarello et al. reported that PBG position was directly related to the diameter of TNT, distance between each nanotube and their thickness [Chiarello 2016]. It was concluded that the PBG positions shifted to longer wavelengths with an increase in diameter of TNTs, resulting in an enhanced photogeneration of hydrogen.

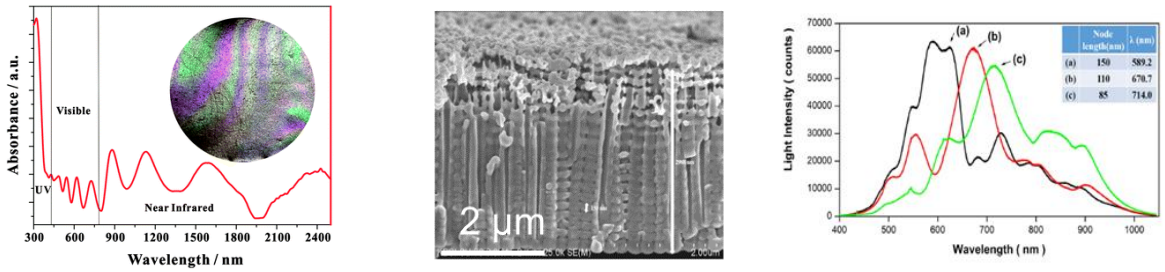

(**a**) (**b**) (**c**)

Fig. 1-6. Characteristics of TNT-PCs: (**a**) UV-vis-NIR diffuse reflectance absorption spectra, the inset presents a digital photograph of the TNT-PCs; adapted with permission from [hang 2014]. Copyright RSC, 2014.; (**b**) FE-SEM image and (**c**) diffraction spectrum of TNT-PCs arrays (prepared TiO_2 with different node lengths); adapted with permission from [Kim 2017]. Copyright Elsevier, 2017.

1-3-3 Two-dimensional titania

It is probable that 2D titania nanostructures, such as nanofilms, nanoplates, nanosheets, and nanobelts are the least examined for photocatalysis among all others, especially comparing with a huge number of studies on particulate titania (0D), titania nanotubes (1D), and 3D titania nanostructures. The investigations on 2D nanostructures have been intensively growing in recent years, especially for solar energy conversion, e.g., with C3N4, MoS2, and graphene-like materials (graphene, graphene oxide, reduced graphene oxide), due to their relatively large surface area, fast transfer of charge carriers to the photocatalyst surface, and thus low recombination of charge carriers, and thus high photocatalytic activity. Although various materials have been prepared as 2D nanostructures, 2D titania nanostructures have been rarely prepared and reported. Of course, films of titania have been intensively studied and commercially applied (self-cleaning, antifogging, and antiseptic materials), but these are not 2D “nano” structures.

Although well-organized titania nanostructures might be easily obtained by a convenient hydrothermal method, such as nanowires (1D), nanotubes (1D), and faceted NPs (0D), other methods are used for the preparation of 2D titania nanostructures since titania films are usually deposited on some supports, such as glass, polyvinyl chloride, and quartz. Therefore, chemical vapor deposition (CVD) [Campbell 1992], plasma-enhanced chemical

vapor deposition (PECVD) [Malinowska 2003], dc-sputtering [Subrt 2017], anodization and successive-ionic-layer-adsorption-and reaction (SILAR) [DeSario 2013] methods have been proposed for the preparation of 2D titania photocatalysts.

1-3-4 Three-dimensional titania

1-3-4-1 Titania aerogels

Titania aerogels are very interesting nano/microstructures, due to low density, porosity, high pore volume and large specific surface area [Campbell 1992 / Malinowska 2003 / Subrt 2017]. Despite they are commonly composed of NPs of titania, the resultant aerogel structure is much larger, and thus titania aerogels might be classified as 3D structures. Titania aerogels have been proposed as efficient photocatalysts with activities similar to that by P25 [Malinowska 2003]. Plasmonic photocatalysis, heterogeneous photocatalysis under vis irradiation on wide bandgap semiconductor (usually titania) modified with plasmonic NPs, such as gold, silver and copper (metals with localized surface plasmon resonance at vis range of solar spectrum), has been hot topic recently. Although, plasmonic photocatalysts showed activity at broad irradiation ranges for various reactions, the mechanism has not been clarified yet. Two main mechanism of plasmonic photocatalysis have been considered, i.e., energy and charge (usually electron) transfer. Accordingly, two kinds of titania aerogels have been prepared, i.e., with 5-nm gold NPs incorporated (3D Au-TiO_2) or not (Au/TiO_2) inside the 3D titania aerogel network, as shown in **Fig. 1-7** [DeSario 2013 / Panayotov 2013]. Interestingly, it was found that 3D Au-TiO_2 possessed much higher activity than simple deposited gold on the surface of titania aerogel (Au/TiO_2), suggesting that direct contact (interface) between gold and titania were crucial. Although authors discussed the possibilities of both mechanisms, the key-factor of morphology (gold position inside the aerogel resulting in large interface of gold-titania) might suggest that the charge transfer mechanism, i.e., “hot” electron transfer from gold to CB of titania, is predominant mechanism in the case of gold-titania plasmonic photocatalysts under vis irradiation.

(**a**) (**b**)

Fig. 1-7. Schemes showing titania aerogels (blue) with gold NPs (yellow dots): (**a**) incorporated inside the titania network (3D Au-TiO_2); and (**b**) deposited on the surface of titania aerogels (Au/TiO_2); drawn based on references [DeSario 2013 / Panayotov 2013].

1-3-4-2 Inverse-opal photonic crystals

There have been various nanostructures of PCs been designed and explored, including one-dimensional (1D), e.g., titania nanotubes-PC [Kim 2017 / Chiarello 2016], two-dimensional (2D) and three-dimensional (3D), e.g., opal PCs and inverse opal PCs (IO-PCs). In the most of the 1D PCs preparation methods, electrochemical methods including one- and two-step anodization are opted as the effective ways [Zhang 2014 / Li 2016] as the formation and properties of PCs dependent on the formation procedures. For instance, bathochromic shift of PBG has been observed after shortening the distance between adjacent nanotubes apart from increase in their diameter [Chiarello 2016].

2D and 3D PCs have been intensively examined in the recent years due to many advantages of the obtained meso/macro porous structures, such as large specific surface area, tunable porosity, and thus efficient mass transport [Likodimos 2018 / Li 2016]. The term of IO is used as unique structures comprise the exact replica structure obtained by using the opal as a template, as shown in **Fig. 1-8**. In this study, focus has been directed in exploration using titania based IO-PCs.

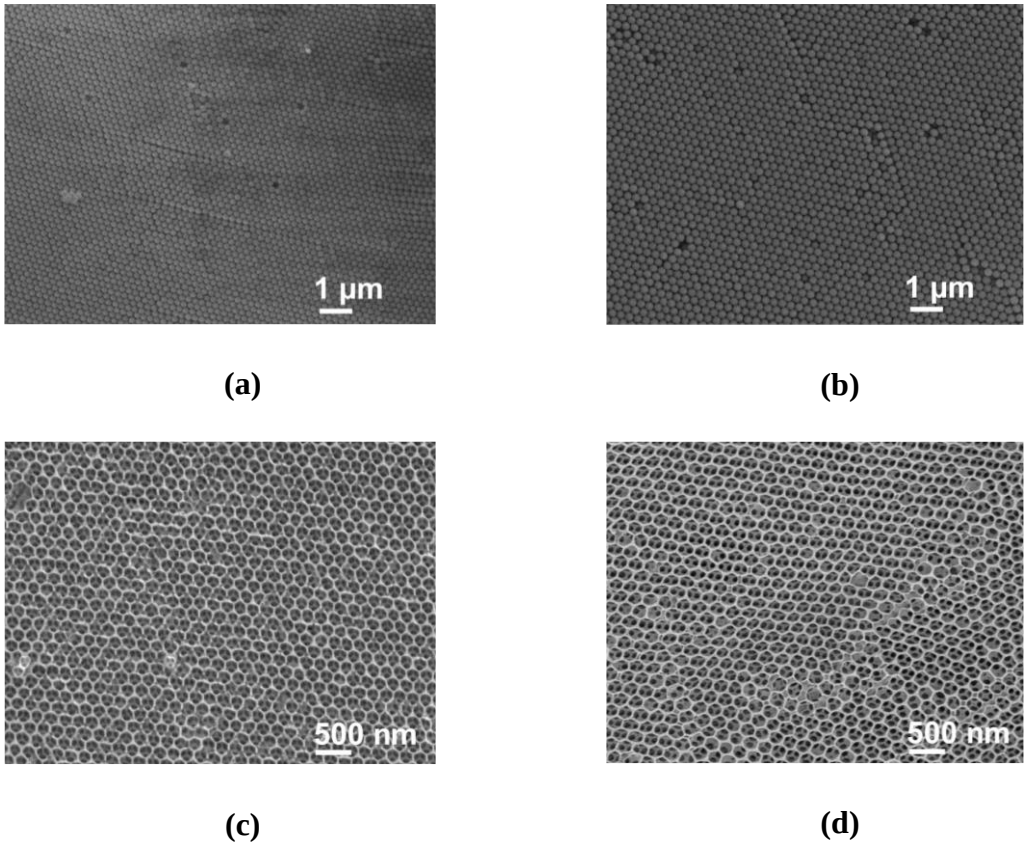

Fig 1-8. SEM images of opal (polystyrene (PS) spheres) and IO titania structures: (**a-b**) PS opal with: (**a**) 200-nm and (**b**) 250-nm sphere sizes, and (**c-d**) replicated titania IO films with: (**c**) 180-nm and (**d**) 207-nm voids; adapted with permission from [Zhang 2019]. Copyright 2018 Creative Commons Attribution.

The IO-PCs are usually fabricated in the three-step procedure, i.e., (i) formation of opal, i.e., colloidal crystal structure (template) by self-assembly of colloidal particles, (ii) infiltration of titania precursor (or titania) into the interstitial voids of opal, and (iii) the removal of sacrificial template (opal). All steps are highly critical and vital to avoid the formation of any cracks and defects [Lu 2012 / Jiang 1999] for the good quality which directly depicts the optic properties of IO-PCs.

Various colloidal particles have been used for the formation of opal (i), i.e., template such as silica (SiO_2), polystyrene (PS) and polymethyl methacrylate (PMMA). Monodispersity of the formed colloidal particles is the most essential criteria as larger variations than 5% in the size/shape inhibits the opal formation [Mayoral 1997]. The variety in the sizes and shapes of particles would result in disordered arrangement, which affects the quality of opal and IO

structures. In contrast, some reports have claimed that polydisperse large SiO_2 particles could also form close-packed arrays under negative pressure [Zhang 2017 / Zhang 2008]. However, it should be pointed that for optical applications of opal and IO-PCs, monodispersed colloidal particles are the most recommended. The self-assembly process is performed by few methods, including the vertical capillary deposition [Kubrin 2016 / Curti 2018 / Zhang, 2019] and spin coating [Kim 2013] for 2D PCs formation whereas sedimentation [Zhao 2005] and centrifugation-assisted sedimentation [Hua 2017] mainly for 3D opal formation. It was reported that SiO_2 opal was opted to has better robustness compared to other materials in terms of the assembly growth on the substrates [Zhao 2012]. The detachment of the material and substrate less likely to happen and the infiltration of targeted precursor could be done efficiently which could minimize the formation of cracks and defects. Following the fabrication of opal, post-thermal operation such as drying or/and calcination process have been proposed to improve the mechanical stability and enable the neck formation between the particles to aid the infiltration in the next step [Miguez 1998].

It has been considered that second step is the most difficult and critical, i.e., to impregnate opal with titania or targeted material, obtaining the stable IO structure. Various methods have been used for this step, e.g., drop casting and capillary force [Zhang 2019], vacuum infiltration [Jovic, 2016], atomic layer deposition (ALD) [Cheng 2012 / Liu 2011], spin-coating [Li 2018] and chemical vapor deposition (CVD) [Moon 2009]. A slightly different approach was taken by [Chen 2010] by soaking the PS opal powder in methanol prior introducing the TiO_2 viscous precursor via the aid of vacuum force. The step to utilize the organic solvent was taken as methanol owns a higher vapor pressure thus would give an easy pathway for the concentrated TiO_2 precursor to replace the methanol as the solvent gradually evaporate in the vacuum environment. Crystallization of the targeted material is carried out once the infiltration process takes place to convert the amorphous phase to either anatase or rutile polymorph. In the normal cases, ca. 15-30% shrinkage of the structure is observed due to the heat treatment, and thus resulting pore size reduction [Curti 2017 / Sordello, 2011]. Despite the fact that cracks formation quite hardly to be prevented, [Kubrin 2016] reported that the empty cracks could allow penetration of template particles and TiO_2 precursor in subsequent deposition as more cycles took place which may enhance the mechanical stability of the structure rather than presence of pure empty cracks. Apart from that, cracks also could be rectified during the infiltration of TiO_2 which the type of targeted material plays a major role. [Curti 2018] had successfully reduce the width of crack from 5 µm to 3 µm by changing

the infiltration method by using liquid precursor to TiO_2 nanoparticles suspension by reducing the formation of compact overlayer [Curti 2017]. It was also reported that ALD method for TiO_2 infiltration on opal structure could minimize the formation of cracks compared to usual sol gel method [Cheng 2012].

The final step (iii) of the template removal might be performed by calcination (for polymers) [Zhang 2019] or usage of highly concentrated base and acid such as sodium hydroxide and hydrofluoric acid treatments respectively for SiO_2 template etching [Zhao 2012].

PBG positions of IO PCs could be tuned and differ in many circumstances, e.g., the nanovoid diameter, the angle of the light irradiation and the overall refractive index comprising the targeted material, TiO_2 (as the high dielectric medium) and void's medium. Hence, tuning of the PBG according to the need of the application might be performed by altering these three aspects. All these factors could be summarized and explained in terms of the modified Bragg's Law which could be applied for (*111*) planes from the first order diffraction as follows:

$$\lambda_{max} = (8/3)^{1/2} D (n^2_{eff} - \sin^2 \theta)^{1/2}$$

where λ_{max} is the wavelength of stop band maximum, D is the diameter of the void, n_{eff} is the effective refractive index, and θ is the angle between the incident and the reflective surface.

Hence, based on this law, theoretical PBG position could be calculated for the titania IO based PCs. For instance, the shift of PBG towards shorter wavelengths has been observed (**Fig. 1-9**] after the reduction in nanovoid diameter due to increase in the calcination temperature [Wu 2014]. The author reported that even at high such as 900°C and 1000°C, the PBG bands could still evident indicating the existence of the periodic structure and the overall IO has not been destroyed. The overall refractive index could be altered depending on the environment of the IO samples system. As reported by [Curti 2017], PBG position is shifted to longer wavelength when the IO sample is immersed in water compared to the same sample measured in air system as shown in **Fig. 1-10**. In addition, the calculated stop band regions for IO-264 in both systems is almost in agreement to the PBG peaks measured via reflectance spectra which was about 455 nm and 400 nm respectively.

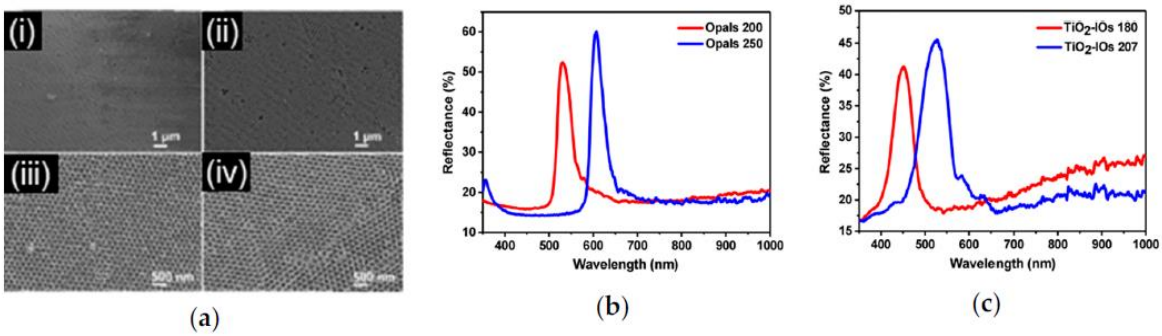

Fig. 1-9. Characteristics of opal (polystyrene (PS) spheres) and inverse opal (IO) titania structures: (**a**) FESEM images of PS opal with: (i) 200-nm and (ii) 250-nm sphere sizes, and replicated titania IO films with: (iii) 180-nm and (iv) 207-nm voids; reflection spectra of: (**b**) PS templates and (**c**) titania IOs; adapted with permission from [Zhang, 2019]. Copyright 2019 Creative Commons Attribution.

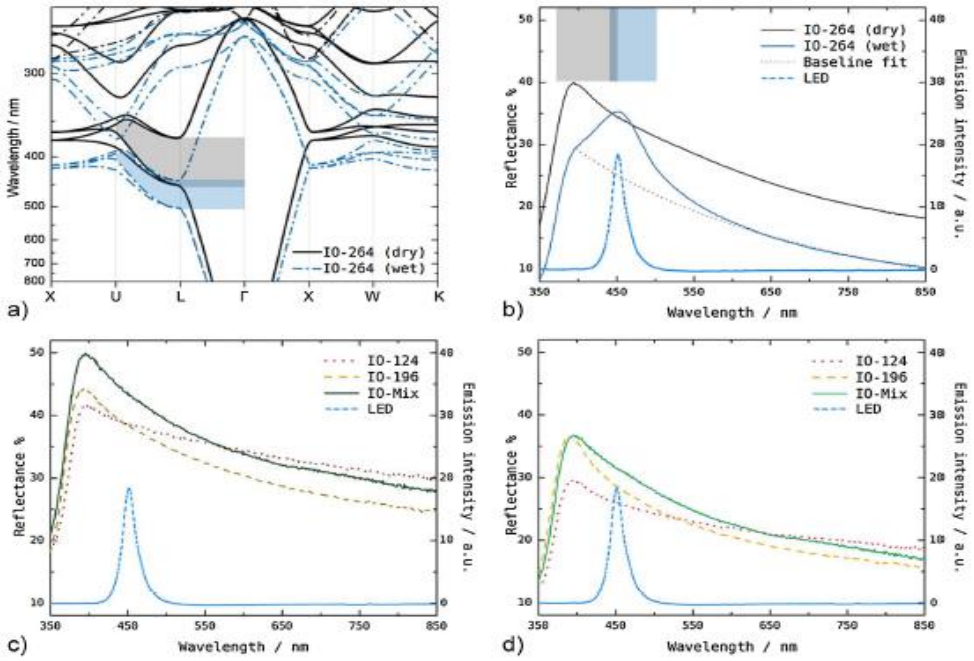

Fig. 1-10. Plots of (a) Calculated photonic band diagram of IO-264 in air and water systems (b) Diffuse reflectance UV–vis spectra of an IO-264 sample in air (c) Diffuse reflectance UV–vis spectra of IO-Mix, IO-196, and IO-124 samples in air. (d) Diffuse reflectance UV–vis spectra of IO-Mix, IO-196, and IO-124 samples in water.

Several reports have reported on how the nanovoid diameter could be related to the PBG bands and photocatalytic activity. For instance, it has been reported that for structures with the largest voids of 610 nm, reduction in velocity of photons and inhibited charge carriers' recombination have been the most evident [Wan 2019] resulting better photocatalytic activity performance compared to TiO_2 IO with smaller nanovoid. In contrast, the smallest voids have been reported as the most active, giving the highest photoelectrochemical enhancements in the case of titania IO sensitized by CdS quantum dots [Cheng 2012]. Therefore, the resultant photocatalytic activity might depend not only on nanovoid diameter, but also on other factors, including porosity, specific surface area and kind of co-modifications. In contrast to this report, [Jovic, 2016] did not conclude on the direct relation between the nanovoid and the photocatalytic activity. However, the overlapping between the electron band gap of TiO_2 anatase and red edge wavelength of PBG gave rise to the slow photon effect thus enhanced the activity compared with other IOs with different nanovoids and PBG [Curti 2017]. Similar agreement could be achieved in terms of the precise matching on the red edge of PBG and electronic absorption of TiO_2 as reported by [Rahul 2015]. In brief, 100% of RhB dye could be degraded only in 2 minutes by TiO_2 IO-215 film when PBG red-edge matches the TiO_2 electronic band absorption at 480 nm due to the enhanced photoabsorption ability compared to PBG position that located further apart at 850 nm.

Apart from nanovoid diameter, the slow photon effect could be realized by the change in angle of irradiation. In the usual cases, hypsochromic shift of PBG would be realized as the irradiation angle increases [Jovic 2016]. Several studies have reported on the relationship between the angle of incidence light and resulting photocatalytic activity performance [Jovic 2016 / Curti 2017], For example, highest activity has been obtained under irradiation at 40° than at different angles during degradation of stearic acid on IO with 247-nm void [Kim 2017].

The importance of retained periodic structure throughout the photocatalytic activity is vital. The comparison between the original and slightly destroyed titania IOs, e.g., by ultrasonication [Srinivasan 2007], milling [Cai 2017] and grinding [Sordello 2011] confirms that undestroyed IO structure is necessary for high activity, e.g., 71% decrease in activity has been observed for disordered surface by milling [Cai 2017].

It should be pointed out that although titania IO might exhibit PBG in vis range of solar spectrum (depending on the void diameter), and thus is able to absorb photons with lower energy than its bandgap, this absorption should not be the reason for the photocatalytic activity

to proceed as titania is not excited (electrons from VB to CB). Accordingly, even if some reports show vis activity of titania IOs, these reports have been mainly performed for activity testing during dyes' degradation, and thus titania sensitization by dye must be considered as the main mechanism under vis irradiation, but not due to PC feature. Indeed, Curti et al. have confirmed that vis activity of titania IO is only observed for dyes (methylene blue; MB), whereas negligible effect is obtained for non-color molecules (acetaldehyde) [Curti 2017]. Tomazatou et al. have indicated that high activity of dye-sensitized titania IO (MB/TiO_2) under vis (in comparison with negligible activity by commercial titania P25) is probably caused by the slow-photon effect [Toumazatou 2017]. Chen et al. have proved that overlapping of PBG with bandgap of titania (TiO_2-coated SnO_2 IO) is the most recommended for activity enhancement, i.e., an increase in the activity in the following order of PBG: 2.55 < 2.98 <3.35 eV [Chen 2014]. Moreover, it has been shown that the highest efficiency for dye decomposition has been obtained when PBG overlaps with absorption band of MB (but away from its maximum to avoid the undesired light screening), confirming both dye-sensitization mechanism and slow photon effect [Lim 2019].

TiO_2 IO structures have been modified with various compounds, including metals, e.g., gold [Kim 2013], silver [Zhao 2012] and nickel [Li 2018] semiconductors, e.g., cadmium selenide and cadmium sulfide quantum dots (QDs) [Cheng 2012] and zinc oxide NPs [Zheng 2015], and by "self-doping" (surface-disordered-engineered TiO_2 PCs [Cai 2017]) to further enhance the photocatalytic performance by amplified light harvesting.

1-4 Plasmonic nanoparticles in photocatalysis

Noble metals such as Au, Ag, Pt and Cu are usually known as good modifiers and co-catalyst for wide-bandgap semiconductors (only active under UV) such as CeO_2 [Kominami 2010] Fe_2O_3 [Thimsen 2011], ZnO [Yu 2012], to hinder charge carriers' recombination. The unique property of noble metals that enables the activity under visible irradiation originates from localised surface plasmon resonance (LSPR) at vis-NIR range of solar spectrum. An oscillating electric field causes the conduction electrons to oscillate coherently when the wavelength of light used to excite the nanoparticles is similar or smaller in the size.

Apart from the usage of noble metals in fields such as medicine, SERS, and optical data storage, the potential application in photocatalysis especially under visible irradiation has bloomed recently. Many studies in terms of betterment in photocatalytic activity performance and stability besides clarification on the mechanism have been carried out till date. The visible light induced oxidation of organic compounds such as methyl *tert*-butyl ether [Rodriguez-Gonzalez 2008] 2-propanol and acetic acid [Kowalska 2009] by Au/TiO_2 have been studied. In addition, direct evidence on the involvement of LSPR effect as the main aspect driving the photodecomposition process has been proofed by action spectrum analyses showing highest activity observed at maximum LSPR wavelength with precise correlation to the respective photoabsorption spectra [Tian 2005 / Kowalska 2009].

Till date, the exact mechanism of the plasmonic based photocatalysis has not been clarified clearly, however few possibilities have been considered such as charge transfer, i.e., the transfer of "hot" electrons, energy transfer, and plasmonic heating (thermal activation). Mechanism on the charge transfer has been commonly considered as plasmonic photosensitizers as the noble metals have the similar role as photosensitizer. Upon LSPR excitation, incidents photons are absorbed by the plasmonic nanoparticles and the resulting photoexcited electrons might be transferred to CB of the semiconductor and proceed the reduction process of the adsorbed oxygen on the surface. Later, the electron-deficient metal could oxidize some organic compounds to recover to the original zero-valent state. This mechanism has been proven by using femtosecond transient absorption spectroscopy by observing the electron transfer of Au to TiO_2 [Furube 2007] apart from time-resolved microwave conductivity (TRMC) study, which showed conductivity signal only for the plasmonic nanoparticles and not for bare TiO_2 [Wei 2018].

The plasmonic heating was first suggested by Chen et al. in 2008, reporting that plasmonic heated Au NPs could induce the oxidation of organic compounds [Chen 2008]. Although plasmonic heating has been proposed as the main mechanism in some research, most reports have rejected this mechanism, mainly due to usually negligible activity of unsupported Au NPs and Au-modified insulators. For example, plasmonic heating has been rejected in research on water splitting [Liu 2011], photocurrent generation [Son 2010], and hydrogen dissociation [Mukherjee 2013]. The study on the activation energy has also excluded plasmonic heating for degradation of organic compounds [Kominami 2011] and generation of photocurrent [Nishijima 2010].

A lot of improvement has been done in improving the overall quantum efficiency by focusing on chemical reactions, i.e., dark part occurring after the photoexcitation process till date. Both properties of noble metals and semiconductor have been improved to enhance better interactions between them such as controllable plasmonic nanoparticles distribution on photocatalyst surface. However, the photocatalytic activity performance differs depending on the selective depositions on photocatalyst with certain faceted morphology as reported in studies related with decahedral anatase particles (DAP) [Murakami 2009] and octahedral anatase particles (OAP) [Wei 2018].

Apart from the dark-part design improvements, not many studies have been done to improve the photoabsoprtion properties of noble metals, i.e., bright-part. This is because it is almost impossible to alter the photoabsorption coefficient of the noble metals apart from controlling the fixed properties such as size, shape and the environment (refractive index of medium) of the nanoparticles. For instance, it is well known that LSPR would be observed at 520-580 nm for spherical Au nanoparticles [Link 1999] and 410-430 nm for Ag nanoparticles [Nilius 2001]. Accordingly, higher activity under visible light irradiation has been achieved by the polydisperse noble metal nanoparticles due to broader LSPR peak resulting in enhanced light harvesting [Kowalska 2009]. In this regard, the better and efficient strategy to improve on the photoabsorption efficiency of the plasmonic nanoparticles has not been reported till date.

1-5 Plasmonic based PCs photocatalysts

1-5-1 Introduction

Coupling of PCs especially IO structures with other semiconductors/materials and surface modification with plasmonic nanoparticles such as Au NPs, Ag NPs and Pt NPs have been garnering interest of many researchers in photocatalysis field recently due to the enhanced photocatalytic activity performance. In the case of plasmonic nanoparticles modification/doping on IO structures, the combination of LSPR and photonic effects arising from noble metals and slow photons (due to PBG), respectively, has been considered as one of the main factors for the amplified photoreaction rates.

1-5-2 Fabrication methods of plasmonic based PCs photocatalysts

Preparation of plasmonic based PCs could be quite challenging as the loading of the noble metal NPs should be done in a gentle way without destroying the IO structures, which directly depicting on the Bragg's diffraction and most importantly the effectiveness of LSPR effect needs to be retained. Till date, there have been several reports on the usage of photodeposition and thermal methods for plasmonic NPs deposition by using the respective metal precursors such as chloroplatinic acid (H_2PtCl_6) for Pt [Chen 2008], silver nitrate ($AgNO_3$) for Ag [Sanchez-Garcia 2016] and tetrachloroauric acid ($HAuCl_4$) for Au [Rahul 2018]. Heat treatment such as hydrothermal method has been implied to introduce Au NPs on TiO_2 PCs, strengthening the stability as interphase sintering between TiO_2 and Au NPs take places [Lu 2012]. Apart from that, co-assembly and infiltration methods have been reported to fabricate Ag- and Au-loaded PCs respectively [Erola 2015]. Interestingly, the co-assembly method is not suitable for Ag deposition on the SiO_2-IO as LSPR effect diminished after the calcination process due to lower thermal stability of Ag compared to Au. In this regard, suitable method should be considered to retain a good quality of plasmonic based PCs photocatalysts.

1-5-3 Plasmonic based PCs photocatalytic applications

Till date, only several reports have been found on plasmonic based PCs photocatalysis. Plasmonic NPs have been utilized in PCs for few factors, including (i) light harvesting at visible-NIR for semiconductors-based PCs that has lack photoabsorption ability at those regions, (ii) slow photons arising from PBG/photonic effect owning to the PCs, which might enhance and strengthen the LSPR effect and (iii) the role of plasmonic NPs as co-catalyst or electron sink to minimized the recombination rates of photoexcited charge carriers which could improve the overall quantum efficiency.

Interesting studies on the aspect mentioned at (ii) have been reported, where enhanced activity is evident only when LSPR wavelength matches with the slow photons effect, which could be realized by the nanovoid tuning to control the PBG position wavelengths. Accordingly, about 2.3-fold higher photocatalytic efficiency for photodegradation of 2,4-dichlorophenol in comparison to the reference Au NP/nanocrystalline TiO_2 under vis

irradiation has been achieved by precise tuning in formation of Au NP/TiO_2 PC to match with LSPR effect [Lu 2012]. Similar agreement has been achieved by photoelectrochemical (PEC) water splitting performance amplification by matching of LSPR and PBG red-edge (slow photons) wavelengths by using Au NP-modified TiO_2 nanorod array structure [Zhang 2014] as shown in **Fig. 1-11**. Additionally, both studies [Zhang 2014 / Lu 2012] have indicated that red-edge PBG is more effective than blue-edge one. At the red-edge PBG, the light propagates with decrease group velocity, being described as a sinusoidal standing wave that has its highest amplitude in the high refractive index part of the PC, whereas the standing wave at blue edge is localized in the low-refractive index part. Accordingly, an absorber at high dielectric part has stronger interactions with light at red-edge regions of PBG. In contrast, TiO_2-Au-CdS powdered PCs has shown the enhanced H_2 production due to utilization of slow photons at PBG blue-edge along with improvement of charge-carriers separation attributed to the role of Au NPs as electron scavenger [Zhao 2018]. In contrast to the enhanced performance in photocatalysis, even a decrease in the photocatalytic activity of TiO_2-coated nanoporous alumina IO has been observed after deposition of Au NPs or Ag NPs on its surface, where both effects do not match, i.e., LSPR at ca. 400-550 nm and PBG at ca. 800 nm [Lim 2019].

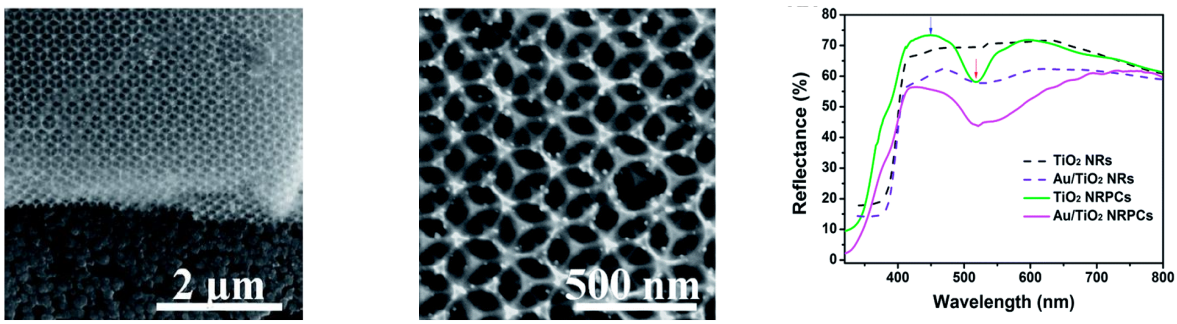

(**a**) (**b**) (c)

Fig. 1-11. (**a**) Low-magnification and (**b**) high-resolution scanning electron microscopy images of Au/TiO_2 PCs on the FTO substrate, (**c**) Diffused reflectance spectra of TiO_2 nanorods (NRs), Au/TiO_2 NRs, TiO_2 NRPCs, Au/TiO_2 NRPCs (PBG marked with dark arrow and slow-photon region marked with red arrow); Reprinted with permission (after formatting) from [Zhang, 2014]. Copyright (2014) RSC.

As mentioned in the previous section, the loading of plasmonic NPs has been critical as the amount, shape and size could alter the enhancement of photoreaction rates. For instance, different amount of Pt has been loaded on TiO_2-IO PC, which loading amount of 2wt% has exhibited the best activity in comparison to lower loading, as 1.3 wt% of Pt could not show any significant enhancement in the dye photodegradation experiment [Chen 2008]. Similarly, it has been shown that the lowest (2 mM) and the highest (20 mM) amount of deposited Ag (in terms of precursor concentration) on TiO_2 PC is not able to amplify the light absorption as the former is inadequate to exhibit LSPR and the latter results in Ag NPs' aggregation, diminishing the activity [Zhao 2012]. Loss of LSPR effect due to aggregation and disruption in charge carriers' migration has been considered as factors for lower methylene blue photodegradation efficiency [Chen 2014] resulting from longer deposition duration of Ag-NPs on TiO_2-IO PC.

Moreover, it has also been postulated that the localization of plasmonic nanomaterials in/on PC might be crucial for the overall activity. For instance, it has been proposed that deposition of NM layer on PC is not recommended, as the majority of light is absorbed in the metallic coating before it reaches the bulk PC structure, resulting in a decrease in the overall photocatalytic activity, similar to well-known "screen-effect" in other noble metal-TiO_2 structures [Wang 2018 / Wang 2019]. Accordingly, it has been proposed that the preparation of titania IO structures with plasmonic NPs inside each void would be the most profitable. In this regard, the size of NMNPs as well as void diameter should be tuned well to allow the matching between LSPR of plasmonic NPs and PBG of TiO_2.

1-6 Purpose of present study

Looking back to the basic principle of photocatalysis, photochemical reaction is initiated by photoabsorption, which is known as the bright part and followed by chemical reaction using the photoexcited charge carriers, where the reduction and oxidation process takes place, and is known as the dark part. The overall photoreaction efficiency would be denoted as the product of the photoabsorption efficiency and the quantum efficiency resulting from the chemical reaction. Generally, much attention and studies are focused on the dark part of the photocatalysis and the improvements after photoexcitation process, such as enhancement of charge separation to reduce recombination rate and many designs on improving the quantum

efficiency as discussed briefly in section 1-3 and 1-4. This is because photoabsorption efficiency denotes to property of photoabsorbing material that is fixed and almost impossible to be varied.

The use of PC could improve the bright part process, due to the appearance of slow photons from the edge of PBG, which could be utilized by the photoabsorbing material (Au NPs) incorporated in the void spaces of the TiO_2 IO PCs (labelled as Au NP@IOT). An important aspect of the study is incorporation of Au NPs inside the voids of IO, as the slow photons are multiscattered inside the void. This kind of plasmonic-based-PCs design is the first one to be reported and would be highlighted in this study. In this bright-part design, the only one Au NP incorporated in each void would have the similar photoabsorption property at ca.530 nm due to LSPR effect, however the presence of slow photons at the PBG edges wavelengths (from TiO_2 IO PCs) could enhance the photoabsorption efficiency by allowing the precise matching between both LSPR and photonic effect. Hence, the development of this bright-part design could be evident by the idea of checking and matching the wavelength ranges by using monochromatic LED irradiation thus the photoabsoprtion enhancement could be proven by observing the amplified photocatalytic activity.

Till date, all the studies reported on the coupling of slow photons and LSPR effects used polychromatic light source with wide range of visible light wavelengths. The precise matching between slow photons and plasmon effect could not be proven by polychromatic source as there is no strong evidence, indicating the enhancement arising from plasmon effect as the slow photons could match with electronic band gap of TiO_2 also under vis range till 450 nm. Hence, the importance of proving the photoabsorption enhancement due to the overlapping of LSPR effect and slow photons by using monochromatic irradiation is highlighted in this study. Apart from that, the importance of having Au NP in each void would be addressed as compared to the conventional methods for deposition of Au NPs on TiO_2 IO PC surface.

1-7 References

Amano, F.; Prieto-Mahaney, O. O.; Terada, Y.; Yasumoto, T.; Shibayama, T.; Ohtani, B., Decahedral single-crystalline particles of anatase titanium (IV) oxide with high photocatalytic activity. *Chem. Mater.* **21**, (13), 2601-2603 (2009).

Asahi, R.; Morikawa, T.; Ohwaki, T.; Aoki, K.; Taga, Y., Visible-light Photocatalysis in Nitrogen-doped Titanium Oxide, *Science*, **293**, 269–271 (2001).

Balaur, E.; Macak, J. M.; Taveira, L.; Schmuki, P., Tailoring the wettability of TiO_2 nanotube layers. *Electrochem Commun* **7**, (10), 1066-1070 (2005).

Baur, E.; Neuweiler, C., Über Photolytische Bildung von Hydroperoxyd, *Helv. Chim. Acta*, **10**, 901–907 (1927).

Baur, E.; Perret, A.; *Helv. Chim. Acta* **7**, 910-915 (1924).

Beranek, R.; Tsuchiya, H.; Sugishima, T.; Macak, J. M.; Taveira, L.; Fujimoto, S.; Kisch, H.; Schmuki, P., Enhancement and limits of the photoelectrochemical response from anodic TiO_2 nanotubes. *Appl Phys Lett***, 87**, (24), 243114/1-243114/3 (2005).

Brigden, C. T.; Poulston, S.; Twigg, M. V.; Walker, A. P.; Wilkins, A. J. J., Photooxidation of short-chain hydrocarbons over titania. *Appl. Catal. B-Environ.* **32**, (1-2), 63-71 (2001).

Cai, J. M.; Wu, M. Q.; Wang, Y. T.; Zhang, H.; Meng, M.; Tian, Y.; Li, X. G.; Zhang, J.; Zheng, L. R.; Gong, J. L., Synergetic enhancement of light harvesting and charge separation over surface-disorder-engineered TiO_2 photonic crystals. *Chem.* **2**, 877-892 (2017).

Campbell, L. K.; Na, B. K.; Ko, E. I., Synthesis and Characterization of Titania Aerogels. *Chem. Mater.* **4**, (6), 1329-1333 (1992).

Chen, J. I. L.; Loso, E.; Ebrahim, N.; Ozin, G. A., Synergy of slow photon and chemically amplified photochemistry in platinum nanocluster-loaded inverse titania opals. *J. Am. Chem. Soc.* **130**, 5420-5421 (2008).

Chen, X.; Li, Z; Ye, J.; Zou, Z. Forced impregnation approach to fabrication of large-area, three-dimensionally ordered macroporous metal oxides. *Chem. Mater.* **22**, 3583–3585 (2010).

Chen, X.; Zhu, H.-Y.; Zhao, J.-C.; Zheng, Z.-F.; Gao, X.-P., Visible-light-driven oxidation of organic contaminants in air with gold nanoparticle catalysts on oxide supports. *Angew. Chem. Int. Ed.* **47**, 5353-5356 (2008).

Chen, Z.; Fang, L.; Dong, W.; Zheng, F.; Shen, M.; Wang, J., Inverse opal structured Ag/TiO_2 plasmonic photocatalyst prepared by pulsed current deposition and its enhanced visible light photocatalytic activity. *J. Mat. Che. A* **2**, 824-832 (2014).

Cheng, C. W.; Karuturi, S. K.; Liu, L. J.; Liu, J. P.; Li, H. X.; Su, L. T.; Tok, A. I. Y.; Fan, H. J., Quantum-dot-sensitized TiO_2 inverse opals for photoelectrochemical hydrogen generation. *Small* **8**, 37-42 (2012).

Chiang, C. C.; Tuyen, L. D.; Ren, C. R.; Chau, L. K.; Wu, C. Y.; Huang, P. J.; Hsu, C. C., Fabrication of titania inverse opals by multi-cycle dip-infiltration for optical sensing. *Photonic Nanostruct* **19**, 48-54 (2016).

Chiarello, G. L.; Zuliani, A.; Ceresoli, D.; Martinazzo, R.; Selli, E., Exploiting the photonic crystal properties of TiO_2 nanotube arrays to enhance photocatalytic hydrogen production. *ACS Catal.* **6**, 1345-1353 (2016).

Curti, M.; Mendive, C. B.; Grela, M. A.; Bahnemann, D. W., Stopband tuning of TiO_2 inverse opals for slow photon absorption. *Mater. Res. Bull.* **91**, 155-165 (2017).

Curti, M.; Robledo, G. L.; Claro, P. C. D.; Ubogui, J. H.; Mendive, C. B., Characterization of titania inverse opals prepared by two distinct infiltration approaches. *Mater. Res. Bull.* **101**, 12-19 (2018).

Curti, M.; Schneider, S.; Bahnemann, D. W; Mendive, C. B. Inverse Opal Photonic Crystals as a Strategy to Improve Photocatalysis: Underexplored Questions *J. Phys. Chem. Lett.*, **6, 19**, 3903–3910 (2015).

DeSario, P. A.; Pietron, J. J.; DeVantier, D. E.; Brintlinger, T. H.; Stroud, R. M.; Rolison, D. R., Plasmonic enhancement of visible-light water splitting with Au-TiO_2 composite aerogels. *Nanoscale* **5**, (17), 8073-8083 (2013).

Di Paola, A.; Bellardita, M.; Palmisano, L., Brookite, the least known TiO_2 photocatalyst. *Catalysts* **3**, (1), 36-73 (**2013)**.

Dinh, C. T.; Nguyen, T. D.; Kleitz, F.; Do, T. O., Shape-controlled synthesis of highly crystalline titania nanocrystals. *ACS Nano* **3,** (11), 3737-3743 (2009).

Erola, M. O. A.; Philip, A.; Ahmed, T.; Suvanto, S.; Pakkanen, T. T., Fabrication of Au- and Ag-SiO_2 inverse opals having both localized surface plasmon resonance and Bragg diffraction. *J. Solid State Chem.* **230**, 209-217 (2015).

Fox, M. A.; Dulay, M. T.; Heterogeneous photocatalysis. *Chem. Rev.* **93**, 341-357 (1993).

Frank, S. N.; Bard, A. J.; Heterogeneous photocatalytic oxidation of cyanide ion in aqueous solutions at titanium dioxide powder. *J. Am. Chem. Soc.* **99**, 303-304 (1977).

Fujishima, A.; Hashimoto, K.; Watanabe, T. TiO_2 Photocatalysis: Fundamentals and applications. (BKC, Tokyo, 1999)

Fujishima, A.; Honda, K., Electrochemical photolysis of water at a semiconductor electrode. *Nature*, **238**, 37–38 (1972).

Furube, A.; Du, L.; Hara, K.; Katoh, R.; Tachiya, M. Ulltrafast plasmon-induced electron transfer from gold nanodots into TiO_2 nanoparticles. *J. Am. Chem. Soc.* **129**, 14852-14853 (2007).

Gong, D.; Grimes, C. A.; Varghese, O. K.; Hu, W.; Singh, R. S.; Chen, Z.; Dickey, E. C. Titanium oxide nanotube arrays prepared by anodic oxidation. *Journal of Materials Research* **16**, (12), 3331-3334 (2001).

Gong, X. Q.; Selloni, A. First-principles study of the structures and energetics of stoichiometric brookite TiO_2 surfaces. *Phys Rev B* **76**, (23) (2007).

Gratzel, M.; Rotzinger, F. P. The Influence of the Crystal-lattice structure on the conduction-band energy of oxides of titanium (IV). *Chem. Phys. Lett.* **118**, (5), 474-477 (1985).

Han, X. G.; Wang, X.; Xie, S. F.; Kuang, Q.; Ouyang, J. J.; Xie, Z. X.; Zheng, L. S. Carbonate ions-assisted syntheses of anatase TiO_2 nanoparticles exposed with high energy (001) facets. *Rsc Adv* **2**, (8), 3251-3253 (2012).

Honda, H.; Ishizaki, A., Soma, R.; Hashimoto, K.; Fujishima, A. Application of Photocatalytic Reactions Caused by TiO_2 Film to Improve the Maintenance Factor of Lighting Systems. *Journal of the Illuminating Engineering Society* **27,** 42-49 (1998).

Hua, C. X.; Xu, H. B.; Zhang, P. P.; Chen, X. Y.; Lu, Y. Y.; Gan, Y.; Zhao, J. P.; Li, Y. Process optimization and optical properties of colloidal self-assembly via refrigerated centrifugation. *Colloid Polym. Sci.* **295**, 1655-1662 (2017).

Hupka, J.; Zaleska, A.; Janczarek, M.; Kowalska, E.; Gorska, P.; Aranowski, R., UV/Vis light-enhanced photocatalysis for water treatment and protection. In *Soil and Water Pollution Monitoring, Protection and Remediation*, Twardowska, I.; Allen, H. E.; Häggblom, M. M.; Stefaniak, S., Eds. Springer Netherlands: Berlin, 2006; Vol. Nato Science Series: IV. Earth and Environmental Sciences, pp 151-166.

Imai, H.; Takei, Y.; Shimizu, K.; Matsuda, M.; Hirashima, H. Direct preparation of anatase TiO_2 nanotubes in porous alumina membranes. *J Mater Chem* **9**, (12), 2971-2972 (1999).

Islam, M. T. et al. Fullerene stabilized gold nanoparticles supported on titanium dioxide for enhanced photocatalytic degradation of methyl orange and catalytic reduction of 4-nitrophenol. *J. Environ. Chem. Eng.* **6,** 3827–3836 (2018).

Janczarek, M.; Kowalska, E.; Ohtani, B. Decahedral-shaped anatase titania photocatalyst particles: synthesis in a newly developed coaxial-flow gas-phase reactor. *Chem Eng J* **289**, 502-512 (2016).

Jiang, P.; Bertone, J. F.; Hwang, K. S.; Colvin, V. L. Single-crystal colloidal multilayers of controlled thickness. *Chem. Mater.* **11**, 2132-2140 (1999).

Jovic, V.; Idriss, H.; Waterhouse, G. I. N. Slow photon amplification of gas-phase ethanol photo-oxidation in titania inverse opal photonic crystals. *Chem. Phys.* **479**, 109-121 (2016).

Kandiel, T. A.; Feldhoff, A.; Robben, L.; Dillert, R.; Bahnemann, D. W. Tailored titanium dioxide nanomaterials: anatase nanoparticles and brookite nanorods as highly active photocatalysts. *Chem. Mater.* **22**, (6), 2050-2060 (2010).

Kasuga, T.; Hiramatsu, M.; Hoson, A.; Sekino, T.; Niihara, K. Titania nanotubes prepared by chemical processing. *Adv Mater* 11, (15), 1307 (1999).

Kim, K.; Thiyagarajan, P.; Ahn, H. J.; Kim, S. I.; Jang, J. H. Optimization for visible light photocatalytic water splitting: gold-coated and surface-textured TiO_2 inverse opal nano-networks. *Nanoscale* **5**, 6254-6260 (2013).

Kim, W. T.; Choi, W. Y. Fabrication of TiO_2 photonic crystal by anodic oxidation and their optical sensing properties. *Sensor Actuat a-Phys* **260**, 178-184 (2017).

Kominami, H.; Tanaka, A.; Hashimoto, K. Gold nanoparticles supported on cerium (IV) oxide powder for mineralization of organic acids in aqueous suspensions under irradiation of visible light of λ = 530 nm. *Appl. Catal. Gen.* **397**, 121–126 (2011).

Kominami, H.; Tanaka, A.; Hashimoto, K. Mineralization of organic acids in aqueous suspension of gold nanoparticles supported on cerium (IV) oxide powder under visible light irradiation. *Chem. Commun.* **46**, 1287-1289 (2010).

Kou, J. H.; Lu, C. H.; Wang, J.; Chen, Y. K.; Xu, Z. Z.; Varma, R. S. Selectivity enhancement in heterogeneous photocatalytic transformations. *Chem Rev* **117**, (3), 1445-1514 (2017).

Kowalska, E. Investigation of photochemical degradation of organic compounds. PhD Thesis, Gdansk University of Technology, Gdansk, Poland, 2004.

Kowalska, E.; Rau, S.; Ohtani, B. Plasmonic titania photocatalysts active under UV and visible-light irradiation: Influence of gold amount, size, and shape. *J. Nanotechnol.* **2012,** 1-11 (2012).

Kowalska, E.; Abe, R.; Ohtani, B. Visible light-induced photocatalytic reaction of gold-modified titanium (IV) oxide particles: action spectrum analysis. *Chem. Commun.* **2**, 241-243 (2009).

Kowalska, E.; Rau, S. Photoreactors for wastewater treatment: A review. *Recent Pat. Engin.* **4**, (3), 242-266 (2010).

Kowalski, D.; Kim, D.; Schmuki, P. TiO_2 nanotubes, nanochannels and mesosponge: Self-organized formation and applications. *Nano Today* **8**, (3), 235-264 (2013).

Kowalski, D.; Schmuki, P. Polypyrrole self-organized nanopore arrays formed by controlled electropolymerization in TiO_2 nanotube template. *Chem Commun* **46**, (45), 8585-8587 (2010).

Kozak, M.; Mazierski, P.; Zebrowska, J.; Kobylanski, M.; Klimczuk, T.; Lisowski, W.; Trykowski, G.; Nowaczyk, G.; Zaleska-Medynska, A. Electrochemically obtained tio_2/cu_xo_y nanotube arrays presenting a photocatalytic response in processes of pollutants degradation and bacteria inactivation in aqueous phase. *Catalysts* **8**, (6) (2018).

Kubrin, R.; Pasquarelli, R. M.; Waleczek, M.; Lee, H. S.; Zierold, R.; do Rosario, J. J.; Dyachenko, P. N.; Moreno, J. M. M.; Petrov, A. Y.; Janssen, R.; Eich, M.; Nielsch, K.; Schneider, G. A. Bottom-up fabrication of multilayer stacks of 3D photonic crystals from titanium dioxide. *ACS Appl. Mater. Inter.* **8**, 10466-10476 (2016).

Lazzeri, M.; Vittadini, A.; Selloni, A. Structure and energetics of stoichiometric TiO_2 anatase surfaces. *Phys Rev B* **63**, 15 (2001).

Li, H.; Vienneau, G.; Jones, M.; Subramanian, B.; Robichaud, J.; Djaoued, Y. Crack-free 2D-inverse opal anatase TiO_2 films on rigid and flexible transparent conducting substrates: low temperature large area fabrication and electrochromic properties. *J Mater Chem C* **2**, (37), 7804-7810 (2014).

Li, X. H.; Wu, Y.; Shen, Y. H.; Sun, Y.; Yang, Y.; Xie, A. J. A novel bifunctional Ni-doped TiO_2 inverse opal with enhanced SERS performance and excellent photocatalytic activity. *Appl. Surf. Sci*. **427**, 739-744 (2018).

Li, X.; Yu, J. G.; Jaroniec, M. Hierarchical photocatalysts. *Chem. Soc. Rev*. **45**, 2603-2636 (2016).

Li, Z. Z.; Xin, Y. M.; Wu, W. L.; Fu, B. H.; Zhang, Z. H. Phosphorus cation doping: A new strategy for boosting photoelectrochemical performance on TiO_2 nanotube photonic crystals. *ACS Appl. Mater. Inter*. **8**, 30972-30979 (2016).

Likodimos, V. Photonic crystal-assisted visible light activated TiO_2 photocatalysis. *Appl. Catal. B-Environ.* **230**, 269-303 (2018).

Lim, S. Y.; Law, C. S.; Liu, L.; Markovis, M.; Abell, A. D.; Santos, A. Integrating surface plasmon resonance and slow photon effects in nanoporous anodis alumina photonic crystals for photocatalysis. *Catal. Sci. Technol.* **9**, 3158-3176 (2019).

Link, S.; El-Sayed, M. A. Spectral properties and relaxation dynamics of surface plasmon electronic oscillations in gold and silver nanodots and nanorods. *J. Phys. Chem. B* **103**, 8410-8426 (1999).

Liu, G.; Yang, H. G.; Pan, J.; Yang, Y. Q.; Lu, G. Q.; Cheng, H. M. Titanium dioxide crystals with tailored facets. *Chem Rev* **114**, (19), 9559-9612 (2014).

Liu, G.; Yu, J. C.; Lu, G. Q.; Cheng, H. M. Crystal facet engineering of semiconductor photocatalysts: motivations, advances and unique properties. *Chem Commun* **47**, (24), 6763-6783 (2011).

Liu, L. J.; Karuturi, S. K.; Su, L. T.; Tok, A. I. Y. TiO_2 inverse-opal electrode fabricated by atomic layer deposition for dye-sensitized solar cell applications. *Energ. Environ. Sci.* **4**, 209-215 (2011).

Liu, Z.; Hou, W.; Pavaskar, P.; Aykol, M.; Cronin, S.B. Plasmon resonance enhancement of photocatalytic water splitting under visible illumination. *Nano Lett.* **11**, 1111–1116. (2011)

Lopez, C., Materials aspects of photonic crystals. *Adv Mater* **15**, (20), 1679-1704 (2003).

Lu, X. Y.; Zhu, Y.; Cen, T. Z.; Jiang, L. Centimeter-scale colloidal crystal belts via robust self-assembly strategy. *Langmuir* **28**, 9341-9346 (2012).

Lu, Y.; Yu, H. T.; Chen, S.; Quan, X.; Zhao, H. M. Integrating plasmonic nanoparticles with TiO_2 photonic crystal for enhancement of visible-light-driven photocatalysis. *Environ. Sci. Technol.* **46**, 1724-1730 (2012).

Malinowska, B.; Walendziewski, J.; Robert, D.; Weber, J. V.; Stolarski, M. Titania aerogels: Preparation and photocatalytic tests. *Int J Photoenergy* **5**, (3), 147-152 (2003).

Matsunaga, T.; Tomoda, R.; Nakajima, T.; Wake, H. Photoelectrochemical sterilization of microbial cells by semiconductor powders. *FEMS Microbiol. Lett*, **29**, 211–214 (1985).

Mayoral, R.; Requena, J.; Moya, J. S.; Lopez, C.; Cintas, A.; Miguez, H.; Meseguer, F.; Vazquez, L.; Holgado, M.; Blanco, A. 3D long-range ordering in an SiO_2 submicrometer-sphere sintered superstructure. *Adv. Mater.* **9**, 257-260 (1997).

Mazierski, P.; Malankowska, A.; Kobylanski, M.; Diak, M.; Kozak, M.; Winiarski, M. J.; Klimczuk, T.; Lisowski, W.; Nowaczyk, G.; Zaleska-Medynska, A. Photocatalytically Active TiO_2/Ag_2O Nanotube Arrays Interlaced with Silver Nanoparticles Obtained from the One-Step Anodic Oxidation of Ti-Ag Alloys. *Acs Catal* **7**, (4), 2753-2764 (2017).

Michael R.; Hoffmann, S.; Martin, T.; Choi, W.; Bahnemann. D. W. Environmental applications of semiconductor photocatalysis. *Chem. Rev.*, **95**, 69-96 (1995).

Miguez, H.; Meseguer, F.; Lopez, C.; Blanco, A.; Moya, J. S.; Requena, J.; Mifsud, A.; Fornes, V. Control of the photonic crystal properties of fcc-packed submicrometer SiO_2 spheres by sintering. *Adv. Mater.* **10**, 480-483 (1998).

Moon, J. H.; Cho, Y. S.; Yang, S. M. Room temperature chemical vapor deposition for fabrication of titania inverse opals: Fabrication, morphology analysis and optical characterization. *B. Korean Chem. Soc.* **30**, 2245-2248 (2009).

Mukherjee, S.; Libisch, F.; Large, N.; Neumann, O.; Brown, L.V.; Cheng, J.; Lassiter, J.B.; Carter, E.A.; Nordlander, P.; Halas, N. J. Hot electrons do the impossible: Plasmon-induced dissociation of H_2 on Au. *Nano Lett.* **13**, 240–247 (2013).

Murakami, N.; Katayama, S.; Nakamura, M.; Tsubota, T.; Ohno, T. Dependence of Photocatalytic Activity on Aspect Ratio of Shape-Controlled Rutile Titanium (IV) Oxide Nanorods. *J Phys Chem C* **115**, (2), 419-424 (2012).

Murakami, N.; Kurihara, Y.; Tsubota, T.; Ohno, T. Shape-controlled anatase titanium(iv) oxide particles prepared by hydrothermal treatment of peroxo titanic acid in the presence of polyvinyl alcohol. *J. Phys. Chem. C* **113**, 3062-3069 (2009).

Nilius, N.; Ernst, N.; Freund, H. On energy transfer processes at cluster-oxide interfaces: silver on titania. *Chem. Phys. Lett.* **349**, 351-357 (2001).

Nishijima, Y.; Ueno, K.; Yokata, Y.; Murakoshi, K.; Misawa, H. Plasmon-assisted photocurrent generation from visible to near-infrared wavelength using a Au-nanorods/TiO_2 electrode. J. Phys. *Chem. Lett.* **1**, 2031–2036 (2010).

Ohno, T.; Sarukawa, K.; Matsumura, M. Crystal faces of rutile and anatase TiO_2 particles and their roles in photocatalytic reactions. *New J. Chem.* **26**, (9), 1167-1170 (2012).

Ohno, T.; Tokieda, K.; Higashida, S.; Matsumura, M. Synergism between rutile and anatase TiO_2 particles in photocatalytic oxidation of naphthalene. *Applied Catalysis, A: General* **244**, (2), 383-391 (2003).

Ohtani, B. Photocatalysis A to Z—What We Know and What We Don't Know, *J. Photochem. Photobiol. C Photochem. Rev.*, **11**, 157–178 (2010).

Ohtani, B. Revisiting the Fundamental Physical Chemistry in Heterogeneous Photocatalysis: Its Thermodynamics and Kinetics, *Phys. Chem. Chem. Phys.*, **16**, 1788–1797 (2014).

Oyama, T.; Iimura, Y.; Takeuchi, K.; Ishii, T. Synthesis of rutile and anatase TiO_2 fine particles by laser-ignited vapour-phase reaction. *J Mater Sci Lett* **15**, (7), 594-596 (1996).

Panayotov, D. A.; DeSario, P. A.; Pietron, J. J.; Brintlinger, T. H.; Szymczak, L. C.; Rolison, D. R.; Morris, J. R. Ultraviolet and Visible Photochemistry of Methanol at 3D Mesoporous Networks: TiO_2 and Au-TiO_2. *J Phys Chem C* **117**, (29), 15035-15049 (2013).

Pelizzetti, E.; Borgarello, M.; Minero, C.; Pramauro, E.; Borgarello, E.; Serpone, N. Photocatalytic degradation of polychlorinated dioxins and polychlorinated biphenyls in aqueous suspensions of semiconductors irradiated with simulated solar light. *Chemosphere* **17**, 499-510 (1988).

Peral, J.; Ollis, D. F. Heterogeneous photocatalytic oxidation of gas-phase organics for air purification: Acetone, 1-butanol, butyraldehyde, formaldehyde, and m-xylene oxidation. *J. Catal.* **136**, 554-565 (1992).

Prieto-Mahaney, O. O.; Murakami, N.; Abe, R.; Ohtani, B. Correlation between photocatalytic activities and structural and physical properties of titanium (IV) oxide powders. *Chem. Lett.* **38**, (3), 238-239 (2009).

Rahul, T. K.; Sandhyarani, N. Plasmonic and photonic effects on hydrogen evolution over chemically modified titania inverse opals. *Chemnanomat* **4**, 642-648 (2018).

Rahul, T. K.; Sandhyarani. N. Nitrogen-Fluorine co-doped titania inverse opals for enhanced solar light driven photocatalysis**.** *Nanoscale* **7**, 18259-18270 (2015).

Ramamoorthy, M.; Vanderbilt, A. First-principles calculations of the energetics of stoichiometric TiO_2 surfaces. *Phys. Rev. B* **49**, 16721-16727 (1994).

Rao, M. V.; Rajeshwar, K.; Verneker, V. R. P.; DuBow, J. Photosynthetic production of hydrogen and hydrogen peroxide on semiconducting oxide grains in aqueous solutions. *Journal of Physical Chemistry* **84**, (15), 1987-91 (1980).

Rodriguez-Gonzalez, V.; Zanella, R.; del Angel, G.; Gomez, R. MTBE visible-light photocatalytci decomposition over Au/TiO_2 and Au/TiO_2-Al_2O_3 sol-gel prepared catalysts. *J. Mol. Catal. A: Chem.* **281**, 93-98 (2008).

Sanchez-Garcia, L.; Tserkezis, C.; Ramirez, M. O.; Molina, P.; Carvajal, J. J.; Aguilo, M.; Diaz, F.; Aizpurua, J.; Bausa, L. E. Plasmonic enhancement of second harmonic generation from nonlinear $RbTiOPO_4$ crystals by aggregates of silver nanostructures. *Opt. Express* **24**, 8491-8500 (2016).

Son, M.S.; Im, J.E.; Wang, K.K.; Oh, S.L.; Kim, Y.R.; Yoo, K. H. Surface plasmon enhanced photoconductance and single electron e_ects in mesoporous titania nanofibers loaded with gold nanoparticles. *Appl. Phys. Lett*. **96**, 023115 (2010).

Sordello, F.; Duca, C.; Maurino, V.; Minero, C. Photocatalytic metamaterials: TiO_2 inverse opals. *Chem. Commun.* **47**, 6147-6149 (2011).

Srinivasan, M.; White, T. Degradation of methylene blue by three-dimensionally ordered macroporous titania. *Environ. Sci. Technol.* **41**, 4405-4409 (2007).

Subrt, J.; Plizingrova, E.; Palkovska, M.; Bohacek, J.; Klementova, M.; Kupcik, J.; Bezdicka, P.; Sovova, H. Titania aerogels with tailored nano and microstructure: comparison of lyophilization and supercritical drying. *Pure Appl Chem.* **89**, (4), 501-509 (2017).

Sunada, K.; Watanabe, T.; Hashimoto, K. Bactericidal Activity of Copper-Deposited TiO_2 Thin Film under Weak UV Light Illumination *Environ. Sci. Technol.* **37**, 20, 4785–4789 (2003).

Thimsen, E.; Le Formal, F.; Gratzel, M.; Warren, S. C. Influence of plasmonic au nanoparticles on the photoactivity of Fe_2O_3 electrodes for water splitting. *Nano Lett.*, **11**, 35-43 (2011).

Tian, Y.; Tatsuma, T. Mechanisms and applications of plasmon-induced charge separation at TiO_2 films loaded with gold nanoparticles. *J. Am. Chem. Soc.* **127**, 7632-7637 (2005).

Toumazatou, A.; Arfanis, M. K.; Pantazopoulos, P.-A.; Kontos, A. G.; Falaras, P.; Stefanou, N.; Likodimos, V. Slow-photon enhancement of dye sensitized TiO_2 photocatalysis. *Mat. Lett.* **197**, 123-126 (2017).

Umebayashi, T.; Yamaki, T.; Itoh, H.; Asai, K. Band gap narrowing of titanium dioxide by sulfur doping. *J. Appl. Phys.* **93**, 5156 (2003).

Vittadini, A.; Selloni, A.; Rotzinger, F. P.; Gratzel, M. Structure and energetics of water adsorbed at TiO_2 anatase (101) and (001) surfaces. *Phys Rev Lett* **81**, (14), 2954-2957 (1998).

Wan, Y.; Wang, J.; Wang, X.; Xu, H.; Yuan, S.; Zhang, Q.; Zhang, M. Preparation of inverse opal titanium dioxide for photocatalytic performance research. *Optic. Mater.* **96**, 109287-109287-7 (2019).

Wang, K. L.; Janczarek, M.; Wei, Z. S.; Raja-Mogan, T.; Endo-Kimura, M.; Khedr, T. M.; Ohtani, B.; Kowalska, E. Morphology- and crystalline composition-governed activity of titania-based photocatalysts: Overview and perspective. *Catalysts* **9**, (2019)

Wang, K. L.; Wei, Z. S.; Ohtani, B.; Kowalska, E. Interparticle electron transfer in methanol dehydrogenation on platinum-loaded titania particles prepared from P25. *Catal. Today* **303**, 327-333 (2018).

Wei, Z. S.; Kowalska, E.; Ohtani, B. Enhanced Photocatalytic Activity by Particle Morphology: Preparation, Characterization, and Photocatalytic Activities of Octahedral Anatase Titania Particles. *Chem. Lett.* **43**, (3), 346-348 (2014).

Wei, Z.; Janczarek, M.; Endo, M.; Colbeau-Justin, C.; Ohtani, B.; Kowalska, E. Silver-modified octahedral anatase particles as plasmonic photocatalyst. *Catal. Today* **310**, 19-25 (2018).

Wei, Z.; Janczarek, M.; Endo, M.; Wang, K. L.; Balcytis, A.; Nitta, A.; Mendez-Medrano, M. G.; Colbeau-Justin, C.; Juodkazis, S.; Ohtani, B.; Kowalska, E. Noble metal-modified faceted anatase titania photocatalysts: Octahedron versus decahedron. *Appl Catal B-Environ* **237**, 574-587 (2018).

Wei, Z.; Kowalska, E.; Verrett, J.; Colbeau-Justin, C.; Remita, H.; Ohtani, B. Morphology-dependent photocatalytic activity of octahedral anatase particles prepared by ultrasonication-hydrothermal reaction of titanates. *Nanoscale* **7**, (29), 12392-12404 (2015).

Wu, M.; Liu, J.; Jin, J.; Wang, C.; Huang, S. Z.; Deng, Z.; Li, Y.; Su, B. L. Probing significant light absorption enhancement of titania inverse opal films for highly exalted photocatalytic degradation of dye pollutants. *Appl. Catal. B-Environ.* **150**, 411-420 (2014).

Wysocka, I.; Kowalska, E.; Trzcinski, K.; Lapinski, M.; Nowaczyk, G.; Zielinska-Jurek, A. UV-Vis-Induced Degradation of Phenol over Magnetic Photocatalysts Modified with Pt, Pd, Cu and Au Nanoparticles. *Nanomaterials-Basel* **8**, (1) (2018).

Yablonovitch, E. Photonic Band-Gap Structures. *J Opt Soc Am B* **10**, (2), 283-295 (1993).

Yang, H. G.; Liu, G.; Qiao, S. Z.; Sun, C. H.; Jin, Y. G.; Smith, S. C.; Zou, J.; Cheng, H. M.; Lu, G. Q. Solvothermal synthesis and photoreactivity of anatase tio$_2$ nanosheets with dominant {001} Facets. *J Am Chem Soc* **131**, (11), 4078-4083 (2009).

Yang, H. G.; Sun, C. H.; Qiao, S. Z.; Zou, J.; Liu, G.; Smith, S. C.; Cheng, H. M.; Lu, G. Q. Anatase TiO_2 single crystals with a large percentage of reactive facets. *Nature* **453**, (7195), 638-U4 (2008).

Yang, H. Y.; Zhu, S. K.; Pan, N. Studying the mechanisms of titanium dioxide as ultraviolet-blocking additive for films and fabrics by an improved scheme. *J Appl Polym Sci* **92**, (5), 3201-3210 (2004).

Yu, H.; Ming, H.; Zhang, H.; Li, H.; Pan, K.; Liu, Y.; Wang, F.; Gong, J.; Kang, Z. Au/ZnO nanocomposite: Facile fabrication and enhanced photocatalytic activity for degradation of benzene. *Mat. Chem. Phys.* **137**, 113-117 (2012).

Zhang, J. H.; Liu, H. Y.; Wang, Z. L.; Ming, N. B. Assembly of high-quality colloidal crystals under negative pressure. *J Appl Phys* **103**, (1) (2008).

Zhang, X.; Liu, Y.; Lee, S. T.; Yang, S. H.; Kang, Z. H. Coupling surface plasmon resonance of gold nanoparticles with slow-photon-effect of TiO_2 photonic crystals for synergistically enhanced photoelectrochemical water splitting. *Energ. Environ. Sci.* **7**, 1409-1419 (2014).

Zhang, Y. X.; Quan, M. H.; Zhao, W. D.; Yang, Z.; Wang, D.; Cao, H.; He, W. L. Preferential self-assembly behavior of polydisperse silica particles under negative pressure. *Colloid Surface A* **529**, 832-839 (2017).

Zhang, Y.; Li, K.; Su, F. Y.; Cai, Z. Y.; Liu, J. X.; Wu, X. W.; He, H. L.; Yin, Z.; Wang, L. H.; Wang, B.; Tian, Y. Q.; Luo, D.; Sun, X. W.; Liu, Y. J. Electrically switchable photonic crystals based on liquid-crystal-infiltrated TiO_2-inverse opals. *Opt Express* **27**, (11), 15391-15398 (2019).

Zhang, Z. H.; Wu, H. J. Multiple band light trapping in ultraviolet, visible and near infrared regions with TiO_2 based photonic materials. *Chem. Commun.* **50**, 14179-14182 (2014).

Zhang, Z. H.; Yang, X. L.; Hedhili, M. N.; Ahmed, E.; Shi, L.; Wang, P. Microwave-Assisted Self-Doping of TiO_2 Photonic Crystals for Efficient Photoelectrochemical Water Splitting. *Acs Appl Mater Inter* **6**, (1), 691-696 (2014).

Zhao, Y. X.; Yang, B. F.; Xu, J.; Fu, Z. P.; Wu, M.; Li, F. Facile synthesis of Ag nanoparticles supported on TiO_2 inverse opal with enhanced visible-light photocatalytic activity. *Thin Solid Films* **520**, 3515-3522 (2012).

Zhao, H.; Hu, Z.Y.; Liu, J.; Li, Y.; Wu, M.; Van Tendeloo, G.; Su, B. L. Blue-edge slow photons promoting visible-light hydrogen production on gradient ternary 3DOM TiO_2-Au-CdS photonic crystals. *Nano Energy* **47**, 266–274 (2018).

Zheng, S.; Wei, Z.; Yoshiiri, K.; Braumuller, M.; Ohtani, B.; Rau, S.; Kowalska, E. Titania modification with a ruthenium (II) complex and gold nanoparticles for photocatalytic degradation of organic compounds. *Photochem. Photobiol. Sci.* **15,** 69–79 (2016).

Zheng, X. Z.; Li, D. Z.; Li, X. F.; Chen, J.; Cao, C. S.; Fang, J. L.; Wang, J. B.; He, Y. H.; Zheng, Y. Construction of ZnO/TiO_2 photonic crystal heterostructures for enhanced photocatalytic properties. *Appl. Catal. B-Environ.* **168**, 408-415 (2015).

Zhou, Q.; Dong, P.; Liu, L. X.; Cheng, B. Y. Study on the sedimentation self-assembly of colloidal SiO_2 particles under gravitational field. *Colloid. Surface. A* **253**, 169-174 (2005).

Zielinska-Jurek, A.; Bielan, Z.; Wysocka, I.; Strychalska, J.; Janczarek, M.; Klimczuk, T. Magnetic semiconductor photocatalysts for the degradation of recalcitrant chemicals from flow back water. *J Environ Manage* 195, 157-165 (2017).

Zielinska-Jurek, A.; Klein, M.; Hupka, J. Enhanced visible light photocatalytic activity of Pt/I-TiO_2 in a slurry system and supported on glass packing. *Sep Purif Technol* **189**, 246-252 (2017).

Chapter 2

Materials and experimental details

2-1 Materials

Hydrogen tetrachlorogold(III) tetrahydrate (99.9%), trisodium citrate (> 99%), 3-aminopropyltriethoxysilane (3-APS), sodium silicate (> 98%), ammonia (25%), tetraethylorthosilicate (TEOS) (> 95 %), titanium isopropoxide (> 95%), sodium hydroxide (> 98%) and ethanol (99.5 %) were purchased from Wako Pure Chemical and used without further purification. Milli-Q water with a resistivity of 18.2 MΩ was used throughout the experiments.

2-2 Preparation of three-dimensional Au-NP@IOT samples

The procedure used for Au-NPs@IOT preparation consists of five steps, as illustrated in **Fig. 2-1**: (1) preparation of homogeneous-sized Au NPs, (2) covering of Au-NPs by silica layers to obtain the core-shell structured Au-NP@SiO_2 (3) preparation of Au-NP@SiO_2 opal-structured colloidal crystal (4) infiltration of a titania precursor to the interspaces of the Au-NP@SiO_2 opal via a forced impregnation method (5) selective etching of silica.

2-2-1 Synthesis of Au NPs

Au NPs with controlled shape and diameters were very vital in the preparation of core-shells with high monodispersity, hence two Turkevich-based synthesis methods (seeding and direct citrate reduction) were attempted to prepare homogeneous-sized Au NPs. All the apparatuses were rinsed with aqua regia and Milli-Q water to remove traces of metal ions before the experiments were conducted.

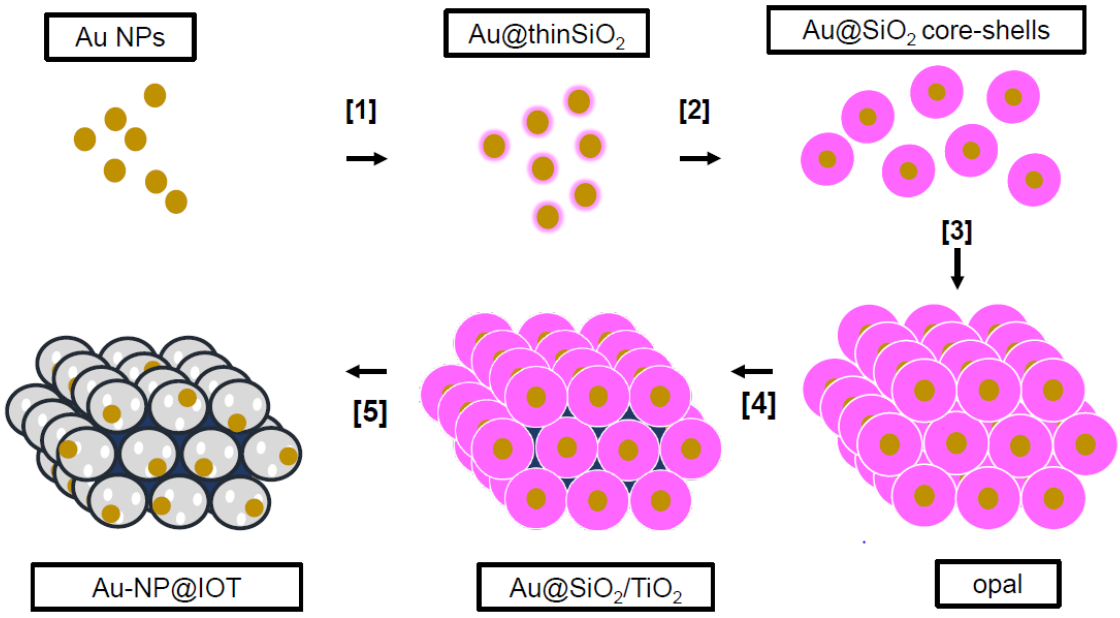

Fig. 2-1. Schematic illustration on the formation of 3D powdered Au-NPs@IOT.

2-2-1-1 Seeding method

Firstly, seeding method (Bastus 2011) was attempted to prepare the Au NPs colloidal. In the initial step, Au seeds were synthesized. A heating mantle was used to heat trisodium citrate solution (2.2 mM) in a 300 mL three neck round bottomed flask. A condenser was fitted to prevent the evaporation of the solvent. 1 mL of $HAuCl_4$ (25 mM) solution was inserted once the trisodium citrate solution began to boil.

After the synthesis of Au seeds, the reaction condition temperature was reduced to 90°C. For the first cycle, 1 mL of $HAuCl_4$ (25 mM) solution was added to the seed solution that has been previously prepared. After 30 minutes of stirring, a darker red solution could be

observed. The process was repeated for another 2 more times to slowly increase the diameter of the Au NPs. Then, 55 mL of the resultant colloid was removed and kept apart, labelled as D1, which indicated the Au NPs synthesized from the first cycle.

The remaining colloid was used as seeds to proceed further growth on Au NPs in the second cycle. 52 mL of Milli-Q water and 2 mL of trisodium citrate solution (60 mM) were added to the colloid. After 30 minutes of stirring, a darker red solution could be observed. The process was repeated for another 2 more times to slowly increase the diameter of the Au NPs. Then, 55 mL of the resultant colloid was removed and kept apart, labelled as D2, which indicated the Au NPs synthesized from the second cycle. Several cycles were performed by using the same procedures until Au NP colloidal of D5 was obtained.

2-2-1-2 Direct citrate method

In the second method, Au NP sol (100 mL, 0.2 mM) was prepared by modified Turkevich method [Turkevich, 1951; Frens 1973]. In brief, 100 mL of $HAuCl_4$ (25 mM) was placed in round bottomed flask under reflux set up (**Fig. 2-2**). Once the solution commenced boiling, different amount (1 to 1.4 mL) of [1] trisodium citrate (39 mM) was added and stirred for 20 minutes. Accordingly, citrate-stabilized gold colloidal solution with different sizes was obtained.

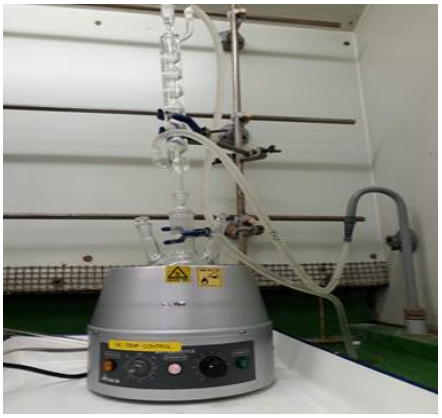

Fig. 2-2. Image of reflux system used for Au NPs synthesis.

2-2-2 Formation of Au@SiO_2 core-shells

Au NPs synthesized from direct citrate reduction method was used in the next steps as lesser time was consumed to form highly-monodispersed Au NPs in comparison to seeding method. Accordingly, hydrophobic properties of Au NPs, stabilized by citrate were changed to hydrophilic by γ-aminopropyltriethoxy silane (APS) as a primer [Liz-Marzan 1996]. A 0.25 mL portion of APS (1 mM) was added to 50 mL of the as-synthesized Au NPs and stirred at 240 rpm for 15 minutes, followed by addition of 2 mL of sodium-silicate solution (44 mM). The solution was stirred continuously for 48 hours for the formation of Au-NP@thinSiO_2 particles. The formation of Au@SiO_2 core-shells with high monodispersity in shape and diameter (minimum variation of < 5%) was achieved by using Stuber's method [Nassor 2011]. A 4 mL aliquot of Au-NP@thin-SiO_2 was stirred in the presence of 20 mL ethanol followed by dropwise addition of ammonia to increase pH value of the solution to 12. TEOS consisting of 10–30 mM (depending on the desired estimated thickness of SiO_2), was injected by using syringe pump at speed of 0.3 mL h^{-1} under the continuous of stirring. The solution was stirred for 60 or 90 minutes (**Table 2-1**) at room temperature for hydrolysis and condensation reactions. The resulting Au-NP@SiO_2 core-shell particles were washed three times with ethanol and separated by centrifugation. The optimization of sol-gel method was carried out to obtain particles with different thickness of SiO_2 ad to avoid the formation of coreless particles. The correlation between TEOS and resultant SiO_2 thickness was shown in **Fig. 2-3.** The red dot indicates the formation of coreless SiO_2 particles (**Fig. 2-3** inset image) which also resulted in polydispersity of particles.

Table 2-1. Experimental details on the formation of Au@SiO_2 core-shells in the fixed amount of catalyst.

Au-NP size (nm)	average SiO_2 thickness (nm)	TEOS (M)	stirring time (hour)
44	90	0.01	1
44	108	0.015	1
44	120	0.017	1
30	150	0.019	1
30	164	0.02	1
30	180	0.026	1.5
30	230	0.03	1.5

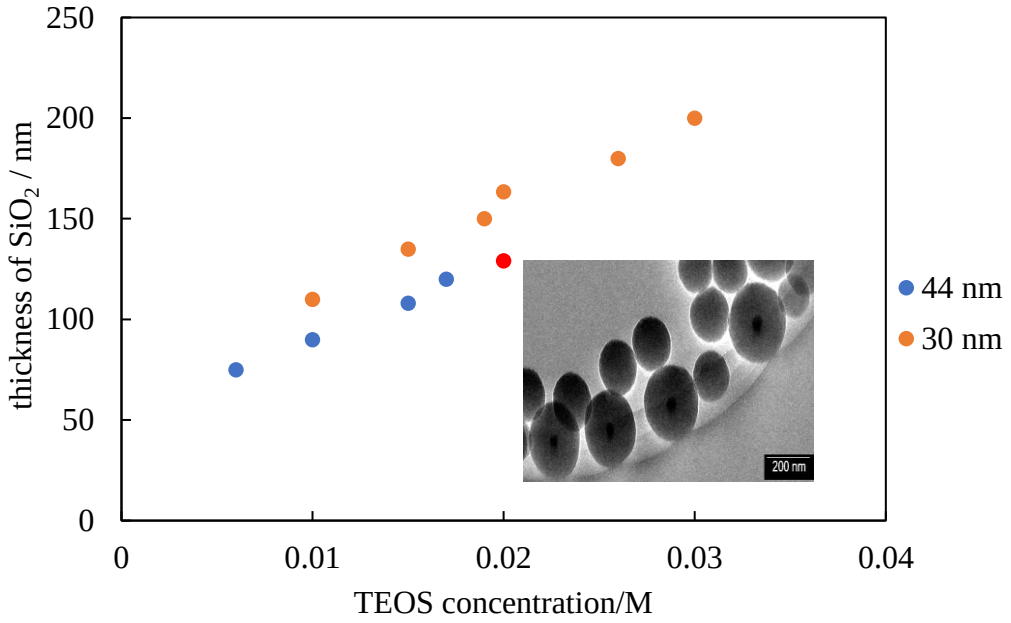

Fig. 2-3. Plot of dependence of SiO_2 thickness on TEOS concentration for two kind of Au NPs; 44 nm (blue) and 30 nm (orange); red dot indicated the formation of coreless particles.

2-2-3 Au-NP@SiO_2 opal formation

In the next step, powdered-opal structure was formed by self-assembly method. Self-assembly of Au-NP@SiO_2 particles was performed by sedimentation enhanced by centrifugation. Au-NP@SiO_2 core-shell particles suspended in ethanol solution was sedimented by a long, smooth and slow centrifugation (4000 rpm for 60 minutes), as illustrated in **Fig. 2-4**. Self-assembled Au-NP@SiO_2 opals were calcined at 300 ºC for 2 hours to strengthen the mechanical stability and allow the formation of necks among the particles [Miguez 1998].

2-2-4 Titania infiltration into opal

In order to obtain the backbone skeleton of the PCs, titania infiltration into the voids of the opal was carried out. Accordingly, forced impregnation method was applied to infiltrate TiO_2 precursor into the voids [Chen, 2010]. Calcined opals were soaked in methanol for about 10 minutes. Then, the infiltrated powdered-opal samples were immediately transferred to a test tube containing a titania precursor, titanium (IV) isopropoxide. The test tube was connected to a vacuum system. Under vacuum pressure, methanol was evaporated, allowing the precursor to fill up the voids. The samples were dried at 323 K for 12 hours, which the drying and infiltration process were repeated for three times to achieve efficient TiO_2 network formation. Later, the samples were calcined at 500 ºC with temperature ramping of 3 K min^{-1} to crystallize amorphous titania.

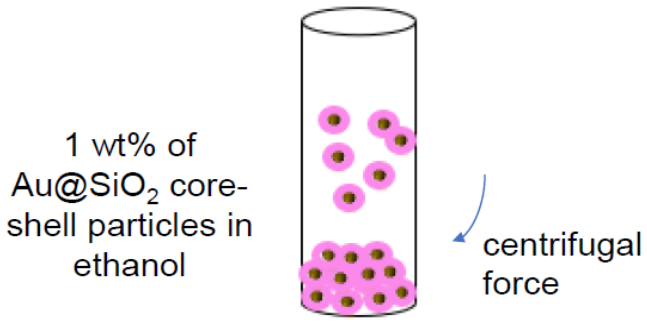

Fig. 2-4. Schematic illustration of vertical self-assembly to form three-dimensional Au-NP@SiO_2 opal.

2-2-5 Selective etching of SiO_2

In order to obtained the final desired photocatalysts design, SiO_2 template (opal) was etched from the infiltrated opal ($Au@SiO_2/TiO_2$). The TiO_2-infiltrated samples was put into a beaker containing 20 mL sodium-hydroxide solution (2M). Then, the samples were etched for 48 hours at room temperature. The etched samples were washed for multiple times with Milli-Q water and dried at 40 ºC for 12 hours, resulted in the final three-dimensional Au-NP@IOT photocatalysts.

2-3 Preparation of IOT samples

Bare TiO_2 IO (IOT) samples were prepared in order to study the photocatalytic activity performance without plasmonic effect from Au NPs. IOT samples were prepared by same methods as described for Au-NP@IOT samples, but without Au-NPs. Coreless SiO_2 NPs with different diameters were synthesized by Stober's method by varying amount TEOS precursor (6 mL to 7.5 mL). The formation of SiO_2 opal, TiO_2 infiltration and selective etching of SiO_2 were performed by the same procedures, as those described in **Section 2-2-3, 2-2-4** and **2-2-5** respectively.

2-4 Au-NP@IOT-like multiarray structure

In comparison to Au-NP@IOT samples, Au-NP@IOT-like multiarray structure was also prepared, i.e., $Au@SiO_2$ core-shell particles were infiltrated with TiO_2 precursor prior self-assembly. This procedure was used to check if it was possible to prepare opal and invsere opal structures from $Au\text{-}NP@SiO_2/TiO_2$. Upon the TiO_2 infiltration, the resulting $Au\text{-}NP@SiO_2/TiO_2$ particles were let for self-assembly, followed by calcination to crystallize TiO_2 and removal of SiO_2 template by using concentrated NaOH aqueous solution. The obtained sample was labelled as Au-NP@IOT-like multiarray structure.

2-5 Preparation of crushed Au-NP@IOTs

In order to prepare a reference sample without inverse opal structure, Au-NP@IOT samples were crushed and brayed by using an agate mortar for 15 minutes.

2-6 Preparation of three-dimensional IOT samples loaded with Au NPs

Au NPs loaded on the surface of IOT samples were prepared as the reference samples for the developed novel structured photocatalysts, Au-NP@IOTs. Two methods were attempted to prepare those reference samples, i.e., hydrothermal and photodeposition methods.

2-6-1 Hydrothermal method

Firstly, hydrothermal method was attempted to prepare the Au-NP loaded on IOT sample. IOT sample was put in the Teflon autoclave. Then, 0.6 mL of $HAuCl_4$ (0.01 mM) comprising of 5 wt% of Au respective to IOT, was added to a solution of 2 mL methanol dissolved in 40 mL of deionized water. The pH value was adjusted to 10 by dropwise addition of ammonia. The Teflon autoclave was sealed and heated at 120 °C for 1 hour. Then, the sample was washed with Milli-Q water and dried at 50 °C. The obtained sample was labelled as HM-Au/IOT.

2-6-2 Photodeposition method

In the photodeposoition method, 5 mL of methanol (50 v/v%) and $HAuCl_4$ (97 mM, comprising of 0.1 wt%, 0.5 wt%, 2 wt% and 5 wt% of Au in respective to TiO_2) was added into a test tube containing 50 mg of bare IOT sample. The sample was bubbled with argon for 15 minutes prior the photoirradiation. The irradiation system set up for photodeposition was illustrated in **Fig. 2-5**. Photoirradiation was performed with a 400-W high-pressure mercury

lamp under continuous Argon bubbling. The obtained samples (labelled as PD-Au/IOTs) were washed with methanol and deionized water, followed by drying at 50 °C for 12 hours.

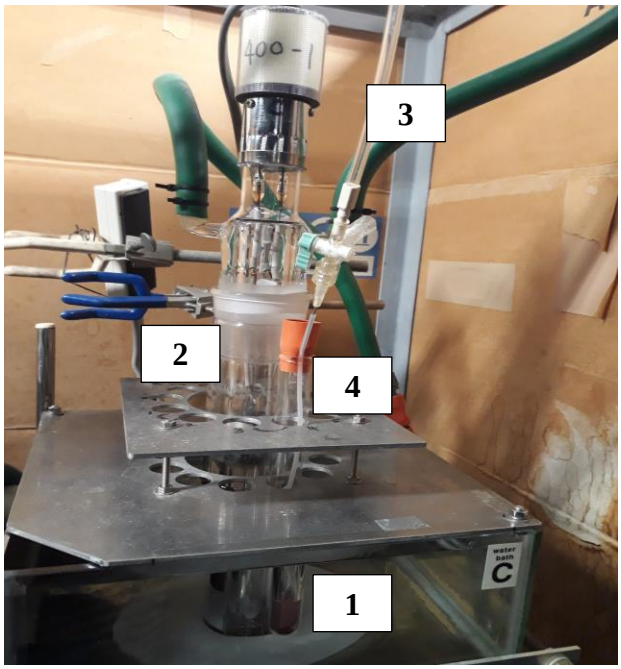

Fig. 2-5. Image of irradiation system used for gold photodeposition on IOT; [1] water bath, [2] mercury lamp, [3] argon bubbling, [4] test tube containing IOT and gold precursor.

2-7 Characterisations

Photoabsorption properties were measured for both liquid and solid samples using two spectrophotometers. UV-visible spectra of liquid samples (Au colloids) were recorded on a Shimadzu multipurpose spectrophotometer UV-MPS 2450, equipped with a high-performance single monochromator and a double beam photometric system in absorbance mode. Samples were inserted in a quartz cell with a light path of 10 mm. Diffuse reflectance spectra of solid samples were measured by an ultraviolet and visible spectrophotometer (JASCO V-670) equipped with an integrating sphere unit PIN-757 for diffuse-reflectance measurement. Spectra in the wavelength range of 200–800 nm were recorded with a scanning rate of 200 nm min^{-1}, bandwidth of 5.0 nm and data uptake interval of 1.0 nm. Barium sulfate ($BaSO_4$) was used as a reference.

Crystal properties were analyzed with a Rigaku Intelligent XRD system, SmartLab, equipped with a sealed tube X-ray generator (a copper target, 40 kV, 30 mA), a D/teX high-speed position-sensitive detector system and an ASC-10 automatic sample changer with measurement conditions of 2θ range of 10–90°, scan speed of 1.00° min^{-1} and scan step of 0.008°. XRD patterns were analyzed by Rigaku PDXL crystal structure analysis package including Rietveld analysis.

The morphology of samples was investigated by low-vacuum scanning electron microscopy (LV-SEM) and transmission electron microscopy (TEM). LV-SEM measurement was performed with JEOL JSM-6360LA under the conditions of 10-mm working distance and10-kV electron-acceleration voltage. Images were obtained at different magnifications (300–33000) in an SEI imaging mode. Powder was deposited on a piece of copper tape attached to a brass sample holder. TEM observations were performed by JEOL JEM-2100F with electron-acceleration voltage of 200 kV. A droplet of colloidal suspension was deposited on a collagen coated-copper grid. The grids were dried overnight under vacuum. Images were obtained at different magnifications (1000–600000).

Flame atomic absorption spectroscopy (FAAS, Shimadzu AA-6200) was used to quantify the amount of Au NP incorporated in Au-NP@IOT samples. Firstly, calibration of gold was carried out using $HAuCl_4 \bullet H_2O$ precursor diluted with aqua regia (10 v/v%). 10 mg of sample was treated with aqua regia under continuous stirring for 1 hour and separated by centrifugation. The procedure was repeated to ensure dissolution of all gold. The solid precipitate was separated, whereas the supernatant was mixed with first supernatant. The concentration of gold was estimated in diluted supernatant (with Milli-Q water) accordingly to the calibration that was carried out.

2-8 Photonic band gap (PBG) calculations

PBG peak positions of all Au-NP@IOT samples were calculated by Bragg's law formula:

$$\lambda_{max} = (8/3)^{1/2} D (n^2_{eff}\text{-}\sin^2 \theta)^{1/2},$$

where λ_{max} is the wavelength of the stopband maximum, D is the diameter of the nanovoid, n_{eff} is the effective refractive index, and θ is the angle between the incident and reflective surfaces.

The value of n_{eff} was estimated by using the refractive index of TiO_2 (n =2.48, taking into consideration the anatase form [Curti 2017], which was proven by XRD analysis) and water (n = 1.33). For convenience, an angle of 45º (θ) was taken, as random angle directions were expected for the samples in powder-oriented. Considering an appreciable distribution of void size, PBG position wavelength for each sample was calculated by assuming a Gaussian distribution of size with its standard deviation, as shown in **Fig. 3-24**. Accordingly, the estimated PBG positions had a relatively wide distribution of wavelength ranges, due to both actual incident-beam angle and void-size distributions. The blue-edge wavelengths were considered, for convenience, by employing 0–25% probability range of wavelengths from the Gaussian plots, as shown in **Fig. 3-25**.

2-9 Photocatalytic activity test

Oxidative decomposition of acetic acid was performed in a quartz cell with a volume of 14.5 mL, containing 3 mL of acetic acid (5 v/v%) in the presence of 15 mg of Au-NP@IOT sample under monochromatic blue LED (λ=450 nm; optical power of 0.3 W) or green LED (λ=530 nm; optical power of 0.1 W) irradiation for 4 hours. Photocatalytic activity of Au-NP@IOT samples were tested under non-stirring (without agitation of the photocatalyst) and stirring conditions. Before the photocatalytic reaction, the sample was kept in the dark for 2 hours to allow adsorption and desorption equilibrium. The generated CO_2 was monitored using a Shimadzu GC-8A gas chromatograph equipped with a TCD and a Porapak-Q column.

2-10 References

Bastus, N. G.; Comenge, J.; Puntes, V. Kinetically controlled seeded growth synthesis of citrate-stabilized gold nanoparticles of up to 200 nm: Size focusing versus Ostwald ripening. *Langmuir* **27**, 11098–11105 (2011).

Chen, X.; Li, Z.; Ye, J.; Zou, Z. Forced impregnation approach to fabrication of large-area, three-dimensionally ordered macroporous metal oxides. *Chem. Mater.* **22,** 3583–3585 (2010).

Curti, M.; Mendive, C. B.; Grela, M. A.; Bahnemann, D. W. Stopband tuning of TiO_2 inverse opals for slow photon absorption *Mater. Res. Bull.* **91,** 155–165 (2017).

Deparis, O.; Moucheta, S. R.; Su, B.-L. Light harvesting in photonic crystals revisited: Why do slow photons at the blue edge enhance absorption? *Phys. Chem. Chem. Phys.* **17**, 30525–30532 (2015).

Frens G. Controlled nucleation for the regulation of the particle size in monodisperse gold suspensions, Nature Physical Science, **241**, 20–22 (1973)

Liz-Marzan, L. M.; Giersig, M.; Mulvaney, P. Synthesis of nanosized gold-silica core-shell particles. *Langmuir* **12,** 4329–4335 (1996).

Meseguer, F.; López, C.; Blanco, A.; Moya, J. S.; Requena, J.; Mifsud, A.; Fornés, V. Control of the photonic crystal properties of fcc-packed submicrometer SiO_2 spheres by sintering. *Adv. Mater.* **10,** 480–483 (1998).

Nassor, E. C. O.; Ávila, L. R.; Pereira, P. F. S.; Ciuffi, K. J.; Calefi, P. S.; Nassar, E. J. Influence of the hydrolysis and condensation time on the preparation of hybrid materials. *Mat. Res.* **14,** 1–6 (2011).

Turkevich, J.; Stevenson, P. C.; Hillier, J. A study of the nucleation and growth processes in the synthesis of colloidal gold. *Discuss. Faraday Soc.* **11**, 55–75 (1951).

Chapter 3

Formation, characterization and PBG calculation of Au-NP@IOTs

3-1 Introduction

In this chapter, the formation of Au-NP@IOTs by five-step procedures has been discussed in details along with the morphology and optical study for each sample. Apart from that, the calculated PBG peak positions and estimation of PBG edge wavelengths have been presented for all samples prepared.

3-2 Formation of Au-NP@IOT photocatalysts

3-2-1 Synthesis of Au-NPs

Turkevich method [Turkevich 1951] has been recognized as one of the pioneer methods to synthesize Au NPs with various sizes by allowing chemical reaction between gold precursor and trisodium citrate. Trisodium citrate as stabilizing agent and reducing agent was able to control the diameter and shape of the formed Au NPs [Dobrowolska 2015].

In this study, two Turkevich-based synthesis methods have been attempted, i.e., seeding method (Bastus 2011) and direct citrate reduction method which the former method allowed a progressive and slow growth of Au NPs, resulting in NPs with controlled shapes and diameter whereas direct citrate reduction method has been carried out by varying the ratio between the

gold precursor and the capping agent, trisodium citrate. The general concept for both the methods would be addition of trisodium citrate into boiling gold precursor under reflux system for direct citrate reduction method and the vice-verse procedure for seeding method. Similarly, the colour changes could be observed based on the diameter of Au NPs that were formed.

3-1-1-1 Seeding method

The diameter of the Au NPs increased gradually by consequent addition of Au precursor to the boiling citrate solution in the interval of 30 minutes, resulting in the formation of seed colloidal (at the 1st cycle) followed by Au NPs colloidal with D (diameter) 1, D2, D3, D4 and D5 as the cycle number increases. The colour of the Au NPs became darker as the growth and diameter of the Au NPs progressed in each cycle as shown in **Fig. 3-1**.

As could be observed from **Table 3-1** and **Fig. 3-2,** the red-shifting was evident as the LSPR wavelength increased with the diameter of Au NPs along with the formation of broader peaks. The Au colloidal seeds absorbed the visible light primarily due the smaller optical cross sections resulting in weak absorbance at ca. 519 nm. In the other hand, greater electrons' mean free path experienced in larger particles resulted in higher absorbance as the diameter of Au NPs increased from seed to D5 (Haiss 2007).

Although seeding method could produce diameter controlled Au NPs, lot of time has been consumed as the method required progressive addition of precursor in each cycle and intervals. Hence, a less time-consuming method (direct citrate reduction) that could also synthesize Au NPs with similar narrow distribution has been attempted and used for the rest of the study.

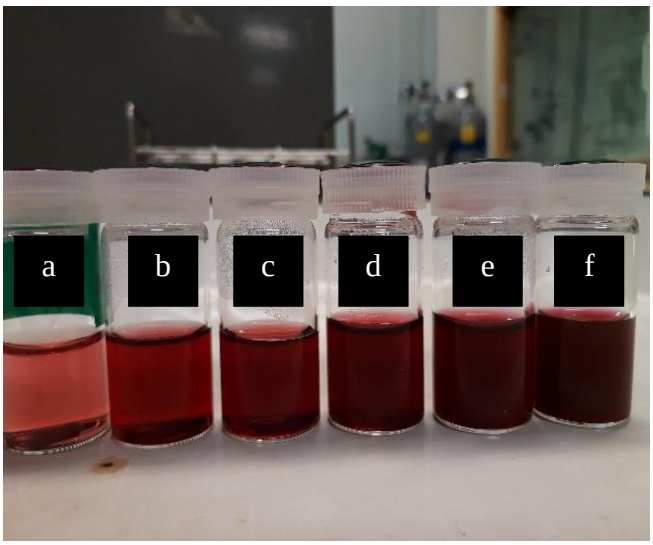

Fig. 3-1. Images of Au NP colloids of (a) seed(b) D1-Au-NPs (c) D2-Au-NPs (d) D3-Au-NPs (e) D4-Au-NPs (f) D5-Au-NPs which were synthesized from seeding method.

Table 3-1. LSPR wavelength and absorbance measured for Au NPs synthesized from seeding method.

Au NPs	LSPR peak wavelength/nm	absorbance
seed	519	0.11
D1	521.5	0.51
D2	522.5	0.81
D3	526.5	1.04
D4	529.5	1.05
D5	536	1.25

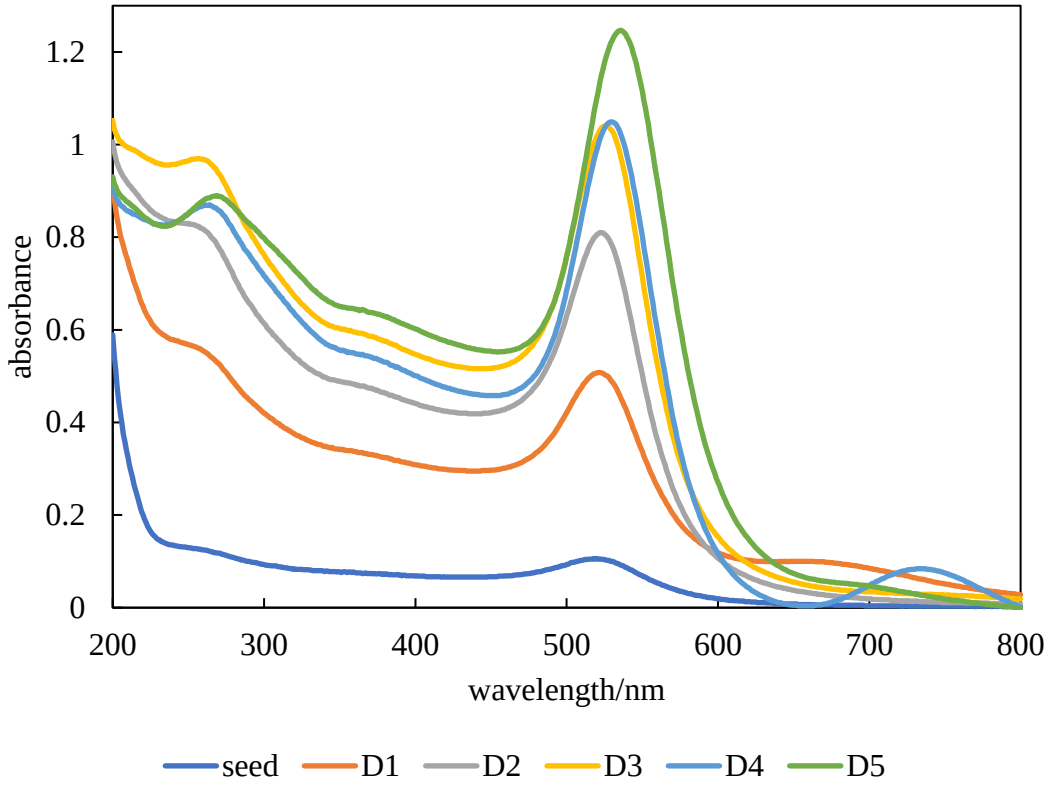

Fig. 3-2. UV-Vis spectra of Au NPs synthesized through seeding method.

3-1-1-2 Direct citrate reduction method

In the other hand, citrate reduction method has been also attempted by varying the amount of capping agent to evident Au NPs with different diameter. In brief, trisodium citrate reduces Au (III) ions to Au (0) resulting in a formation of ruby-red colloidal solution which indicates the formation of zero-valent Au NPs as the citrate molecules are oxidized (**Fig. 3-3)**.

Au NP with average dimeter of 20 nm has been synthesized with LSPR absorbance at ca. 520 nm, whereas Au NPs with average diameter of 30 nm and 44 nm were formed as the amount of reducing agent (trisodium citrate) was reduced (Dong 2020). **Fig. 3-4 (a) and (b)** shows TEM images obtained for Au NPs with average diameter of 30 nm and 44 nm, respectively, and in spherical and faceted hexagonal shape which has been utilized for the further steps. The distribution of particle diameter is presented in **Fig. 3-4 (c) and (d),** indicating the moderately narrow distribution of the formed Au NPs.

Fig. 3-3. Photograph of Au NPs' colloidal solution with average particle diameter of 30 nm (left) and 44 nm (right).

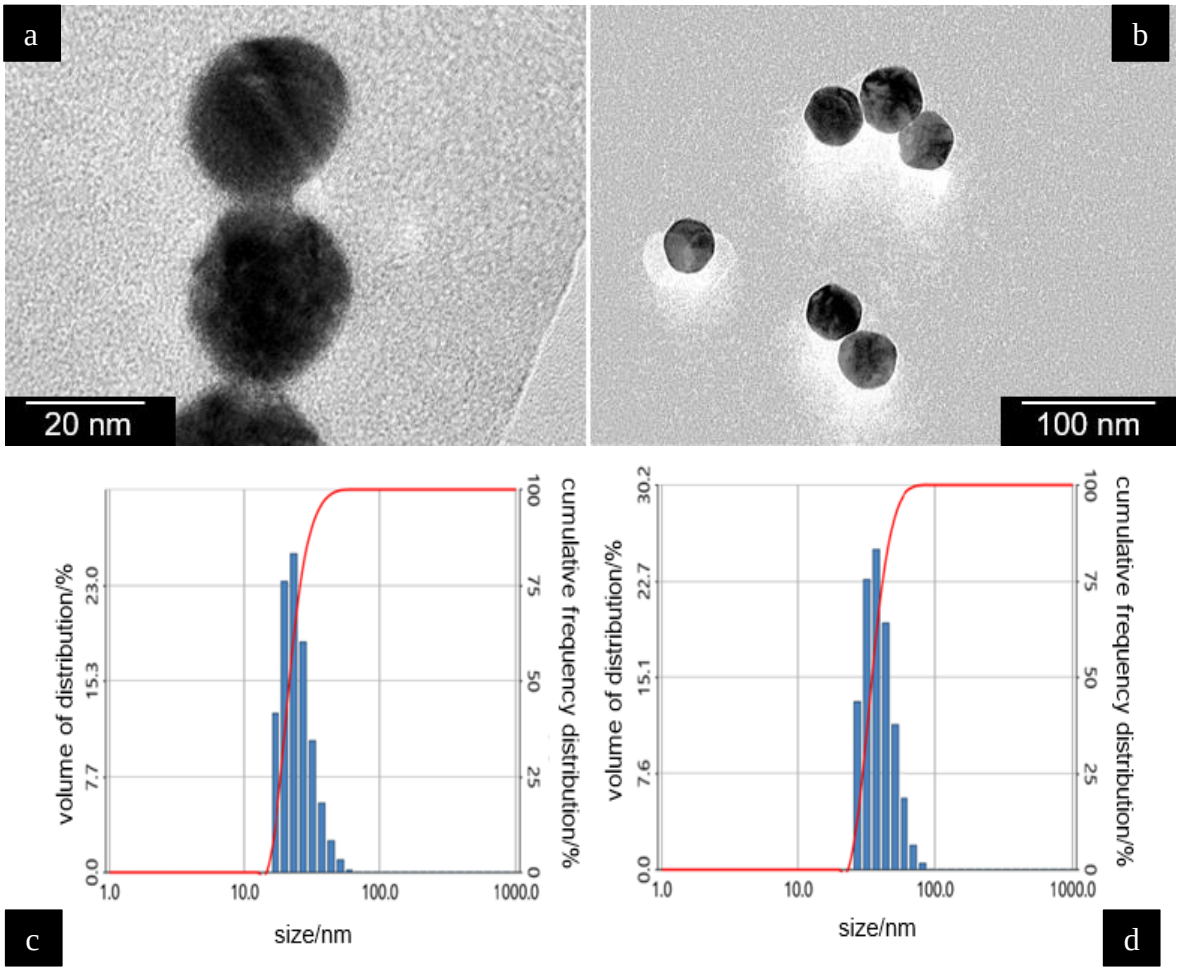

Fig. 3-4. (a-b) TEM images of Au NPs with average diameter of 30 nm and 44 nm and (c-d) distribution of Au NPs' diameter for samples shown in image (a) and (b), respectively.

The formation of Au NPs has been confirmed by photoabsorption spectra as clear LSPR peak is observed in **Fig. 3-5**. The position of LSPR peak differs slightly for all three samples with max absorption at 520 nm, 528 nm and 533 nm for Au NPs of 20, 30 nm and 44 nm size, respectively, which is reasonable considering spherical shape and similar sizes of Au NPs. It is known that SPR depends on the size and the shape of NPs (bathochromic shift with an increase in the size and deviations from spherical shape), the metal kind, and refractive index of the medium [Chen 2008]. Accordingly, for spherical gold NPs of 20-50-nm diameter, LSPR (measured in water/air) appears at ca. 520-540 nm [Lim-Marzan 2016]. The average crystallite size estimated from XRD analysis (presented in **Table 3-2**) was 10 nm (± 2 nm) and 20 nm (± 3 nm) for Au-NP with average diameter of 30 nm and 44 nm, respectively, suggesting that Au NPs are formed from three and two crystallites.

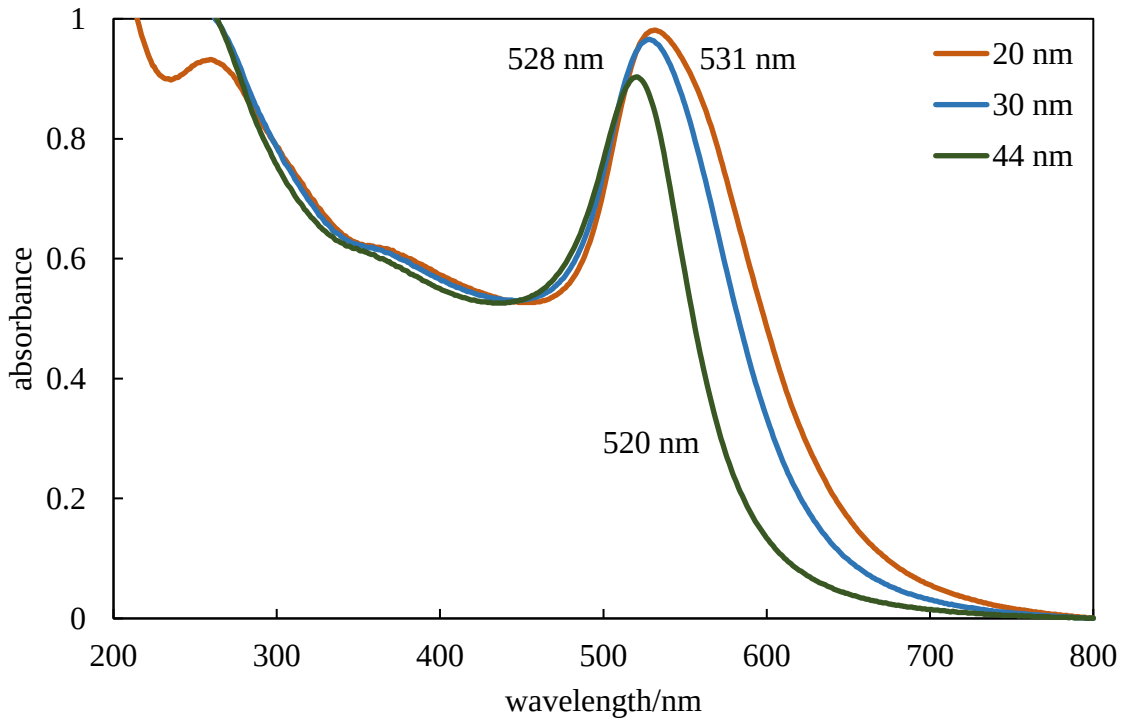

Fig. 3-5. UV-vis spectra of Au NPs with different average diameter of 20 nm, 30 nm and 44 nm.

3-1-2 Formation of Au@SiO_2 core-shells

The vitrophobic characteristic of Au NPs, stabilized by citrate, [Lim-Marzan 1996], has been changed into vitrophilic one by γ-aminopropyltriethoxy silane (APS) as a primer. Moreover, addition of APS helped in obtaining stable colloids as modification of the surface and electrostatic properties is needed during solvent transfer (from water to ethanol) for formation of SiO_2 shell. The modification of the Au NPs resulted in the formation of thin SiO_2 shell with average thickness of 5 nm as pointed out in **Fig. 3-6**. It is considered that growth of a thin SiO_2 layer is vital to avoid aggregation and the formation of secondary Au particles.

UV-vis spectra have been obtained for both Au NPs with coated with thin SiO_2 shell as in **Fig. 3-7**. As mentioned earlier, LSPR peak could be altered and shifted depending on the shape, size and environment. Slight red shift in LSPR maximum wavelength could be evident for both samples although it was more obvious for the smaller Au NP (30 nm) as could be seen in **Fig. 3-7(a)**.

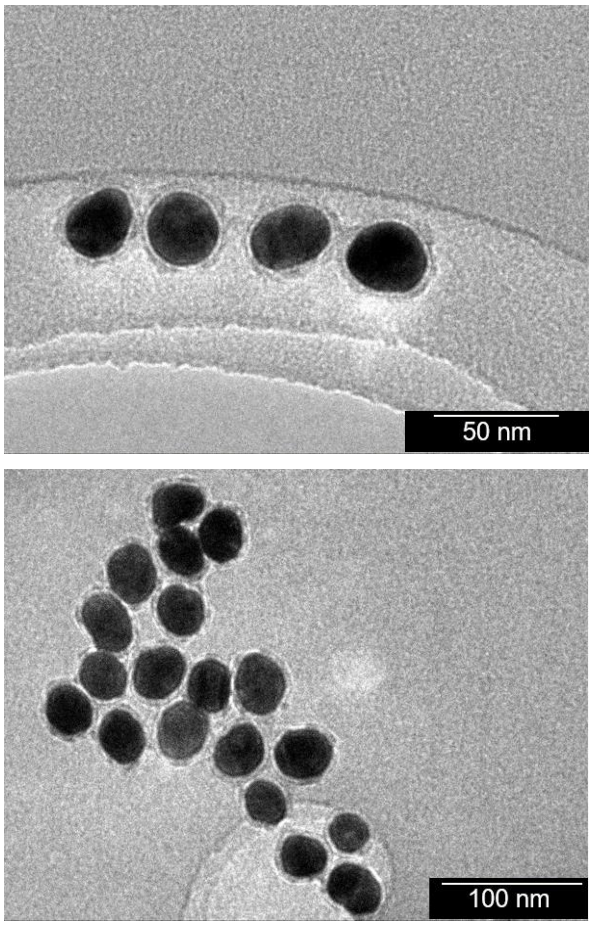

Fig. 3-6. TEM images of Au-NP@SiO_2 core-shells with thin SiO_2 shell.

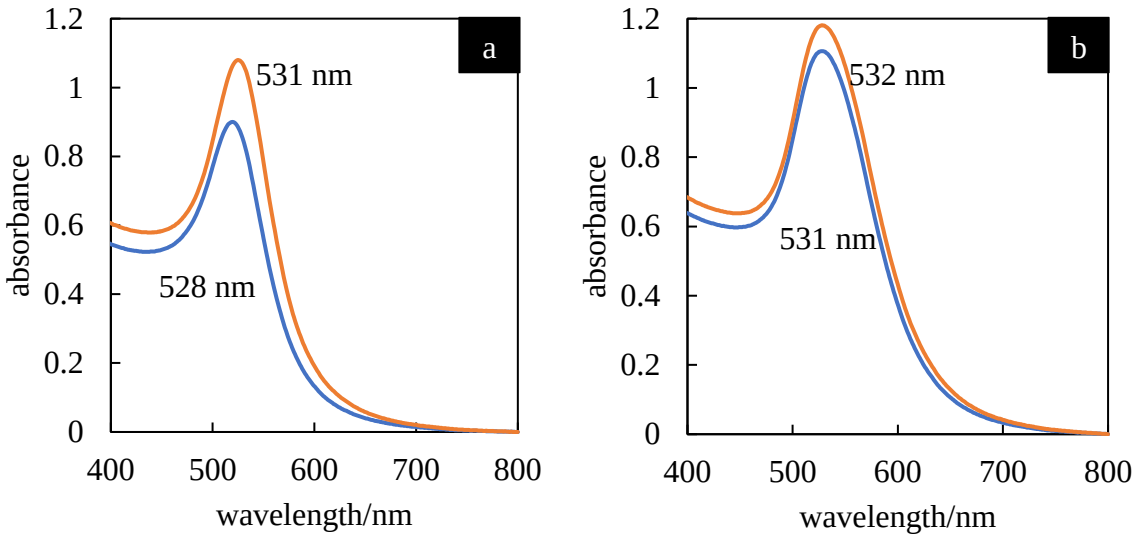

Fig. 3-7. UV-vis spectra of Au NPs (blue) and Au@thinSiO_2 (orange) representing Au NPs with average diameter of (a) 30 nm (b) 44 nm.

The formation of Au@SiO_2 core-shells with high monodispersity in the shape and diameter (minimum variation of < 5 %) has been achieved by Stuber's method, as shown in **Fig. 3-8**. The main advantage of the spherical shaped Au NPs with similar sizes is their ability to serve as building blocks for high quality formation of three-dimensional opal template. It should be pointed out that this step is determinantal for successful preparation of the final opal structure since various factors affect the formation and properties of Au@SiO_2 particles, including the amount of used catalyst (ammonia), concentration of SiO_2 precursor (tetraethyl orthosilicate (TEOS); to vary the shell thickness), polymerization time and the size of the Au NPs' cores [Nassor 2011 / Montano-Priede 2017]. It has been found that for larger Au NPs (> 44 nm), monodispersed Au@SiO_2 core-shells without coreless SiO_2 are difficult to be formed, but this is crucial for formation of opal. The role of ammonia as catalyst for the hydrolysis of TEOS molecules to form silanol groups which subsequently polymerizes via crosslinking, is also important for growth of SiO_2. For example, addition of too high amount of ammonia and too long stirring time (polymerization time) lead to formation of secondary SiO_2 particles with unreacted TEOS molecules causing the formation of coreless particles which is highly unfavorable for opal formation as indicated in **Fig. 2-3** in **Chapter 2**.

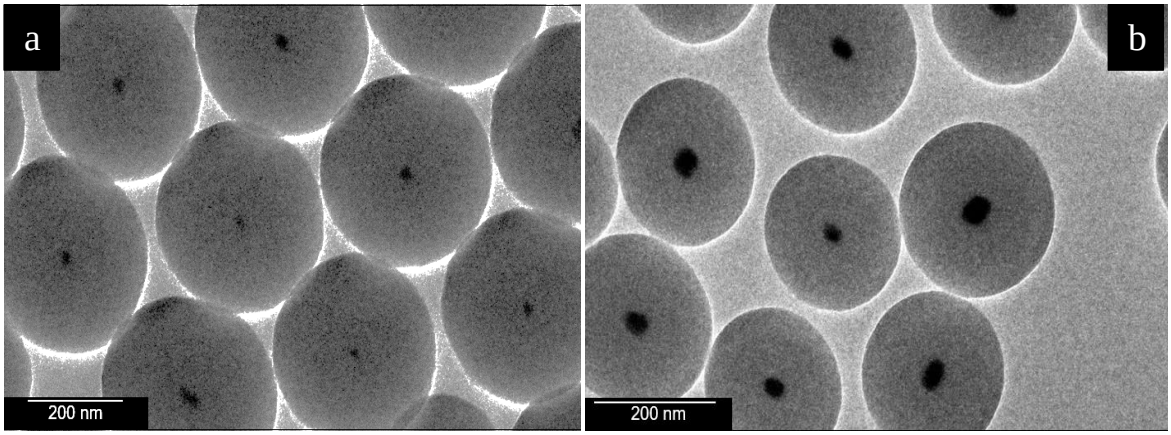

Fig. 3-8. TEM image of Au-NP@SiO_2 core-shells with diameter of (a) 330 nm (Au NPs = 30 nm) and (b) 220 nm (Au NPs = 44 nm).

3-1-3 Au-NP@SiO_2 opal formation

The closely packed opal of face-centered cubic (FCC) structure has been obtained by self-assembly method via centrifugation-accelerated sedimentation of Au@SiO_2 particles dispersed well in ethanol, followed by annealing to: (i) provide mechanical stability, (ii) remove the remaining water, and (iii) form a neck between particles [Miguez 1998]. It should be pointed out that lack of calcination resulted in disordered formation of the TiO_2 network. An exemplary structure of 20-µm thick opal with more than 50 layers of core-shell particles assembled in ordered manner is shown in **Fig. 3-9**. Although, some cracks probably resulting from thermal treatment [Hatton 2010], and small broken parts (caused by removal of the opal from centrifuge tube) could be observed, the ordered structure has still maintained (**Fig. 3-10**). In order to confirm the presence of Au NPs inside SiO_2, TEM images were taken, as shown **Fig. 3-11**. Indeed, core-shell structure of Au@SiO_2 opal has been confirmed.

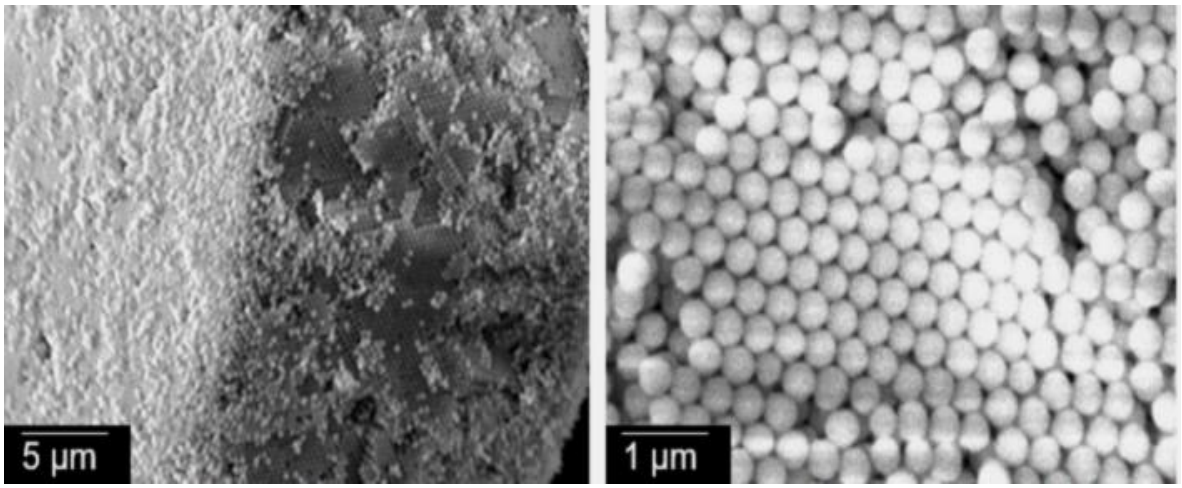

Fig. 3-9. LV-SEM images of opal with closely packed Au@SiO_2 core-shells particles.

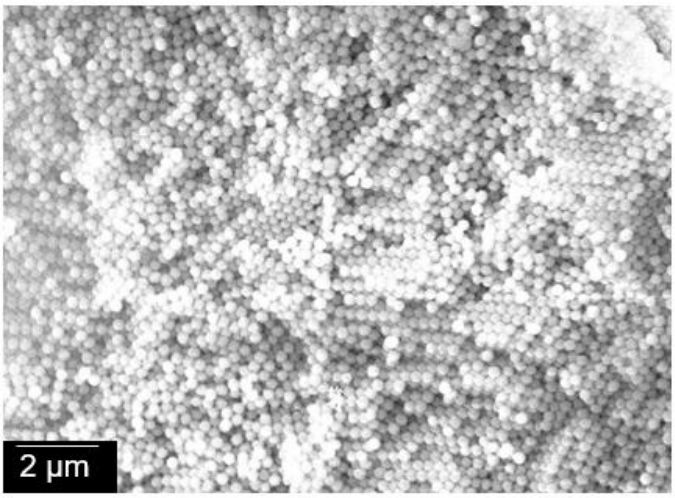

Fig. 3-10. LV-SEM image of broken Au@SiO_2 opal.

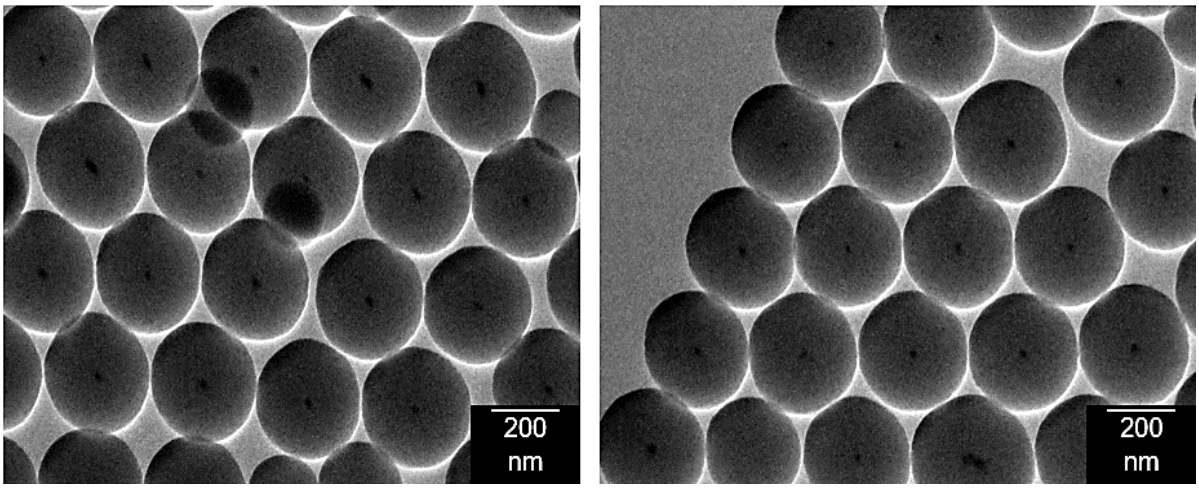

Fig. 3-11. TEM images of assembled Au@SiO_2 core-shells particles.

The importance of the minimum variation in particle morphology (i.e., size and shape) was further investigated by allowing self-assembly for core-shells with high polydispersity. Indeed, the low-quality opals of large void gaps between the particles was obtained as shown in **Fig. 3-12**. It should be pointed out that disordered template/incomplete opal would lead to disordered formation of inverse opal, which might induce the loss of the photonic effect.

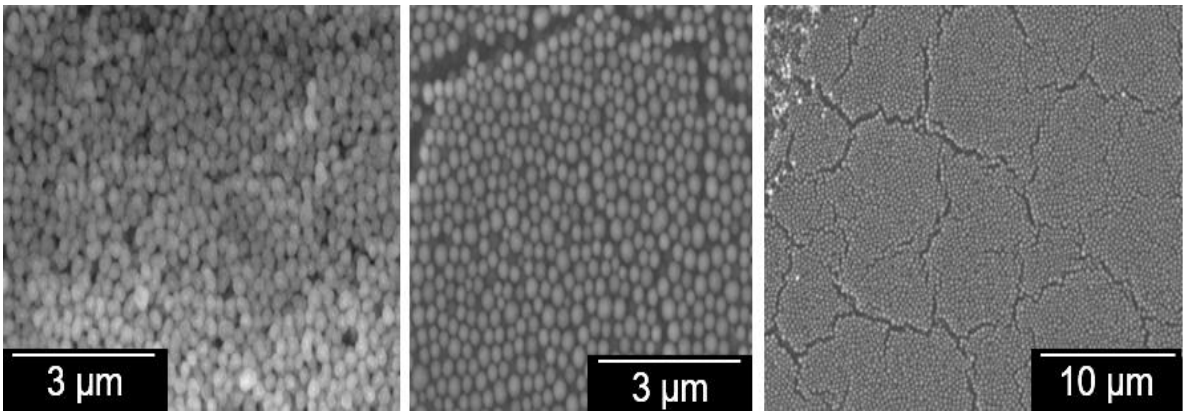

Fig. 3-12. LV-SEM image obtained for self-assembly of Au/SiO_2 core-shells with maximum variation in size and shape.

3-1-4 Infiltration of TiO_2 into powdered opal template

TiO_2 infiltration has been achieved via forced impregnation method under vacuum [Chen 2010], which allows the penetration of titania precursor between SiO_2 particles as shown in **Figs. 3-13 (a-c)**. The ability of the viscous precursor to penetrate the void spaces is crucial to form a high-quality TiO_2 network considering the thickness of the opal. It should be pointed out infiltration of titania precursor inside opal structure is quite difficult, and thus vacuum must be applied for successful formation of Au@SiO_2/TiO_2 structure. For example, TiO_2 formed in the normal infiltration method apart from the inhomogeneous covering of the surface of the opal as shown in **Fig. 3-13 (d)**. Au@SiO_2/TiO_2 was calcined to obtain the crystalline form of titania, anatase, as proven by XRD analysis (**Section 3-2-2**).

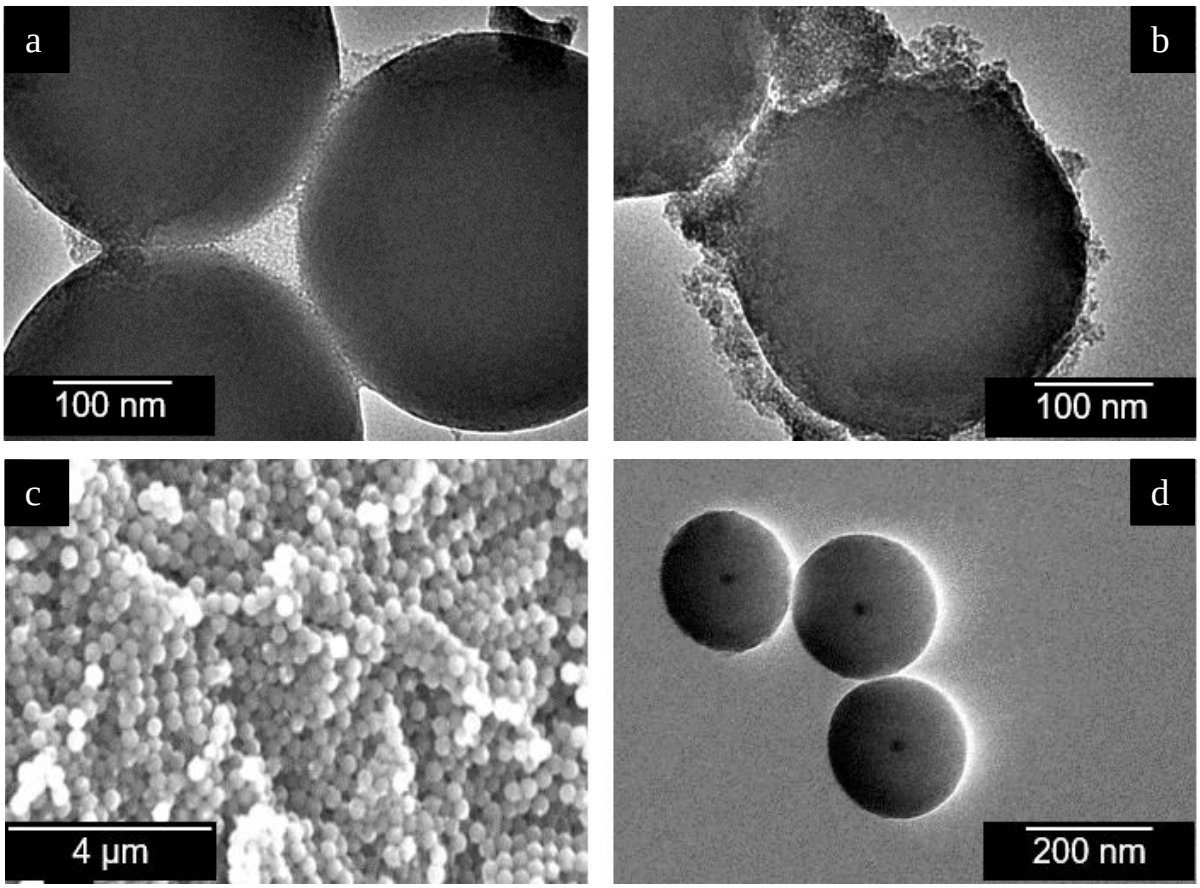

Fig. 3-13. TEM images of (a-b) bare SiO_2 opal infiltrated by forced impregnation method, (d) Au/SiO_2 infiltrated with TiO_2 without vacuum, (c) LV-SEM image of Au/SiO_2 infiltrated with TiO_2 infiltrated by forced impregnation method.

EDX analysis has been carried out for Au-NP@SiO_2/TiO_2 to observe the qualitative content present in the sample. As could be seen in **Fig. 3-14**, high intensity (counts) has been detected for elements of Si (ca. 1.7 keV) and O (ca. 0.5 keV) along with appreciable detection for Ti (ca. 4.5 keV), indicating the successful infiltration of TiO_2 on the Au@SiO_2 opal as negligible Ti detection was observed for sample infiltrated without vacuum. It should be noted that Au peak (ca. 2.1 keV) could not be significantly detected due to the thickness of SiO_2 and TiO_2 formation (**Fig. 3-15**).

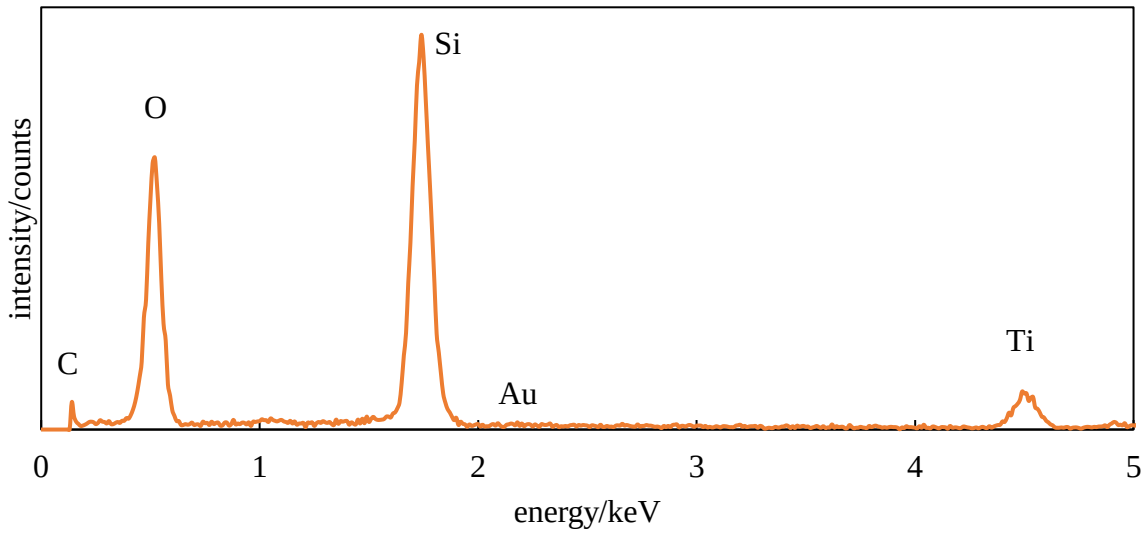

Fig. 3-14. EDX analysis of Au-NP@SiO_2/TiO_2.

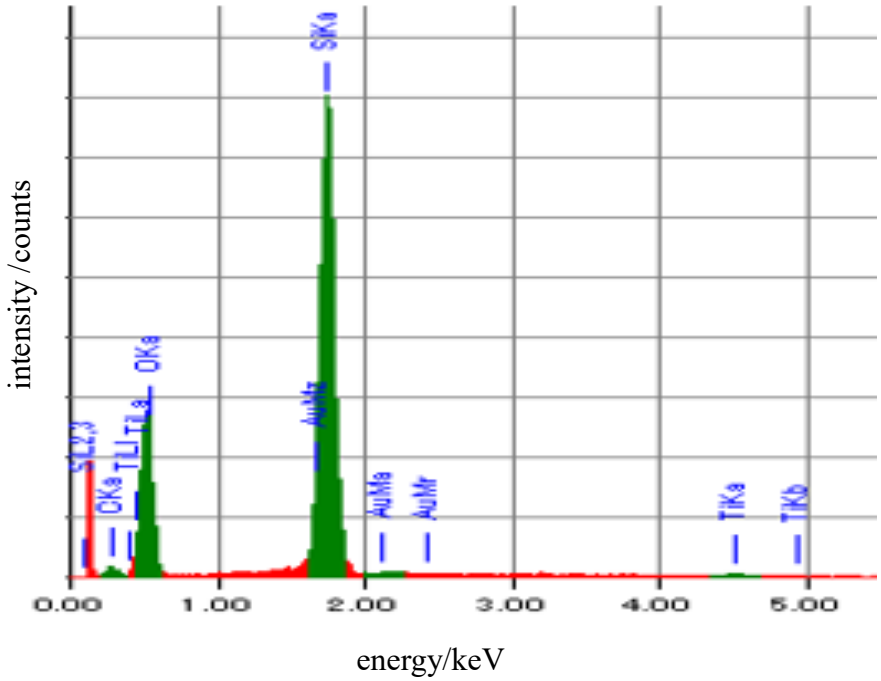

Fig. 3-15. EDX analysis of Au/SiO_2 sample infiltrated with TiO_2 without vacuum.

3-1-5 Selective etching of SiO_2

As the final step, the Au-NP@IOT structure has been formed via base treatment of $Au@SiO_2/TiO_2$ to remove the SiO_2 template. **Table 3-2** shows the Au-NP@IOT samples that were successfully prepared by varying the SiO_2 thickness during the formation of $Au@SiO_2$ core-shell particles. The inverse opal structures could be observed in **Fig. 3-16** with clear sphere contact points marked in **Fig. 3-17 (b)**. The multilayers of periodic structure clearly seen in **Fig. 3-17 (c),** which fulfils the requirement of a good photonic crystal, since light trapping is enhanced as the number of layer increases. The most importantly, Au NPs have remained in the voids even after SiO_2 removal. Few TiO_2 overlayers could be observed, due to the gelation process of the excess precursor on the surface of the infiltrated samples [Chiang 2016]. Shrinkage in the volume fraction (15-30%) of all Au-NP@IOT samples has been observed since the void diameter is reduced during titania calcination (in the comparison with original diameter of SiO_2 template), similarly to previous findings [Wang 2019 / Li 2018]. EDS analysis (**Fig. 3-17 (e)**) proved the efficiency of the alkaline etching method as the trace of SiO_2 was almost negligible.

Table 3-2. Details of Au-NP@IOT samples varying with nanovoid and Au NP diameter.

sample	nanovoid diameter (nm)	$LSPR_{max}$ (nm)	Au-NP	
			*crystallite size (nm)	particle size (nm)
Au-NP@IOT-150	150	531	17.3	44
Au-NP@IOT-200	200	531	20.6	44
Au-NP@IOT -215	215	531	22.2	44
Au-NP@IOT -240	240	528	12.2	30
Au-NP@IOT -250	250	528	10.9	30
Au-NP@IOT -270	270	528	11.8	30
Au-NP@IOT -290	290	528	10.9	30

*Au NP crystallite size determined for Au (111)

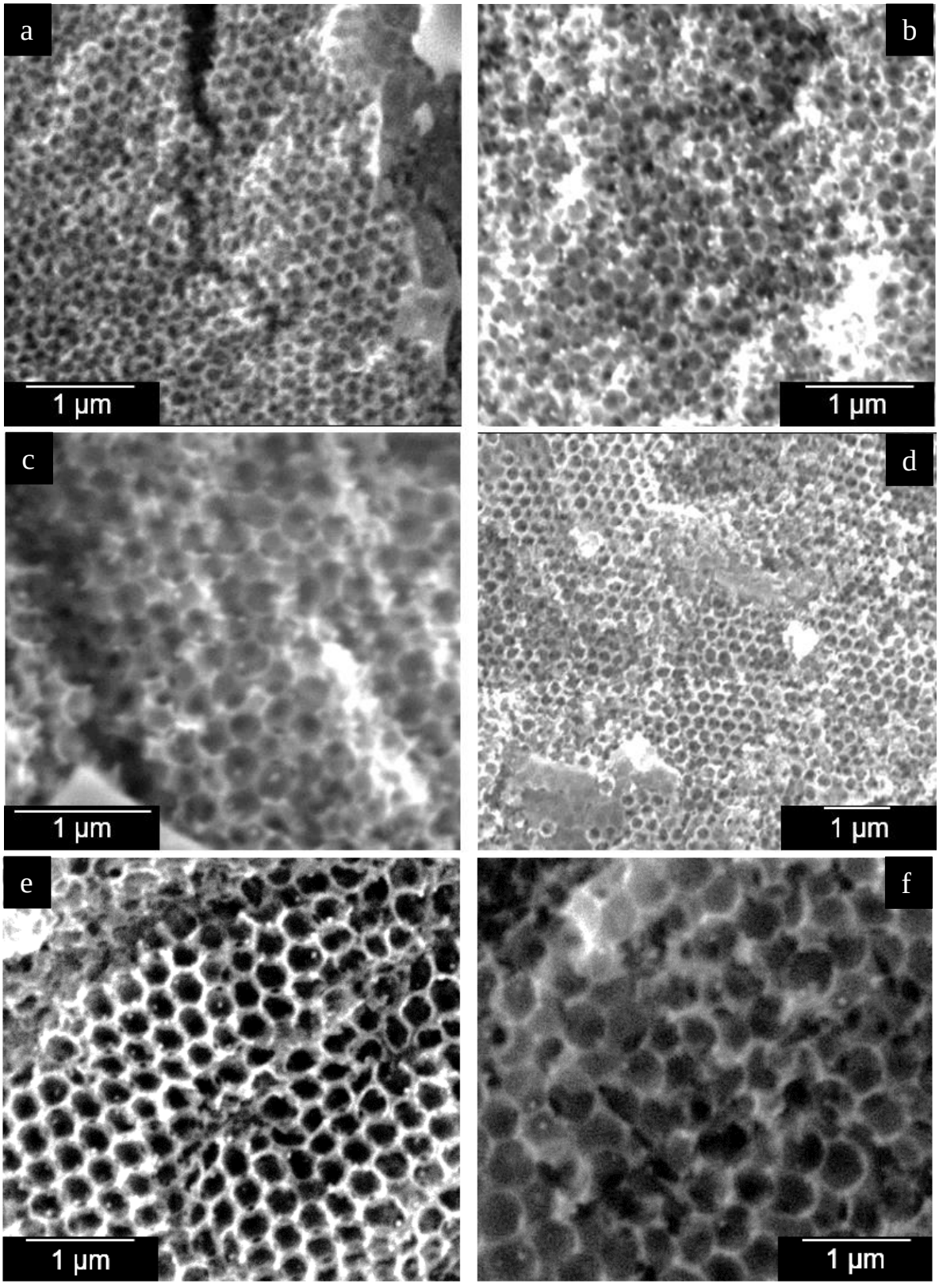

Fig. 3-16. LV-SEM images of Au-NP@IOT samples with average nanovoid diameter (a) 150 nm (b) 200 nm (c) 215 nm (d) 250 nm (e) 270 nm (f) 290 nm.

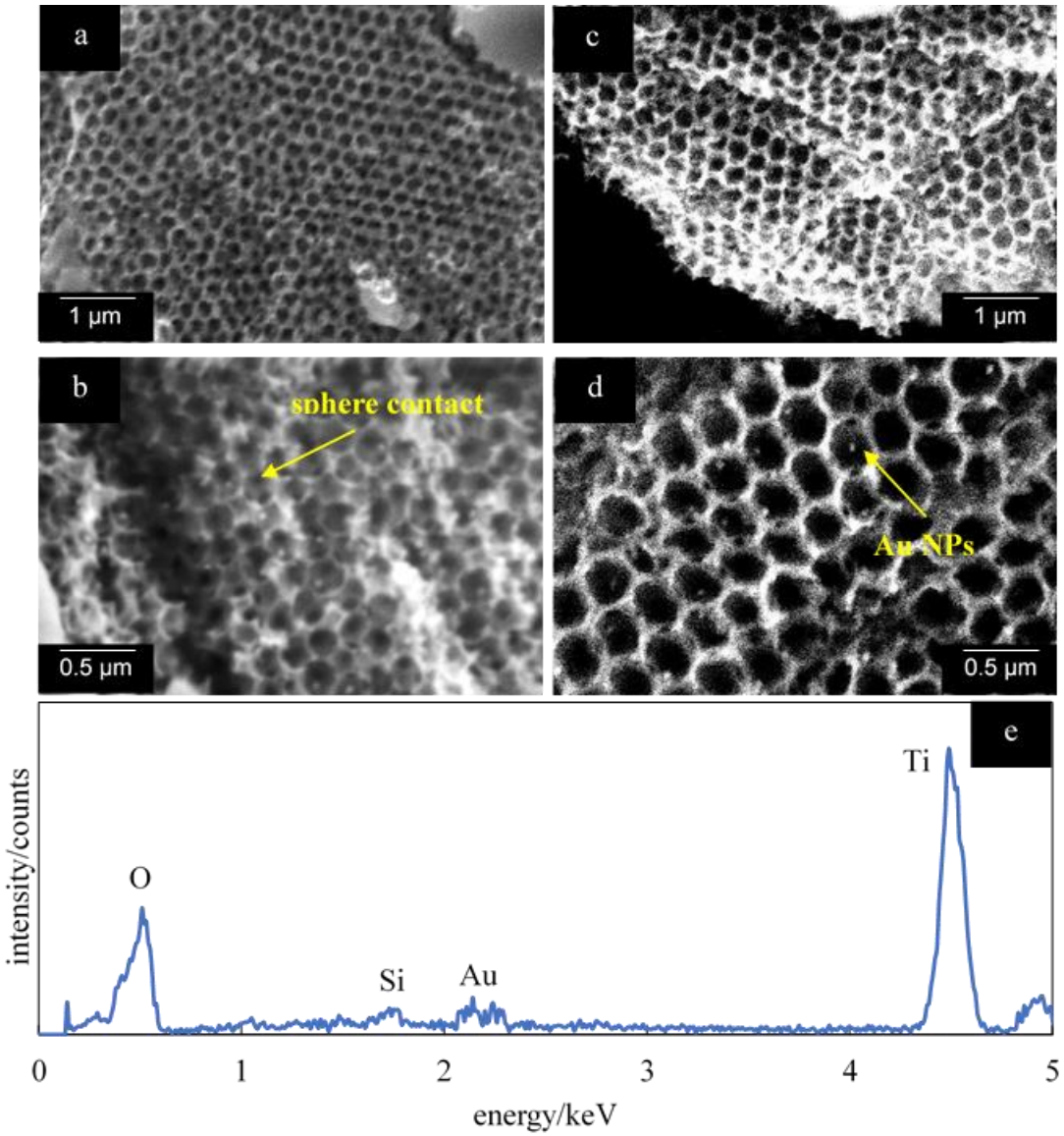

Fig. 3-17. LV-SEM images of Au-NP@IOT samples with average nanovoid diameter of (a-b) 215 nm and (c-d) 270 nm (e) EDX analysis of Au-NP@IOT with diameter of 270 nm.

In order to further confirm on the SiO_2 etching efficiency, the Au-NP@IOT with 270 nm nanovoid has been 'cut' and observed under LV-SEM. It could be evident that there was no clear trace of SiO_2 presence and only Au NPs incorporated inside the nanovoid could be seen in **Fig. 3-18 (a)**. Apart from that, EDX analysis on crushed sample has been carried out to observe the presence of Si after etching process (**Fig. 3-18 (b)**). The similar analysis as in **Fig. 3-17 (e)** was observed indicating the efficiency of the template etching has been the same either in the top layer, middle or the lowest layer as crushing could totally destroy the periodic structure, hence the overall SiO_2 presence could be detected.

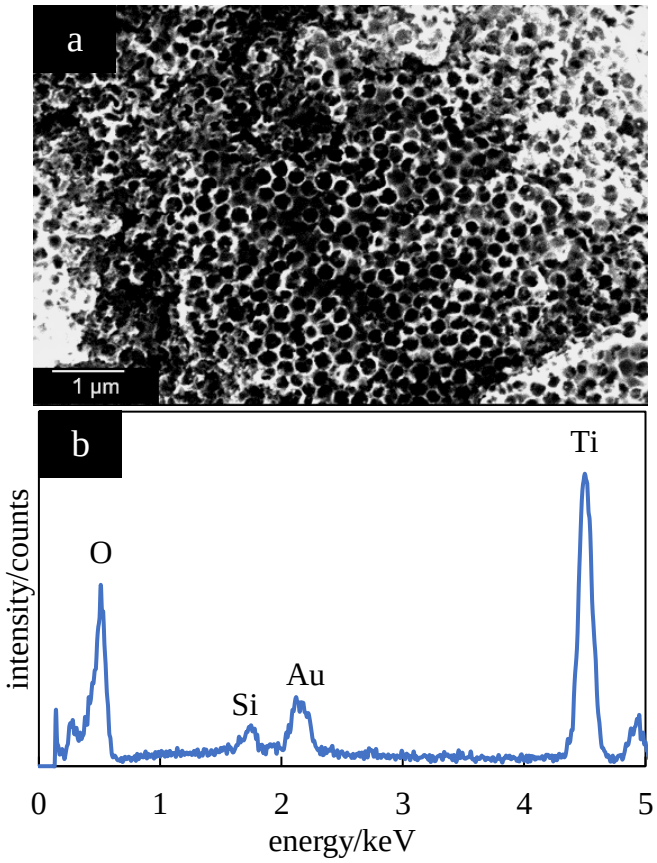

Fig. 3-18. (a) LV-SEM images of 'cut' Au-NP@IOT samples with average nanovoid diameter of 270 nm (b) EDX analysis of crushed Au-NP@IOT.

The estimated thickness of the TiO_2 backbone network formation was about 30-40 nm after 2 cycles of infiltration process. It has been noted that the thickness of the formed TiO_2 increases with the number of infiltration process. **Fig. 3-19 (a)** shows a fragment of Au-NP@IOT observed under electron microscopy revealing the presence of Au NPs in the voids after the template removal. Moreover, the anatase form of TiO_2 has been confirmed as lattice distance of 0.32 nm has been observed corresponding to {101} plane, as shown in **Fig. 3-19 (b)**.

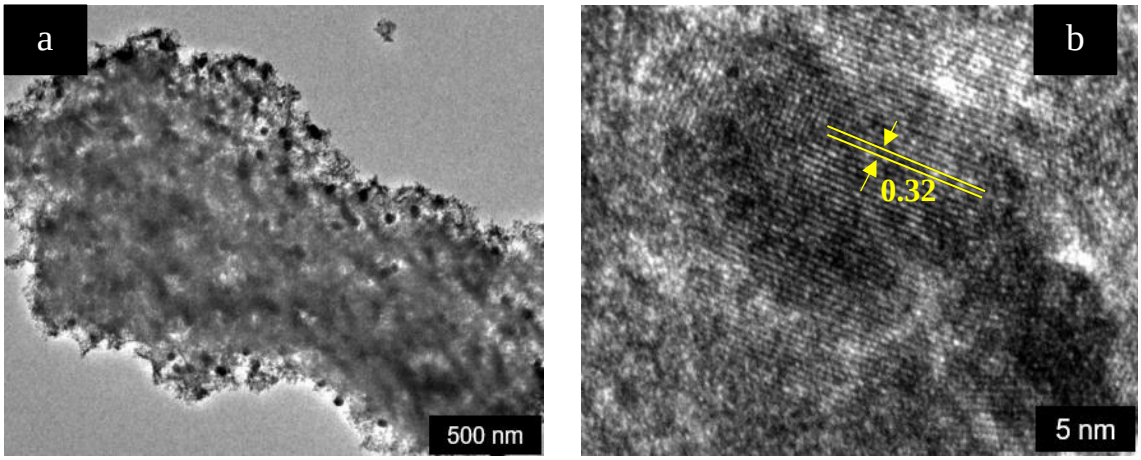

Fig. 3-19. TEM image of (a) Au-NP@IOT sample (b) lattice fringes of TiO_2.

It has been estimated that about ca. 5 – 6 wt% of Au NPs has been incorporated to form Au-NP@IOT samples. Hence, to confirm the content of the noble metal NPs, FAAS measurement has been carried out and the results have been reported in **Table 3-3**. The amount of incorporated Au NP into the IOT with void sizes of 200 nm, 215 nm, 270 nm and 290 nm has been detected to be ca. 5 wt%. Au-NP@IOT sample with nanovoid of 270 nm has been measured before and after 4-hours photoirradiation. The results showed ca. 0.3 wt% of difference which could be assumed as appreciable measurement error and most importantly appreciable of Au NPs leaching has not been detected (no decolourization observed after photoirradiation). The results further prove the amount of incorporated Au NP in Au-NP@IOT has been similar, hence the photoabsorbing ability among the samples are similar as indicated in DRS spectra of the samples and the photoabsorption efficiency could be compared only on considering the slow photons effect (triply wavelength matching).

Table 3-3. Au NP content (wt%) Au-NP@ IOTs using FAAS.

Au NP average diameter	IOT nanovoid	Au NP content (wt%)
44	200	5.1
44	215 (before photoirradiation)	4.8
30	240	5.2
30	290	4.8
30	270 (before photoirradiation)	5.1
30	270 (after photoirradiation)	4.8

The nanovoid distribution is important to predict the photonic effect, [Jovic 2016], and thus it has been estimated from SEM images of each sample, and obtained data are presented in Fig. 3-20. It has been found that with an increase in nanovoid size, the distribution becomes wider.

3-2 Optical study of Au-NP@IOT photocatalysts

3-2-1 Photoabsorption spectra of Au-NP@IOT

It should be noted that since Au-NP@IOT has been prepared in powdered form, hence the photonic shoulder (downward peak) could not be clearly observed in DRS spectrum (**Fig. 3-21**), due to the random scattering of incident light as IOT photonic crystals strongly sensitive to angle of light irradiation [Wu 2014 / Kim 2017] resulting in cumulative broad visible light absorption starting from 400 nm till ca. 700-800 nm. The similar observation has been reported by Wang et al. attributing the significant light harvesting due the presence of Au NPs in voids with visible absorption, resulting in overlapped PBG with LSPR [Wang 2016]. In addition, the proportion of crystal planes directed appropriately, i.e., at the Bragg angle, is too small to be detected in photoabsorption spectra, measured in the diffuse reflection mode. It should be noted that a shoulder-like flat part at ca. 450 nm that has been observed in the Au-NP@IOT spectra might be attributed to photoabsorption from/to the bandgap or surface states of titania [Waterhouse 2013]. As described in **Table 3-2**, Au NPs with two different sizes were employed in the seven prepared samples, and Au-NP@IOT with incorporated Au NPs of size

44 nm shows higher photoabsorption than those for samples with smaller (30 nm) size. The similar trend has been observed for both types of samples, i.e., the larger the nanovoid was, the stronger was photoabsorption (except Au-NP@IOT with nanovoid of 270 nm).

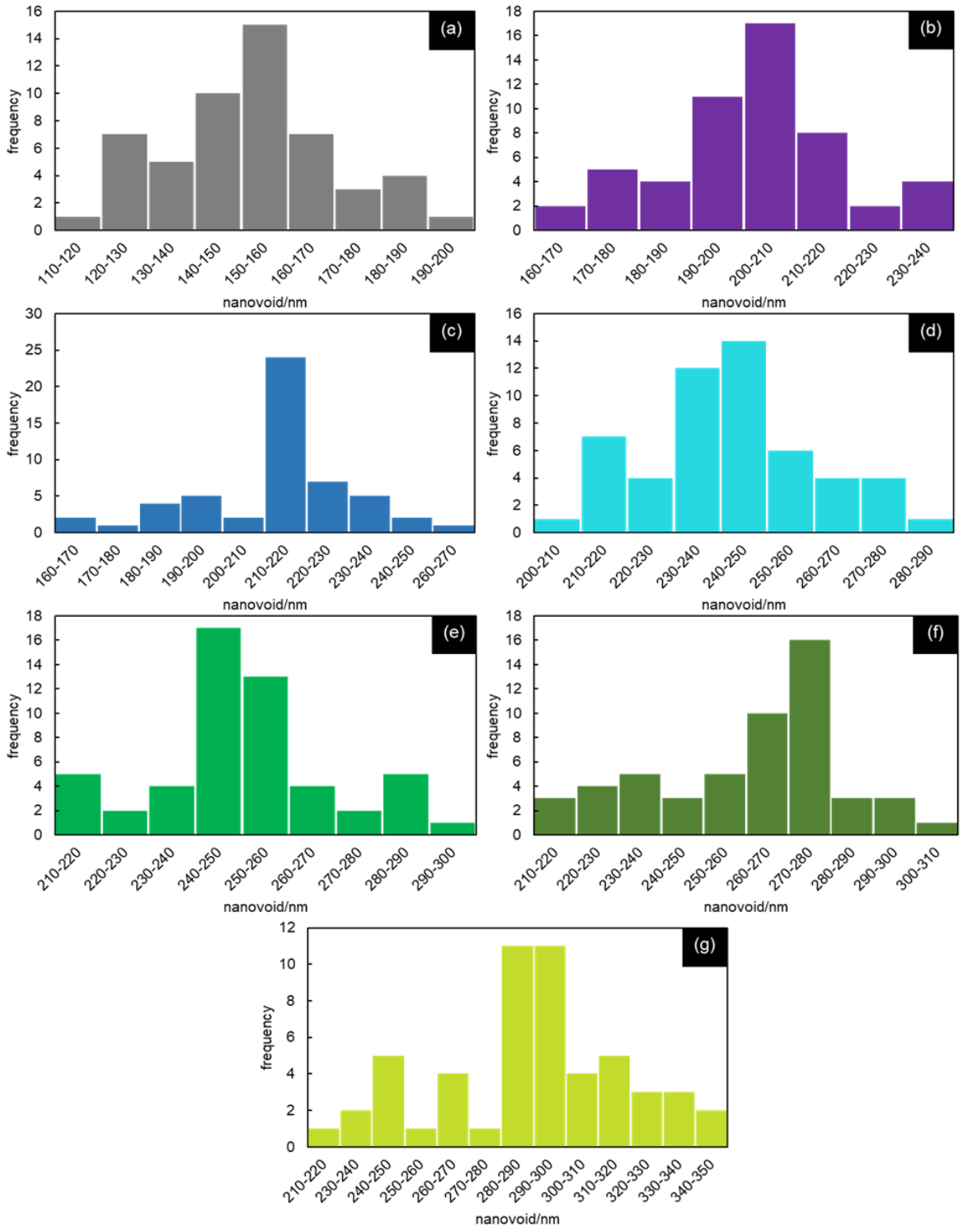

Fig. 3-20. Void-size distribution in Au-NP@IOT samples.

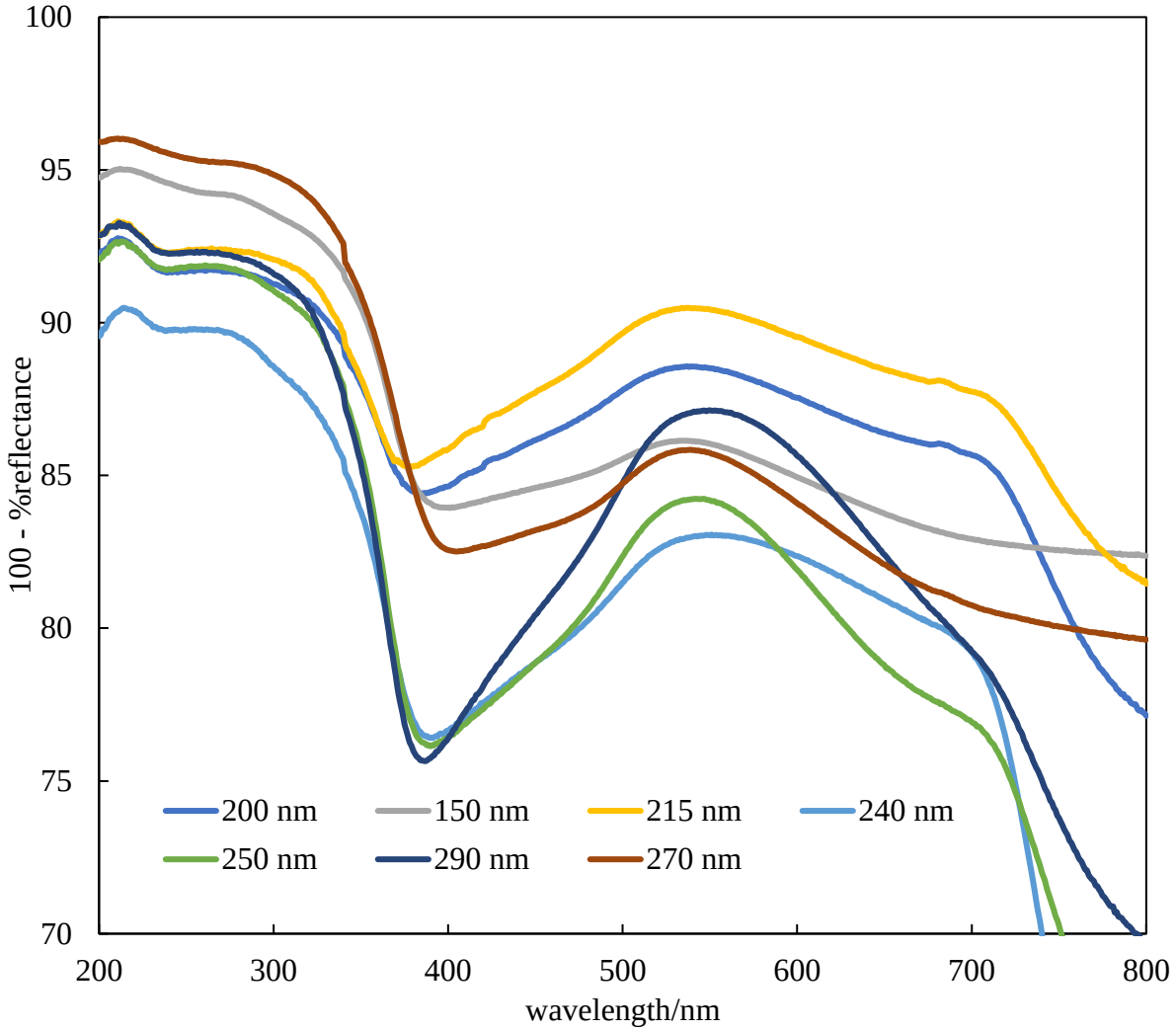

Fig. 3-21. DRS spectra of Au-NP@IOT samples.

In order to study the variance in photoabsorption in each stage prior obtaining the final product, Au-NP@IOT, DRS spectra has been obtained for Au@SiO_2 opal, TiO_2 infiltrated Au@SiO_2 (Au@SiO_2/TiO_2) and Au-NP@IOT with 270 nm nanovoid size (after SiO_2 template removal) samples. As could be observed in **Fig. 3-22**, Au@SiO_2 opal gave very broad photoabsorption spectra resulting from both Bragg diffraction peaks resulting from arrangement of face-centered cubic and refractive index contrast of SiO_2 and void (air) at ca. 400 nm and LSPR absorption at ca. 528 nm. The maximum peak owning to Au NP photoabsorption could be observed ca. 528 nm, which was as similar to the bare Au NPs' optical absorption. There was no obvious shift has been observed on the LSPR absorption wavelength although the surrounding environment of Au NPs has been coated with SiO_2. This

observation could be postulated by the non-interacting characteristics owned by Au NPs in this opal sample as in agreement by previous studies [Garcia-Santamaria 2002 / Ung 2001].

Once TiO_2 has been infiltrated on the opal, downward peak attributing to TiO_2 could be observed at ca. 360 nm till 380 nm along with a wide photoabsoprtion at visible region. Shoulder-like flat part at ca. 450 nm and wider visible range photoabsorption have been observed in the Au-NP@IOT spectra as discussed in the previous section. Surprisingly, the LSPR maximum absorption from Au NP have been shifted ca. 5 nm once the infiltration of TiO_2 ($Au@SiO_2/TiO_2$) and the removal of SiO_2 template (Au-NP@IOT). The red-shift of plasmon effect could be explained by the increased contrast of the high dielectric medium (TiO_2) and void (air) which attributed to stronger scattering within the structure which could directly affect on the contactless Au NPs in the voids after the SiO_2 removal.

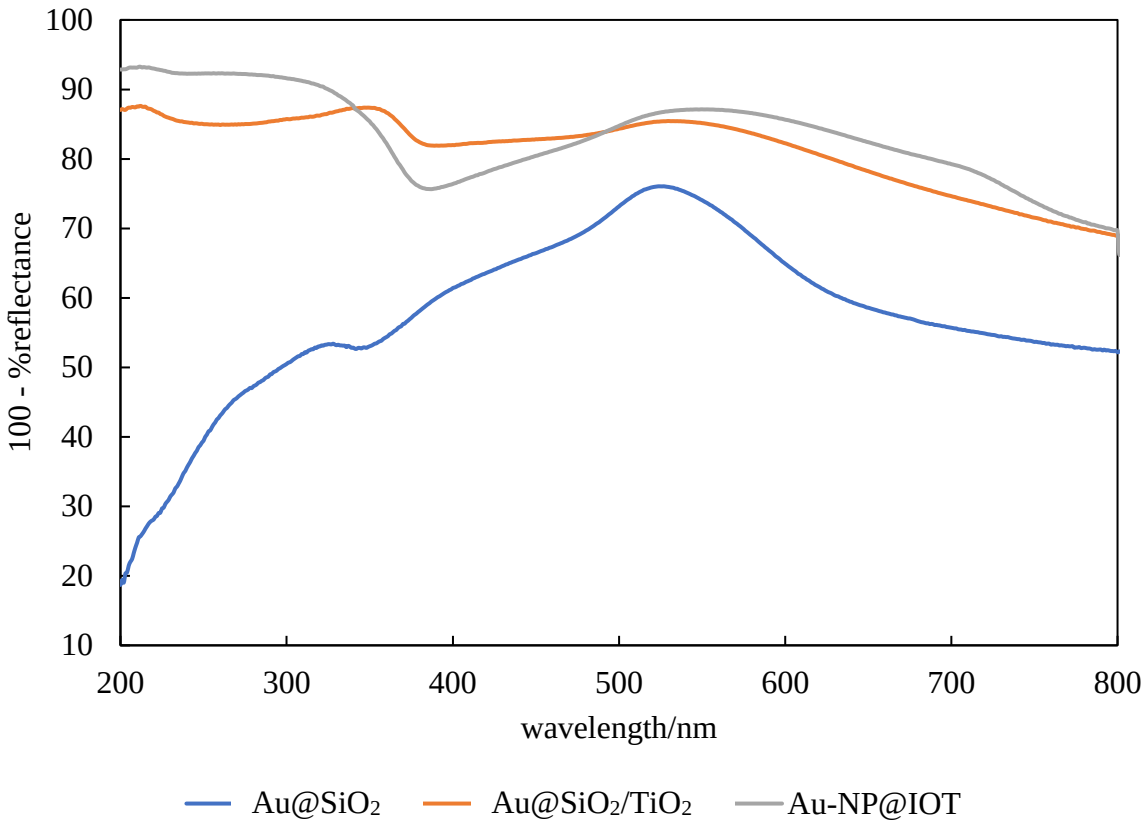

Fig. 3-22. DRS spectra of $Au@SiO_2$, $Au@SiO_2/TiO_2$ and Au-NP@IOT (270 nm nanovoid size) samples.

3-2-2 XRD analysis of Au-NP@IOT

Anatase presence has been proven by XRD analysis in all Au-NP@IOT samples, as shown in **Fig. 3-23**. Almost all the samples have the similar TiO_2 content according to the main (101) anatase diffraction peak intensity. As expected, peaks attributing to rutile polymorph have not been observed in all Au-NP@IOT samples as low calcination temperature (500 °C) has been applied for the crystallization. It has been already been reported that higher calcination temperature than 500 °C results in co-existence of both anatase and rutile phases, whereas calcination of TiO_2 PCs at 1000 °C could completely change the crystallinity to rutile polymorph [Li 2010]. The presence of Au NPs all samples have been proven with the diffraction peaks at 2θ of 38.18°, 44.38°,64.58° and 77.3° for (111), (200), (220) and (311) planes respectively, (JICST 8703). Noticeably, the incorporation of Au NP has not altered the crystal properties of TiO_2.

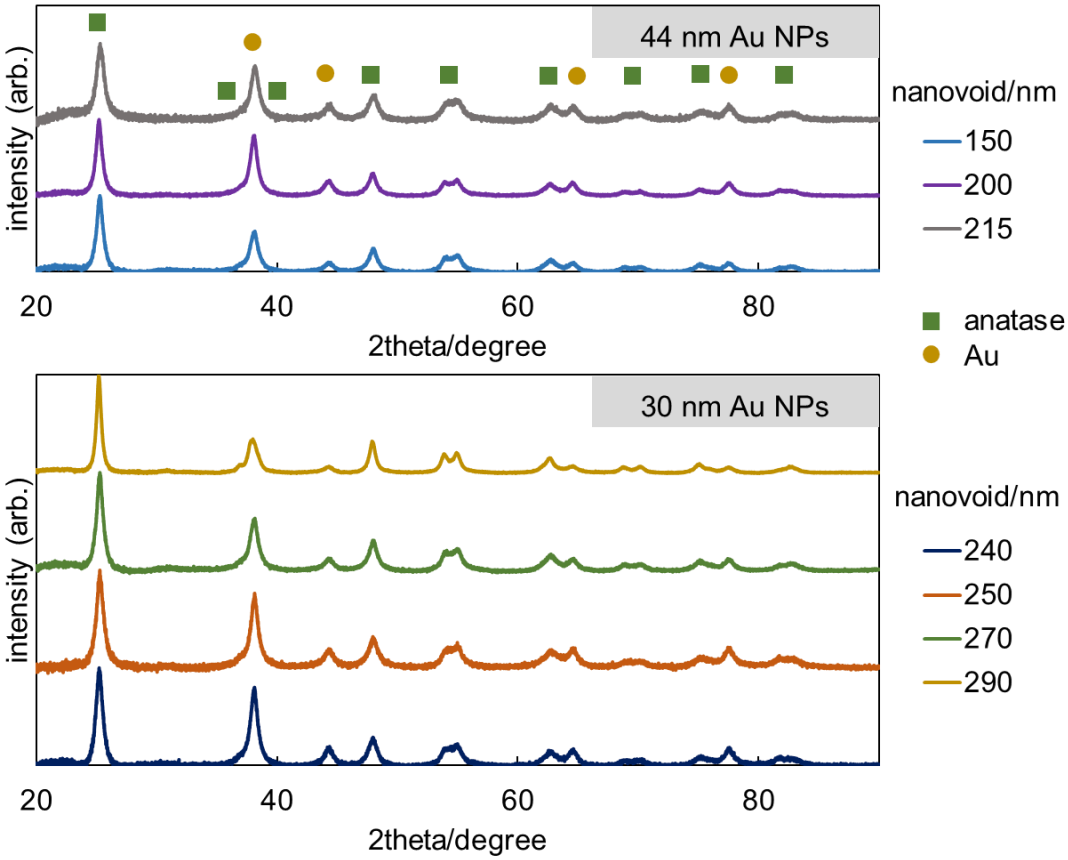

Fig. 3-23. XRD spectra of Au-NP@IOT samples with Au NPs of average diameter of 44 nm and 30 nm.

3-3 PBG calculations of Au-NP@IOT photocatalysts

As described in **Chapter 1,** PBG differs strongly by angle of irradiation, nanovoid diameter and effective refractive index. **Table 3-4** shows the PBG positions calculated for each 10º by assuming the lower dielectric medium such as in air and water (higher dielectric medium is TiO_2 with the average nanovoid diameter measured by LV-SEM. However, considering the nanovoid distribution (**Fig. 3-20)**, the PBG peak positions have been plotted as a Gaussian distribution (**Fig. 3-24)**. Since Au-NP@IOTs have been prepared in powder form, specific angle of irradiation could not be specified, hence 45º has been assumed to be implied in the calculation. In order to obtain the angle dependence, work along this line is now in progress, as described in **Chapter 6-2.** Effective refractive index involving the high (TiO_2) and low (water) dielectric medium refractive indexes corresponds to n=2.48 (taking into consideration of an anatase form, as proven via XRD analysis; **Fig. 3-23**) [Curti 2017] and n=1.33 respectively have been used in the PBG peaks calculation. To the best of our knowledge, this has been the first report to employ water (n=133) for PBG peak position wavelengths estimation, as previous reports involving the application of photonic crystals in photocatalysis have only used air (n=1.00) as the lower dielectric medium. Since Au-NP@IOT photocatalysts have been immersed in acetic acid aqueous solution for the photocatalytic activity tests, the voids would have been filled with water rather than air. Hence, it would be more appropriate to estimate the PBG peak position in water for PBG-activity correlations (**Chapter 4**). The Gaussian plots estimate the expected PBG-peak wavelengths that in the range of from 350–750 nm, depending on the nanovoid distribution for respective samples, covering the wavelength of photoabsorption by Au-NPs (LSPR effect) and titania (electronic band gap) in Au-NP@IOT. Thus, the estimated PBG peak positions have a distribution of relatively wide wavelength ranges due to both actual incident-beam angle and void-size distributions. It has been reported that photonic effect, i.e., slow photons effect, which leads to the photoabsorption amplification, has appeared in both blue-edge (shorter wavelength) [Deparis 2015] and red-edge (longer wavelengths) [Zhang 2014]. In this study, only blue-edge wavelength has been considered since there is no adequate Au-NPs@IOT samples having a red-edge PBG wavelength range fitting LED with emissions of 530 nm and 450 nm used as irradiation sources. As described in **Chapter 2** (**section 2-5**), the blue-edge wavelengths have been estimated by employing 0-25 % from the PBG peak position wavelength range (as in **Fig. 3-24**) which has been presented in **Fig. 3-25**.

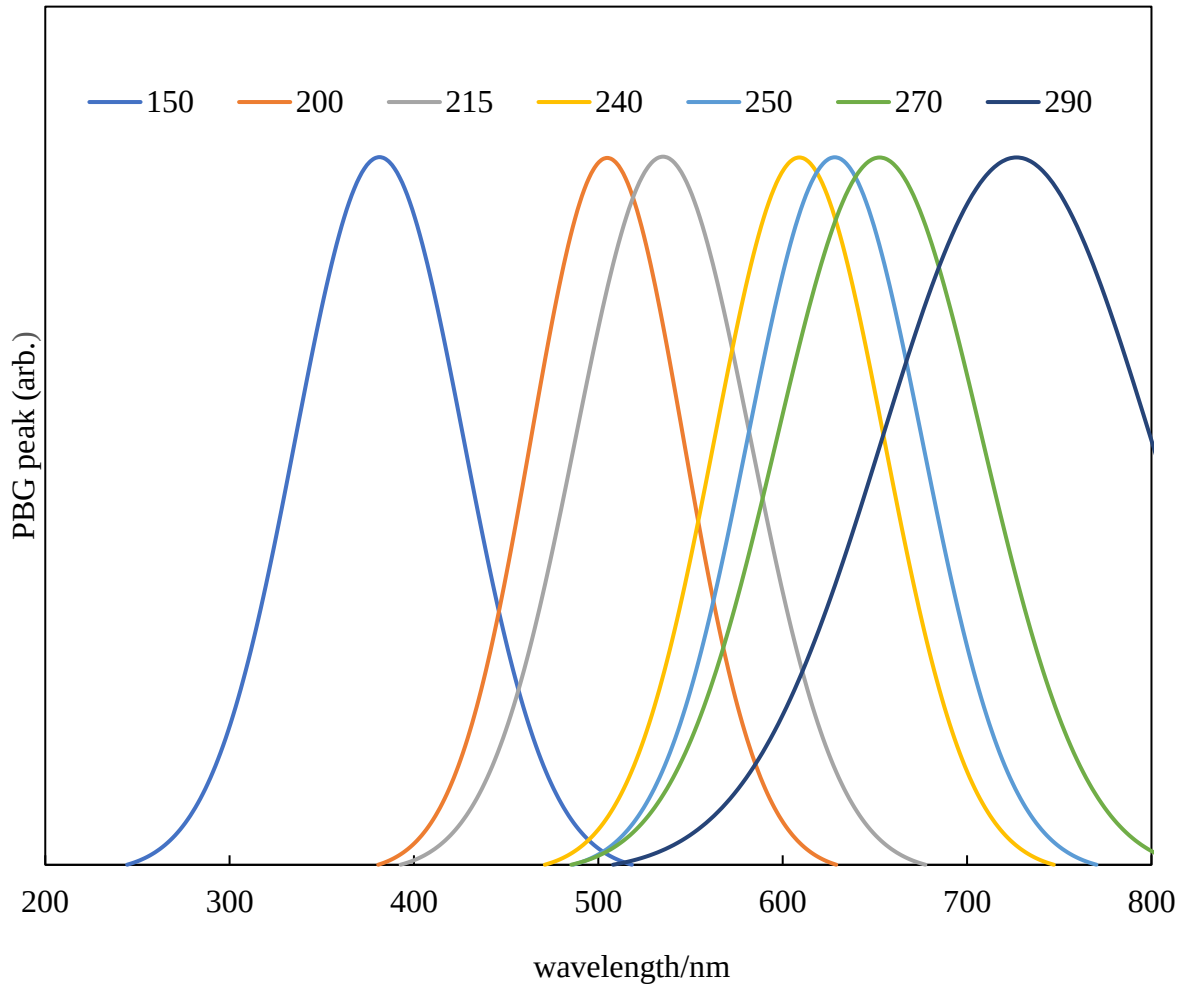

Fig. 3-24. PBG peak positions calculated for Au-NP@IOT samples with different distribution of nanovoid diameter.

Table 3-4. PBG value calculated for each sample with average nanovoid in air (a) water (b) medium for each 10º angle.

(a) average nanovoid diameter/nm	Θ										
	0	**10**	**20**	**30**	**40**	**45**	**50**	**60**	**70**	**80**	**90**
150	370.00	367.54	360.42	349.22	334.93	327.12	319.09	303.42	289.96	280.89	277.70
200	493.33	490.06	480.56	465.62	446.58	436.16	425.46	404.56	386.61	374.51	370.26
215	530.33	526.81	516.61	500.54	480.07	468.87	457.37	434.90	415.60	402.60	398.03
240	591.99	588.07	576.68	558.75	535.89	523.39	510.55	485.47	463.93	449.42	444.32
250	616.66	612.57	600.70	582.03	558.22	545.20	531.82	505.70	483.26	468.14	462.83
270	665.99	661.57	648.76	628.59	602.88	588.81	574.37	546.16	521.92	505.59	499.86
290	715.32	710.58	696.82	675.15	647.54	632.43	616.91	586.61	560.58	543.04	536.88

(b) average nanovoid diameter/nm	Θ										
	0	**10**	**20**	**30**	**40**	**45**	**50**	**60**	**70**	**80**	**90**
150	413.49	411.29	404.94	395.00	382.43	375.61	368.64	355.16	343.73	336.11	333.45
200	551.32	548.39	539.92	526.67	509.91	500.81	491.52	473.55	458.31	448.15	444.60
215	592.66	589.52	580.42	566.17	548.15	538.37	528.38	509.06	492.68	481.76	477.95
240	661.58	658.07	647.91	632.00	611.89	600.97	589.82	568.26	549.97	537.78	533.53
250	689.15	685.49	674.91	658.34	637.39	626.01	614.40	591.93	572.88	560.19	555.76
270	744.28	740.33	728.90	711.00	688.38	676.09	663.55	639.29	618.71	605.00	600.22
290	799.41	795.17	782.89	763.67	739.37	726.18	712.70	686.64	664.54	649.82	644.68

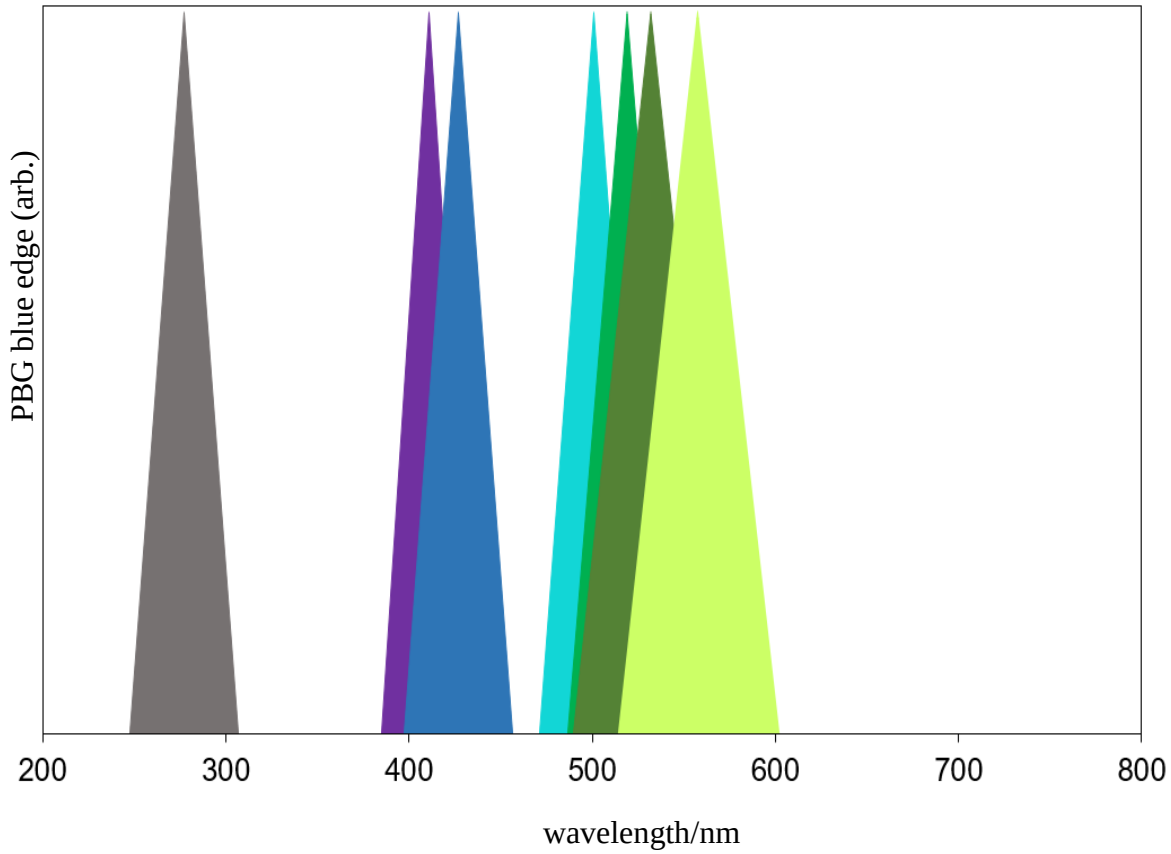

Fig. 3-25. Blue-edge of PBG peak wavelegths range for Au-NP@IOT samples with different distribution of nanovoid diameter.

3-4 Irregular multiarray structure of Au-NP@IOT-like

Morphology study on Au-NP@IOT sample which particles have been self-assembled after TiO_2 impregnation on $Au@SiO_2$ core-shell particles has also been carried out. It could be seen that the core-shell particles have been fully coated by TiO_2 as shown in **Fig. 3-26 (a)**. It is clear that much rougher and denser surface has been obtained for $Au@SiO_2/TiO_2$ multiarray structure (**Fig. 3-26 (b))** than that for Au-NP@IOT (**Fig. 3-13 (c)**) for which the template has been formed in prior of TiO_2 infiltration. Etching of SiO_2 led to the formation of irregular multiarray of Au-NP@IOT-like sample as shown in **Fig. 3-27**. Firstly, an ordered structure with hexagonal arrangement could not be seen, followed by the inconsistent formation of nanovoid. Secondly, the TiO_2 network formation has been broken in most of the parts with an

uneven thickness of the high dielectric medium. Consequently, the Au NPs have been randomly positioned on the surface of the TiO_2 backbone. The major reason for those occurrences might be the uncontrolled thickness of TiO_2 formed in bulk on the disordered $Au@SiO_2$ core-shell particles and thus, prevents the further penetration in the absence of void spaces between each particle. It should be pointed that such disordered multiarray structure of Au-NP@IOT would be definitely unfavorable to evident photonic effect. Hence, self-assembly after impregnation on $Au@SiO_2$ core-shell particles have been discovered to be not efficient enough to form a high-quality of TiO_2 PC.

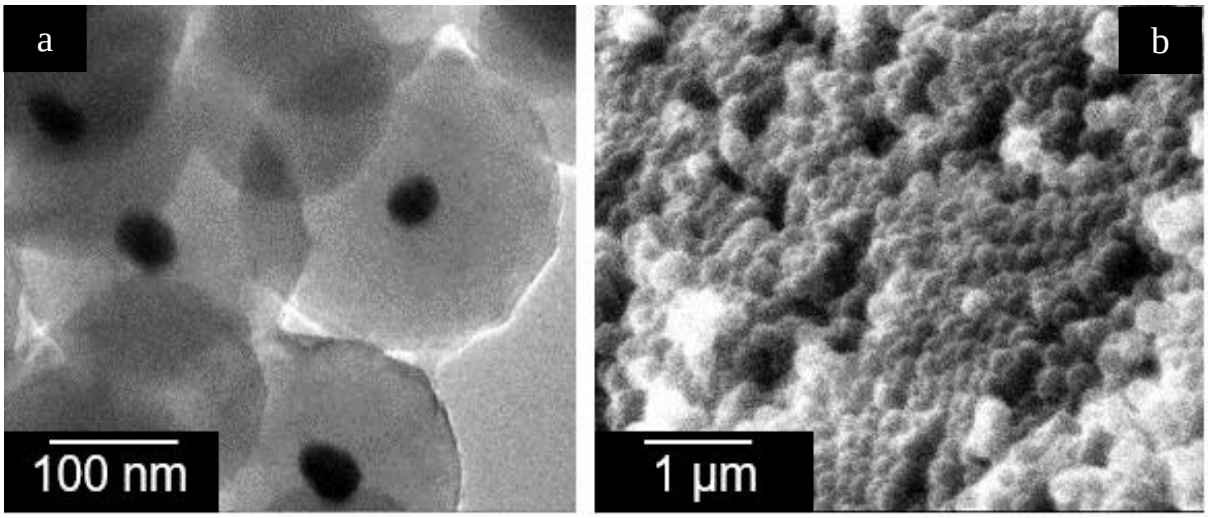

Fig. 3-26. LV-SEM images of (a) $Au@SiO_2/TiO_2$ (b) multiarray strcuture of $Au@SiO_2/TiO_2$.

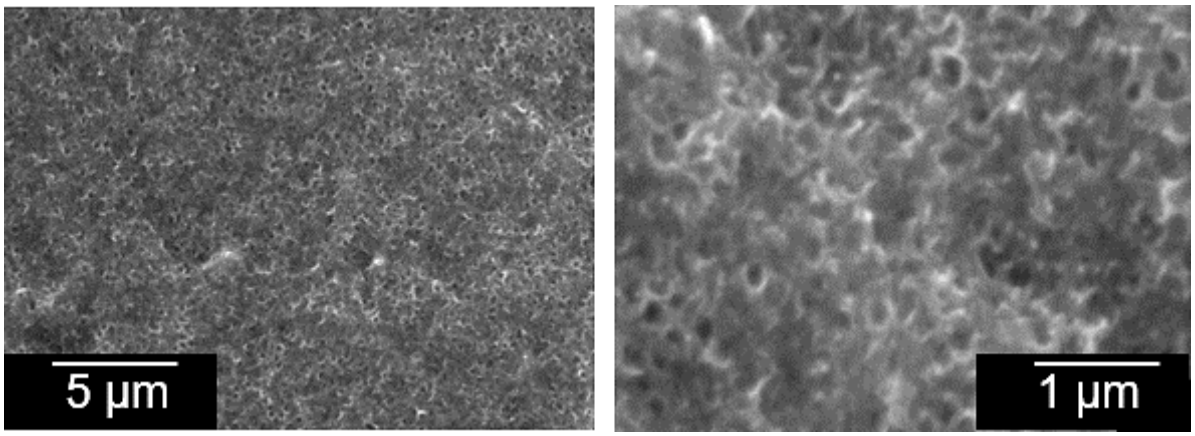

Fig. 3-27. Irregular Au-NP@IOT -like multiarray structure.

3-5 References

Bastus, N. G.; Comenge, J.; Puntes, V. Kinetically controlled seeded growth synthesis of citrate-stabilized gold nanoparticles of up to 200 nm: Size focusing versus Ostwald ripening. *Langmuir* **27**, 11098–11105 (2011).

Chen, H.; Kou, X.; Yang, Z.; Ni, W.; Wang, J. Size-dependent refractive index sensitivity of gold nanoparticles. *Langmuir* **24,** 5233-5237 (2008).

Chen, X.; Li, Z.; Ye, J.; Zou, Z. Forced impregnation approach to fabrication of large-area, three-dimensionally ordered macroporous metal oxides. *Chem. Mater.* **22,** 3583-3585 (2010).

Chiang, C.C.; Tuyen, L.D.; Ren, C.R.; Chau, L.K.;Wu, C.Y.; Huang, P.J.; Hsu, C.C. Fabrication of titania inverse opals by multi-cycle dip-infiltration for optical sensing. *Photonics Nanostruct.* **19,** 48–54 (2016).

Curti, M.; Mendive, C. B.; Grela, M. A.; Bahnemann, D. W. Stopband tuning of TiO_2 inverse opals for slow photon absorption *Mater. Res. Bull.* **91,** 155–165 (2017).

Deparis, O.; Moucheta, S. R.; Su, B-L. Light harvesting in photonic crystals revisited: why do slow photons at the blue edge enhance absorption? *Phys. Chem. Chem. Phys.*, **17**, 30525–30532 (2015).

Dong, J.; Carpinone, P. L.; Pyrgiotakis, G.; Demokritou, P.; Moudgil, B. M. Synthesis of precision gold nanoparticles using Turkevich method. *KONA Powder and Particle Journal*, **37**, 224–232 (2020).

Garcia-Santamaria, F.; Salgueirino-Maceira, V.; Lopez, C.; Liz-Marzan, L. M. Synthetic opals based on silica-coated gold nanoparticles. *Langmuir*,**18**, 4519–4522 (2002).

Haiss, W.; Thanh, N. T. K.; Aveyard, J.; Fernig, D. G. Determination of size and concentration of gold nanoparticles from UV-Vis spectra. *Anal. Chem.* **79**, 4215-4221 (2007).

Hatton, B.; Mishchenko, L.; Davis, S.; Sandhage, K. H.; Aizenberg. J. Assembly of large-area, highly ordered, crack-free inverse opal films. *PNAS* **107,** 10354–10359 (2010).

Jovic, V.; Idriss, H.; Waterhouse, G. I. N. Slow photon amplification of gas-phase ethanol photo-oxidation in titania inverse opal photonic crystals. *Chem. Phys.* **479,** 109–121 (2016).

Kim, W. T.; and Choi, W. Y. Fabrication of TiO_2 photonic crystal by anodic oxidation and their optical sensing properties. *Sens. Actuator A: Phys.* **260,** 178–184 (2017).

Li, Y.; Piret, F.; Léonard, T.; Su, B-L. Rutile TiO_2 inverse opal with photonic bandgap in the UV–visible range. *Journal of Colloid and Interface Science* **348** (2010) 43–48

Li, X. H.; Wu, Y.; Shen, Y.H.; Sun, Y.; Yang, Y.; Xie, A. A novel bifunctional Ni-doped TiO_2 inverse opal with enhanced SERS performance and excellent photocatalytic activity. *Appl. Surf. Sci.* **427,** 739–744 (2018).

Liz-Marzan, L. M. Tailoring surface plasmons through the morphology and assembly of metal nanoparticles. *Langmuir* **22,** 32-41 (2006).

Liz-Marzan, L. M.; Giersig, M.; Mulvaney, P. Synthesis of nanosized gold-silica core-shell particles. *Langmuir* **12,** 4329-4335 (1996).

Miguez, H.; Meseguer, F.; López, C.; Blanco, A.; Moya, J. S.; Requena, J.; Mifsud, A.; Fornés, V. Control of the photonic crystal properties of fcc-packed submicrometer SiO_2 spheres by sintering. *Adv. Mater*. **10,** 480-483 (1998).

Montano-Priede, J. L.; Coelho, J. P.; Guerrero-Martinez, A.; Pena-Rodriguez, O.; Pal, U. Fabrication of monodispersed $Au@SiO_2$ nanoparticles with highly stable silica layers by ultrasound-assisted stober method. *J. Phys. Chem. C* **121,** 9543-9551 (2017).

Nassor, E. C. O.; Ávila, L. R.; Pereira, P. F. S.; Ciuffi, K. J.; Calefi, P. S.; Nassar, E. J. Influence of the hydrolysis and condensation time on the preparation of hybrid materials. *Mat. Res.* **14,** 1-6 (2011).

Turkevich, J.; Stevenson, P. C.; Hillier, J. A study of the nucleation and growth processes in the synthesis of colloidal gold. *Discuss. Faraday Soc.* **11,** 55–75 (1951).

Ung, T.; Liz-Marzán, L. M.; Mulvaney, P. Optical properties of thin films of $Au@SiO_2$ particles. *J. Phys. Chem. B*, **105**, 3441 (2001).

Wang, X.; Li, J.; Gao, X.; Shen, Y.; Xie, A. Ordered CdSe-sensitized TiO_2 inverse opal film as multifunctional surface enhanced Raman scattering substrate. *Appl. Surf. Sci.* **463,** 357–362 (2019).

Wang. Y.; Xiong, D-B.; Zhang, W.; Su, H.; Liu, Q.; Gu, J.; Zhu, S.; Zhang, D. Surface plasmon resonance of gold nanocrystals coupled with slow-photon-effect of biomorphic TiO_2 photonic crystals for enhanced photocatalysis under visible-light. *Catalysis Today* **274** (2016) 15–21

Waterhouse, G. I. N.; Wahab, A. K.; Al-Oufi, M.; Jovic, V.; Anjum, D. H.; Sun-Waterhouse, D.; Llorca, J.; Idriss, H. Hydrogen production by tuning the photonic band gap with the electronic band gap of TiO_2. *Sci. Rep.*, **3**, 2849–2849-5 (2013).

Wu, M.; Liu, J.; Jin, J.; Wang, C.; Huang, S.Z.; Deng, Z.; Li, Y.; Su, B. L. Probing significant light absorption enhancement of titania inverse opal films for highly exalted photocatalytic degradation of dye pollutants. *Appl. Catal. B: Environ.* **150– 151,** 411– 420 (2014).

Zhang, X.; Liu, Y.; Lee, S.T.; Yang, S.H.; Kang, Z.H. Coupling surface plasmon resonance of gold nanoparticles with slow-photon-effect of TiO_2 photonic crystals for synergistically enhanced photoelectrochemical water splitting. *Energy Environ. Sci.* **7**, 1409–1419 (2014).

Chapter 4

Photocatalytic activity and elucidation on the photoabsorption-efficiency enhancement of Au-NP@IOT samples

4-1 Introduction

The enhancement of photocatalytic activity for IO structures coupling with plasmon effects has already been reported [Wang, 2016], however polychromatic irradiation ($\lambda > 420$ nm) was used in all studies, which could not provide the strong evidence on the enhancement arising from plasmon effects as the slow photons also could overlap with electronic band gap of TiO_2 at the region of 420 nm to 450 nm. To the best of our knowledge, this is the first report clarifying the exact evidence on the overlapping of photonic and LSPR effects. Accordingly, photocatalytic activity of obtained Au-NP@IOT (**Section 2-8**) have been investigated under monochromatic irradiation with two LEDs of emission at 530 nm and 450 nm.

Additionally, it should be pointed out that almost all reported studies on photocatalytic activity were performed under continuous stirring, which might be not precise in determining the photonic effect, specifically for powdered IO samples due to the random light scattering correlating to the angle dependence apart from destruction of the samples. In this regard, present study has been performed first under non-stirring condition. However, it is known that such conditions might result in diffusion-limited activity, and thus experiments under stirring have also been performed as discussed in this chapter.

4-2 530-nm LED emission

4-2-1 Non-stirring system

Fig. 4-1 shows the time-course acetic acid decomposition on all seven Au-NP@IOT samples irradiated under monochromatic green LED (λ = 530 nm) for four hours. Photoabsorption by Au NP around ca. 530 nm due to LSPR effect has been well clarified and proven in **Section 3-1** and **3-2**. Hence, it is expected that all Au-NP@IOT photocatalysts with different void spaces might drive the photocomposition of acetic acid as the monochromatic irradiation wavelength overlaps precisely with LSPR absorption. However, an enhanced photocatalytic activity has been observed only for one particular Au-NP@IOT sample with average nanovoid of 270 nm, whereas other samples have shown appreciable considering the activity in dark but much lower activity.

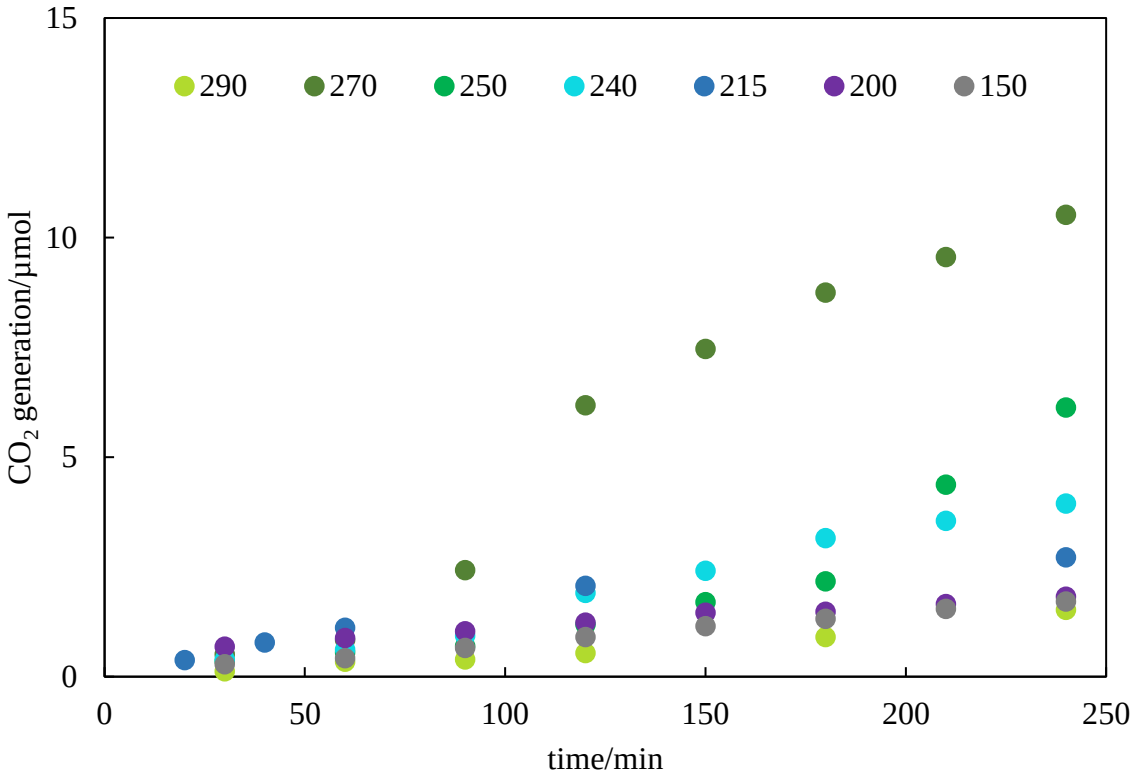

Fig. 4-1. Time-course curve of photocatalytic activity for Au-NP@IOT samples irradiated under monochromatic light irradiation of 530 nm for 4 hours.

Looking back at PBG edge-wavelength range (**Fig. 3-25)**, Au-NP@IOT with average nanovoid of 270 nm has the estimated PBG-edge wavelength close to the irradiation wavelength, (530 nm) and to LSPR of gold. Hence, it could be concluded that the only reason for the photocatalytic activity enhancement could be the precise matching between triply wavelength ranges i.e., slow photons, LSPR photoabsorption and monochromatic irradiation (as illustrated in **Fig. 4-2**), as the photocatalysts have been prepared in similar way except in the differences of nanovoid diameter. LSPR effect was not strong enough to drive the photodecomposition of acetic acid for samples with PBG blue-edge wavelength ranges located further away from the both monochromatic irradiation and LSPR effect, as evident by low amount of generated CO_2. In addition, negligible activity of IOT (without Au NP) with similar average nanovoid diameter (ca. 270 nm) to that in the most active Au-NP@IOT sample under 530 nm irradiation source has been proven as presented in **Fig. 4-2 (a)** and **Fig. 4-3**.

Enhancement of almost 5-fold has been observed for Au-NP@IOT in comparison to IOT without gold, which is another significant evidence directly indicated the photoabsorption enhancement is attributed to overlapping of photonic and LSPR effects with irradiation source. The inactivity of the 'empty' IOT could be explain by the inability of the high dielectric material, TiO_2, to absorb light at 530 nm due to the wide band-gap, and thus TiO_2 could only absorb light at the UV region and slight absorption at vis range till ca. 450 nm is also possible due to some disorders in its crystals structure. Recyclability photocatalytic test has been performed for the Au-NP@IOT sample with the highest activity for two cycles. The activity seems to reduce a little (ca. 0.8 µmol) in the second cycle as presented in **Fig. 4-4**. The irradiation angle on the powdered sample might be changed in the latter cycle as it is almost impossible to control the orientation of the Au-NP@IOT photonic crystal exactly as in the first cycle. Hence, the efficiency of the photocatalyst might vary a little in each time when the powdered structure is recycled. However, it should be noted that, the total CO_2 evolution has been still much higher in the second cycle than that by other Au-NP@IOT samples.

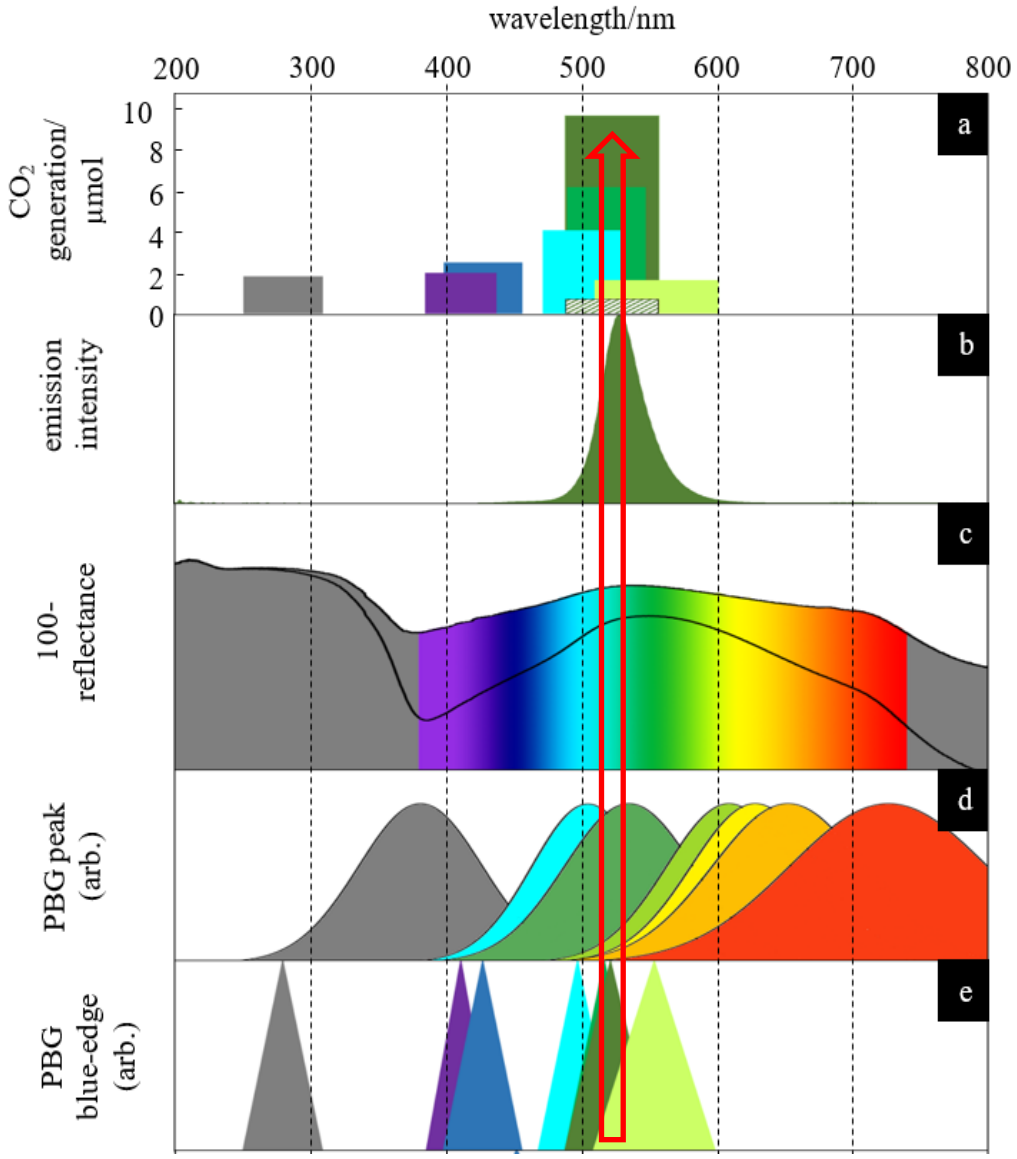

Fig. 4-2. Matching of photoabsorption properties with resultant photocatalytic activities for Au-NP@IOT samples with different nanovoid diameters; [a] CO_2 generation by Au-NP@IOT samples with average nanovoid of 150 nm (grey) 200 nm (purple) 215 nm (blue) 240 nm (sky blue) 250 nm (green) 270 nm (darker green) 290 nm (lime) bare IOT-270 (shaded) [b] 530 nm LED emission spectra [c] representative DRS spectra of Au-NP@IOT with Au NP of 44 nm (upper) and 30 nm (below) [d] PBG peak for Au-NP@IOT samples with nanovoid 150 nm (grey) 200 nm (light blue) 215 nm (green) 240 nm (light green) 250 nm (yellow) 270 nm (orange) 290 nm (red) [e] PBG blue-edge wavelengths for Au-NP@IOT (same colours as in [a]).

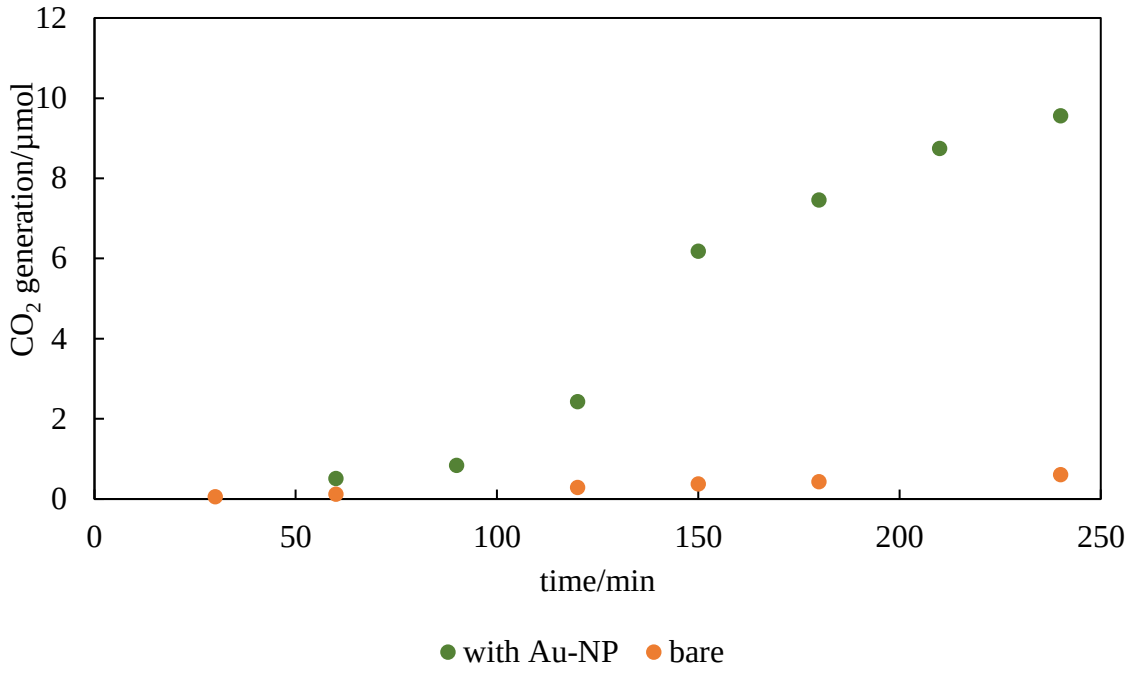

Fig. 4-3. Time-course acetic acid decomposition on Au-NP@IOT and IOT sample with 270 nm nanovoids irradiated under monochromatic light irradiation of 530 nm for 4 hours.

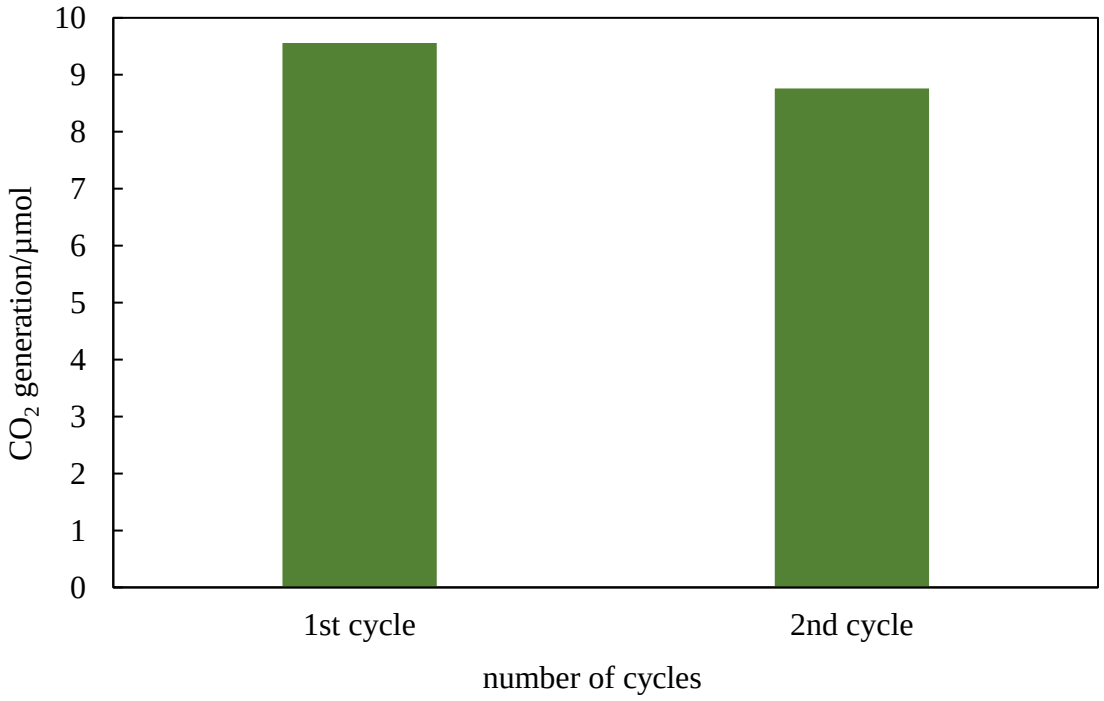

Fig. 4-4. Recyclability test of photocatalytic activity for Au-NP@ IOT with average nanovoid of 270 nm.

4-2-2 Stirring system

The enhancement of photocatalytic activity has been further studied in the stirring system to limit diffusion-control activity, as been observed by long induction time in **Fig. 4-1** and **4-3** (minimum 50 minutes of irradiation to get any CO_2 detected). Two main possible phenomena could be occurred when the powdered photonic crystals are stirred continuously under photoirradiation. Firstly, the destruction of the periodic structures could happen, which directly affect the multiscattering of the light (PBG and slow photons). Secondly, powdered samples in suspension would be randomly oriented due to the continuous change in the incident angle of irradiation as stirring proceeds. **Fig. 4-5** shows the photocatalytic activity of Au-NP@IOT samples with 150 nm, 270 nm, 290 nm nanovoid and bare IOT with 270 nm nanovoid. All the samples have been practically inactive under green LED emission except for Au-NP@IOT that also displayed the photoabsorption enhancement in non-stirring system, as discussed in **Section 4-2-1**. This result has confirmed directly that slow photons do exist and arise in that particular sample, as even under stirring the photocatalytic activity enhancement has been observed. This result is consistent with a study by Zhao et al. stating that slow photons could always exist in powdered samples [Zhao, 2018]. The bare IOT with 270 nm has shown the worst activity (practically inactive), proving that only the sample with photoabsoprtion ability at particular wavelengths (e.g., 530 nm due to LSPR of gold) might be active, and exhibits activity acceleration when this absorption is overlapped with slow photon effect.

The direct comparison between Au-NP@IOT with average diameter of 270 nm under stirring and non-stirring condition has been shown in **Fig. 4-6**. Indeed, almost two-fold loss of activity has been observed for the sample under stirring, which might be attributed to the loss of the periodic structure, as suggested by others [Wang 2016 / Dinh, 2014].

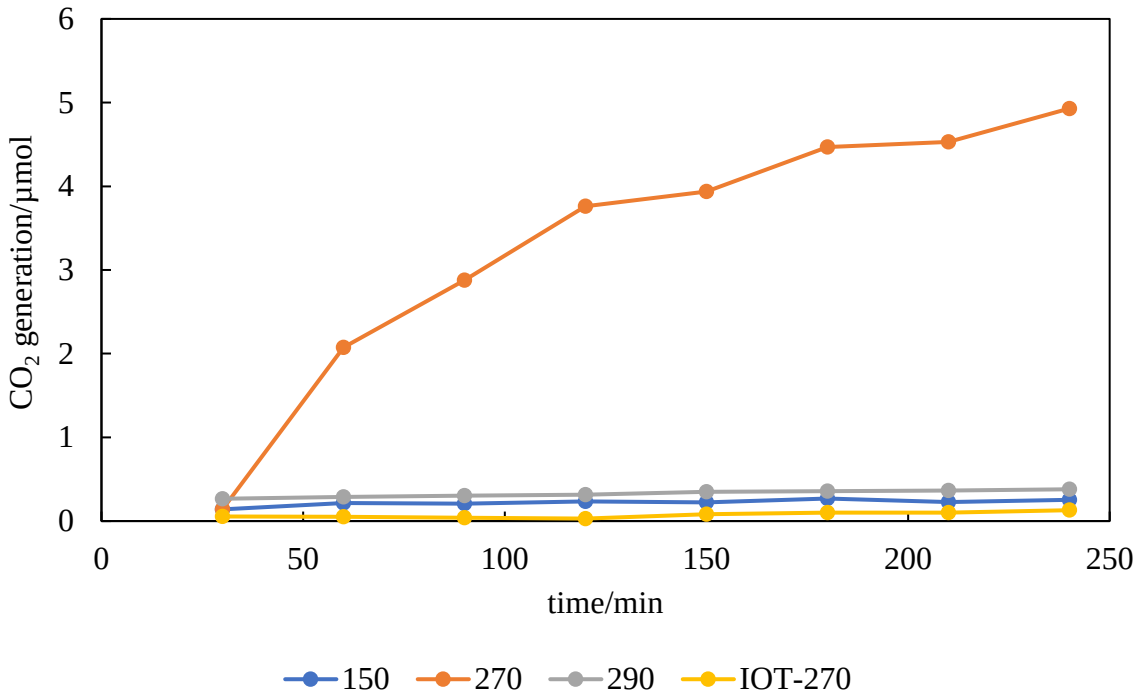

Fig. 4-5. Time-course acetic acid decomposition on Au-NP@IOT and IOT sample with 270 nm nanovoids irradiated under monochromatic light irradiation of 530 nm in stirring condition.

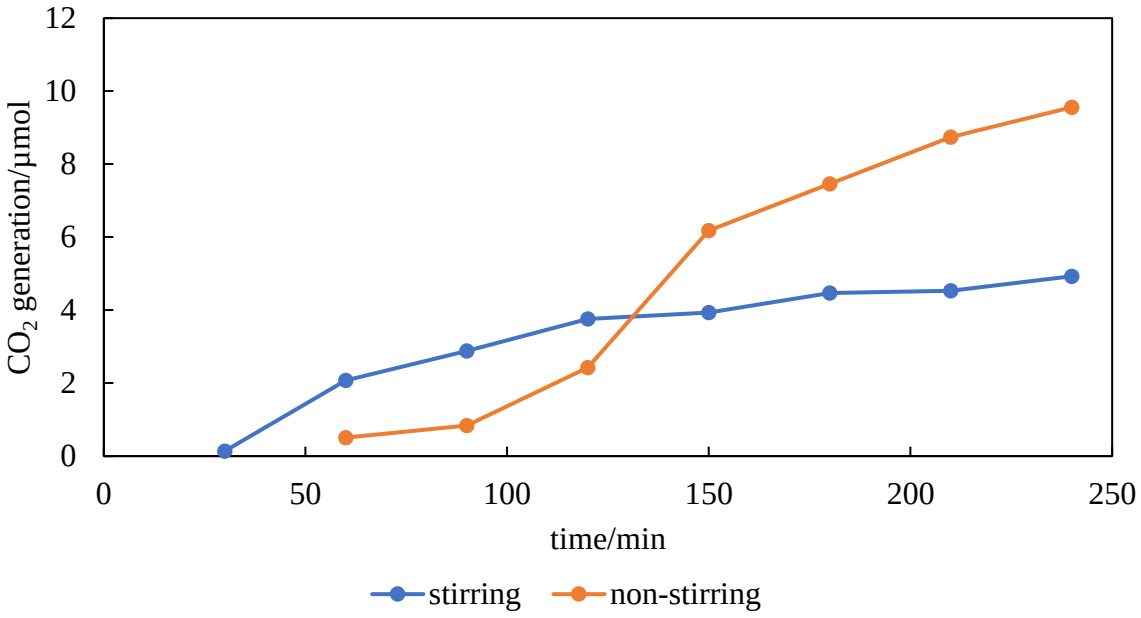

Fig. 4-6. Time-course acetic acid decomposition Au-NP@IOT in non-stirring and stirring condition with 270 nm nanovoid irradiated under monochromatic light irradiation of 530 nm.

4-2-3 Crushed samples

It is rather difficult to have reference sample without the inverse opal structure by retaining the similar components as in Au-NP@IOT, hence the formed Au-NP@IOT sample has been crushed mechanically and brayed using agate mortar to destroy the IOT structure. It should be noted that by braying the Au-NP@IOT sample, the similar component of TiO_2 and Au NP could be retained, thus it would be so suitable to be mentioned as a proper reference sample. Accordingly, Au-NP@IOT samples with original void size of 270 nm (showing the highest activity under 530-nm irradiation) and 290 nm have been crushed and grounded completely using agate mortar. LV-SEM images of the crushed and brayed with original void size of 270 nm are shown in in **Fig. 4-7** The backbone of TiO_2 IO structure has been broken into smaller fragments (ca. 5μm) compared to original periodic structure (ca. 20 μm thickness) with randomly scattered Au NPs and TiO_2 particles, which gave an insight that the formation of PBG would be absent in such structures due to extreme cracks and lack of periodicity (almost none) observed.

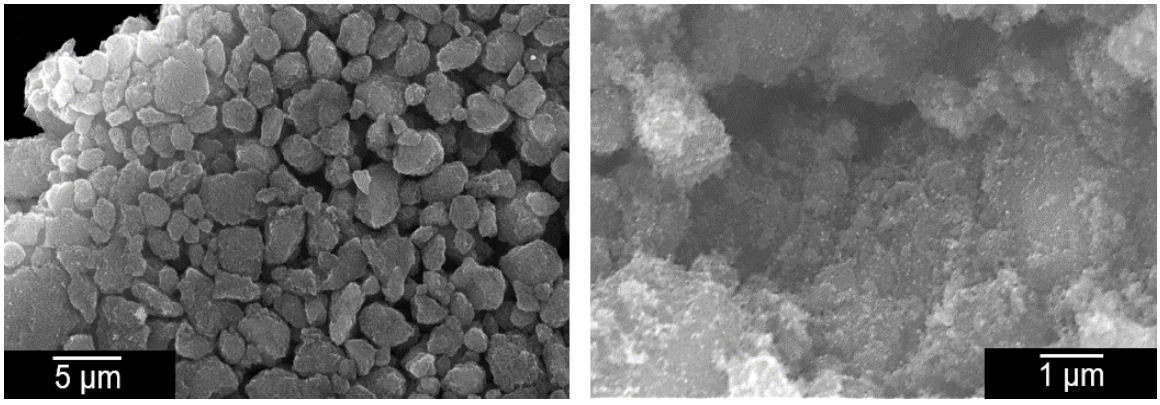

Fig. 4-7. Images of crushed and brayed Au-NP@IOT obtained through LV-SEM observation.

Photocatalytic activity test carried out using the similar condition with irradiation at 530 nm in non-stirring system and the results have been presented **in Fig. 4-8.** It could be clarified that the samples with almost completely destroyed periodic IO structure were inactive under 530 nm irradiation with almost negligible CO_2 liberation in acetic acid-photodecomposition reaction, although the similar amount and LSPR photoabsorption by the

Au are present as compared to reported Au-NP@IOT samples. It is worth to mention that sample with the highest-activity 270 nm void-space lost the activity almost completely (to the dark-reaction level) after the braying process (shaded region in **Fig. 4-8**) indicating the loss of multiscattering phenomenon which hinder the slow photons propagation. Thus, it is possible to further clarify and prove that the photoabsorption enhancement could be achieved only by matching wavelengths of photoirradiation, photoabsorption of gold and estimated PBG edge, proving by slowed photons in Au-NP@IOT.

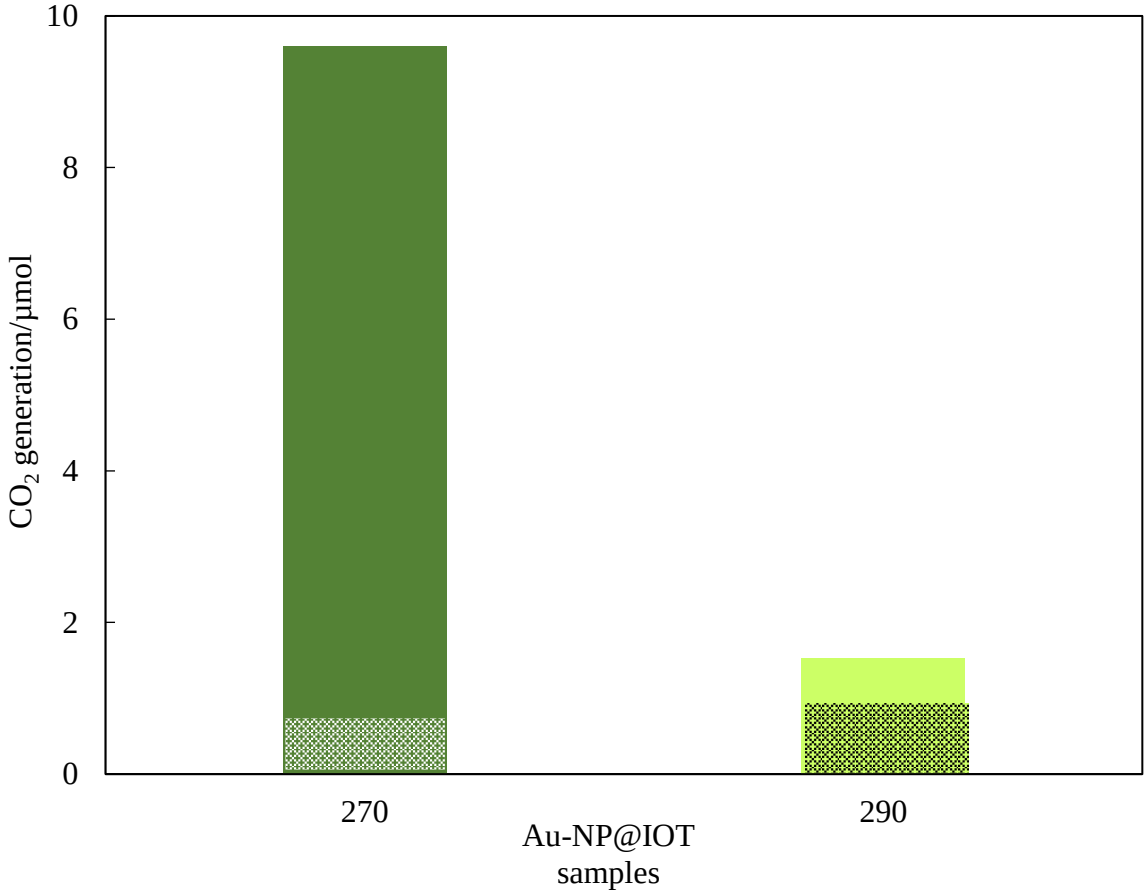

Fig. 4-8. Photocatalytic activities for Au-NP@IOT samples with average nanovoid of 270 nm (darker green) 290 nm (lime) and the respective crushed samples (shaded) irradiated under 530 nm LED emission for 4 hours.

4-3 450-nm LED emission

It has been known the enhancement of activity by possible overlapping of slow photons and plasmonic effect has been suggested but polychromatic irradiation ($\lambda > 420$ nm) has been used. Therefore, the enhancement might be attributed mainly to the TiO_2 photoabsorption rather than solely from LSPR effect as TiO_2 could also absorb light till 450 nm. Accordingly, in this study, photocatalytic activity for five Au-NP@IOT samples with different nanovoids have been carried out under blue monochromatic irradiation ($\lambda = 450$ nm) to further investigate the photoabsorption enhancement due to the overlapping of triply wavelengths of PBG edge, absorption by photocatalyst and LED. **Fig. 4-9** shows the photocatalytic activity using acetic acid decomposition for five Au-NP@IOT samples which has been carried out in non-stirring system.

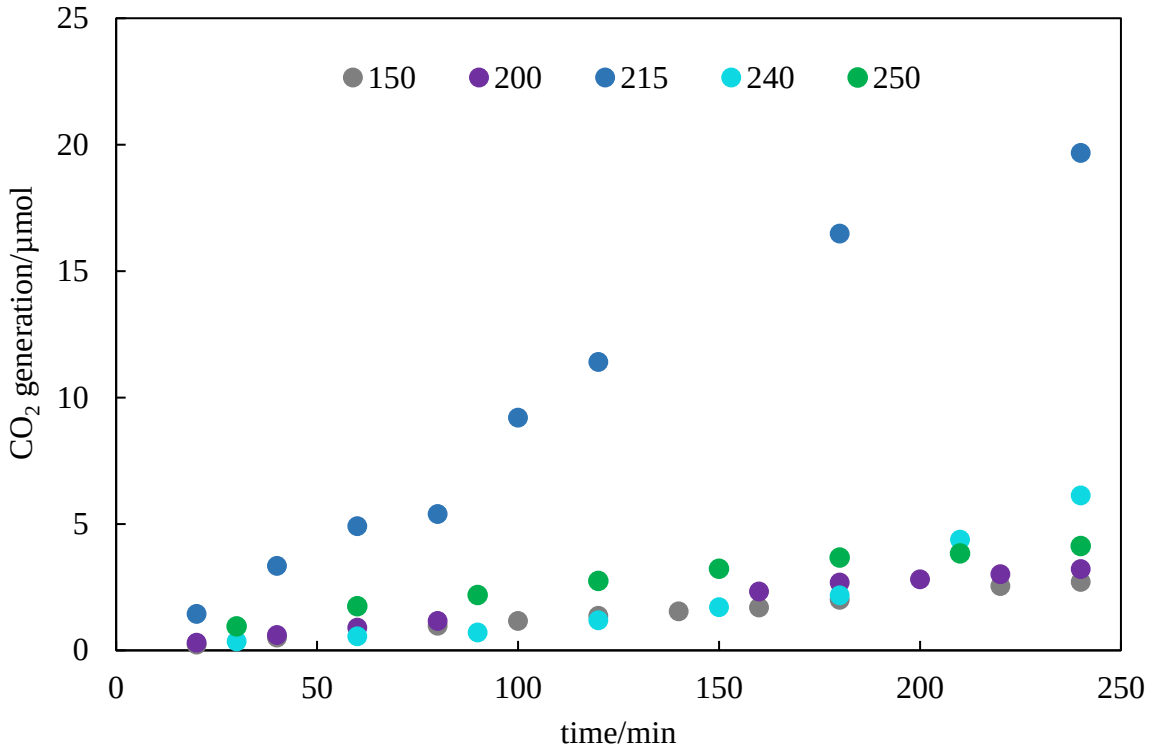

Fig. 4-9. Time-course acetic acid decomposition on Au-NP@IOT samples irradiated under monochromatic light irradiation of 450 nm for 4 hours.

Amplified photocatalytic activity has been only observed using Au-NP@IOT with an average nanovoid of 215 nm similar to the results under 530 nm LED irradiation, only the sample with PBG edge correlating with LED emission (ca. 450 nm) exhibits high activity (**Fig. 4-10**). Interestingly, the respective bare sample (IOT without Au) shows also much lower photocatalytic activity (similar to data under 530 nm). However, this cannot be considered as plasmonic effect (no LSPR effect at 450 nm), but well-known function of noble-metals (since Kraeutler studies in 80s) [Kraeutler 1978] i.e., electron scavenging which inhibits charge carriers' recombination.

For comparison, different reference IOT samples have also been tested and obtained results are shown **Fig. 4-11**. Indeed, almost in all cases, gold-modified samples show higher activity than respective bare IOT. However, the most interesting is that the activity of bare IOT of 215 nm void is higher than activities of Au-NP@IOT samples with different void diameters, and thus confirming that acceleration of activity is only possible when slow photon effect matches irradiation wavelengths and photocatalyst absorption (here TiO_2). Accordingly, it has been shown that reported activity under polychromatic irradiation for wavelength longer than 400 nm cannot prove plasmonic photocatalysis on gold-containing photocatalysts. Therefore, either longer irradiation (> 450 nm) or monochromatic irradiation source should be applied.

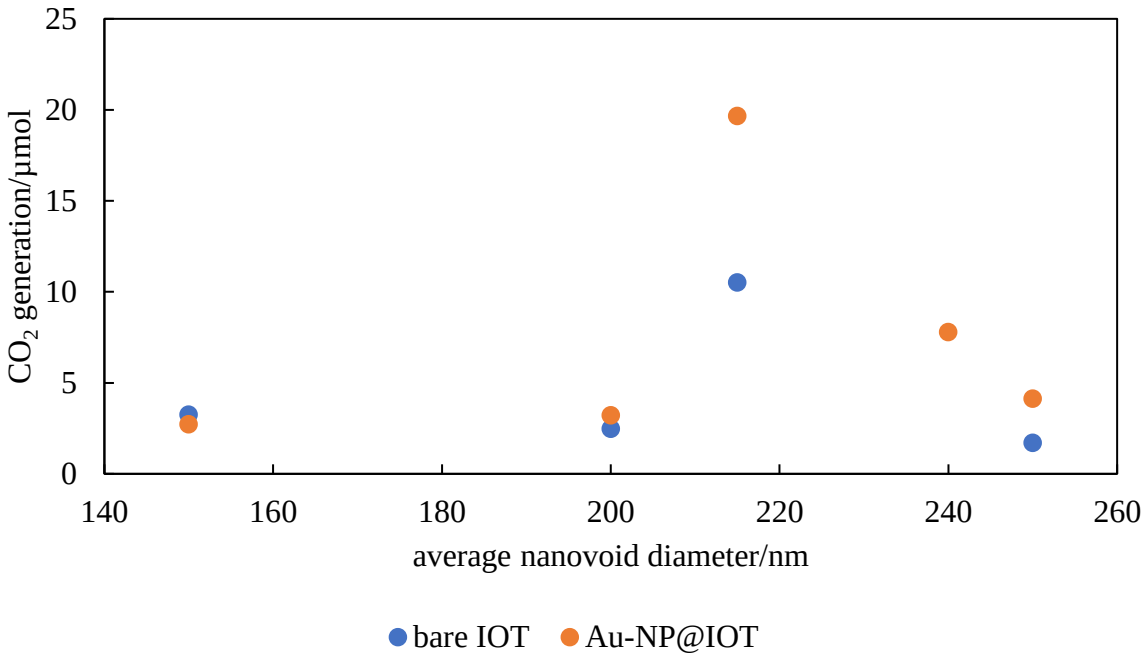

Fig. 4-11. Photocatalytic activity for Au-NP@IOT and IOT sample with respective nanovoids irradiated under monochromatic light irradiation of 450 nm for 4 hours.

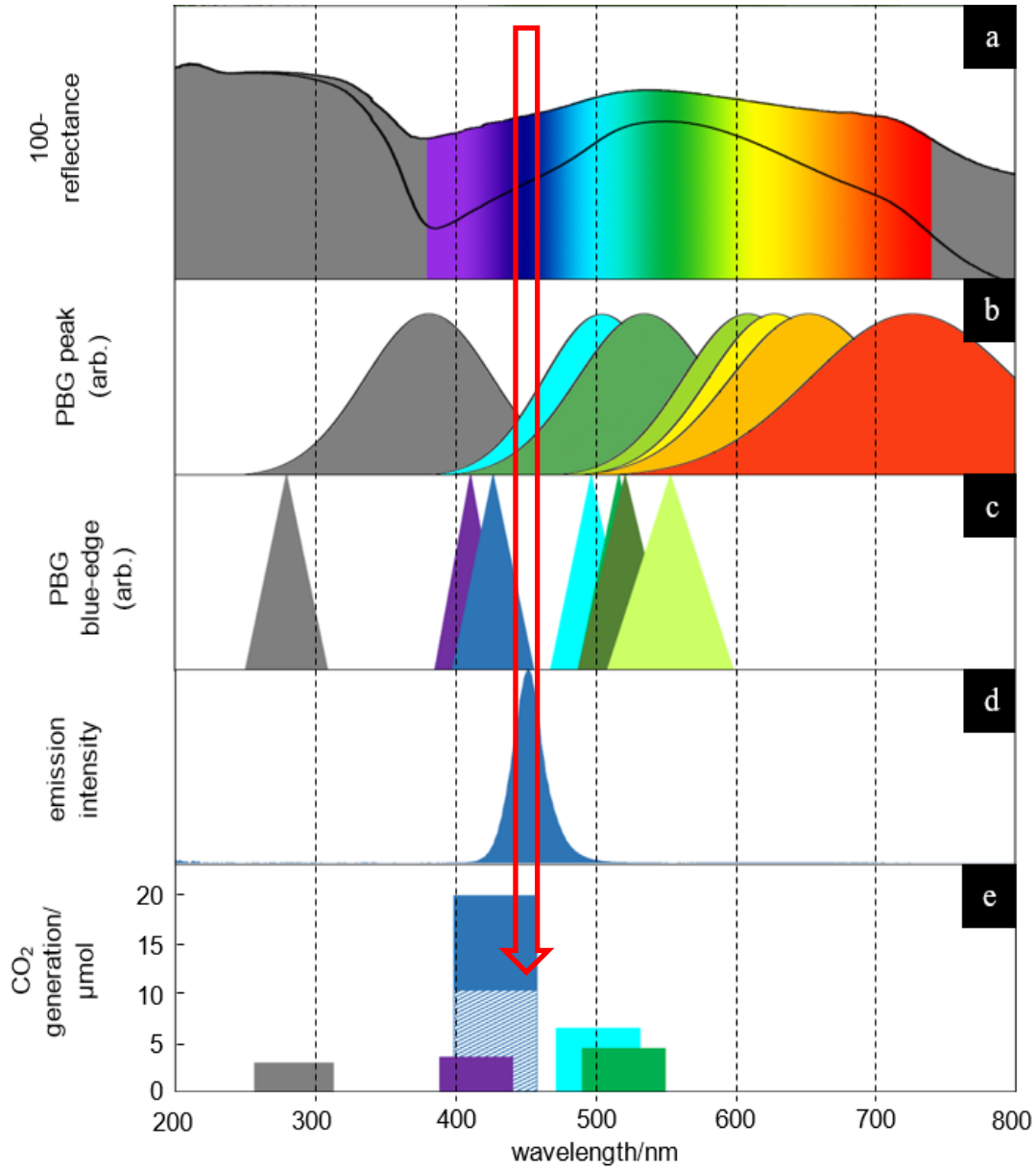

Fig. 4-10. Matching of photoabsorption properties with resultant photocatalytic activities for Au-NP@IOT samples with different nanovoid diameters; [a] representative DRS spectra of Au-NP@IOT with Au NP of 44 nm (upper) and 30 nm (below) [b] PBG peak for Au-NP@IOT samples with nanovoid 150 nm (grey) 200 nm (light blue) 215 nm (green) 240 nm (light green) 250 nm (yellow) 270 nm (orange) 290 nm (red) [c] PBG blue-edge wavelengths for Au-NP@IOT samples with average nanovoid of 150 nm (grey) 200 nm (purple) 215 nm (blue) 240 nm (sky blue) 250 nm (green) [d] 450 nm LED emission spectra [e] CO_2 generation by Au-NP@IOT samples with bare IOT-215 (shaded) (other colours same as [c]).

4-4 Elucidation on the photoabsorption-efficiency enhancement

Based on the results reported in **Section 4-2 and 4-3**, some clear aspects have been pointed out mainly on the bright-side design of photoreaction rate, focusing on the enhancement in the photoabsorption. In the case of the fixed-wavelength LED emission at 530 nm, dependence of the photocatalytic activity rate on the void spaces has been observed, with the fact that the amplified photodecomposition of acetic acid is evident when the wavelength of irradiation, Au NP absorption and the estimated PBG blue-edge are triply matched. As illustrated in **Fig. 4-12**, light has been multiscattered across the periodic structure of Au-NP@IOT, causing the forbidden light propagation at certain wavelengths, i.e., PBG peak depending on the nanovoid. Slow photons arising from the edge of the PBG wavelengths have been well utilized by the Au NPs in the void when the slow photons wavelength matches precisely with the LSPR effect and irradiation source. The LSPR would be intensified in the presence of slow photons as clearly shown by the comparison with other PCs of PBG mismatched with LSPR of gold (**Section 4-2**). Hence, an amplified photoabsorption efficiency has been achieved in the bright-part process prior the chemical reactions that would take place in the dark-part process to give out the total quantum efficiency of the photocatalysis.

In the case of 450 nm LED emission, the same mechanism could be applied by the intensified photoabsorption by the high dielectric medium, i.e., TiO_2 when the slow photons match the photobsorption wavelength. However, different role of Au NP should be considered since there is no plasmonic effect at 450 nm. Accordingly, gold could only accelerate photocatalytic activity by electron scavenging, i.e., improving of the dark part of photocatalysis. Anyway, the significant enhancement of photocatalytic activity is only obtained when triply-matched wavelengths is achieved, i.e., PBG edge, LED emission and TiO_2 photoabsorption.

The possible mechanism on how the dark part under 530 nm LED irradiation i.e., chemical reactions proceed after the photoabsorption by Au-NP@IOTs could be the hot electrons transferred to the conduction band of TiO_2 overcoming the Fermi level barrier [Tian 2005 / Kowalska 2010] and utilized for the photodecomposition of acetic acid that might proceed by radical's formation, as discussed in **Chapter 1**. In contrast, under 450 nm irradiation, gold cannot be excited and thus only titania can be activated, even though usually its absorption edge is at ca. 400 nm, considering some disorders in its structure. Thus, excited

titania formed charge carriers, participating in acetic acid decomposition (both by photogenerated holes and reactive oxygen species formed from oxygen, water and photogenerated electrons). Interestingly, only sample with slow photon effect ca. 450 nm shows significant acceleration of photocatalytic activity and thus bright part enhancement, i.e., enhanced photoabsorption efficiency leads to high photocatalytic performance. In summary, the results shown in **Figs. 4-2 (a)** and **4-10 (e)** suggest that any photoabsorption (TiO_2 or Au-NP) followed by chemical reactions, regardless of their reaction mechanism, can be enhanced by matching the wavelength of photoirradiation and estimated PBG-edge wavelength.

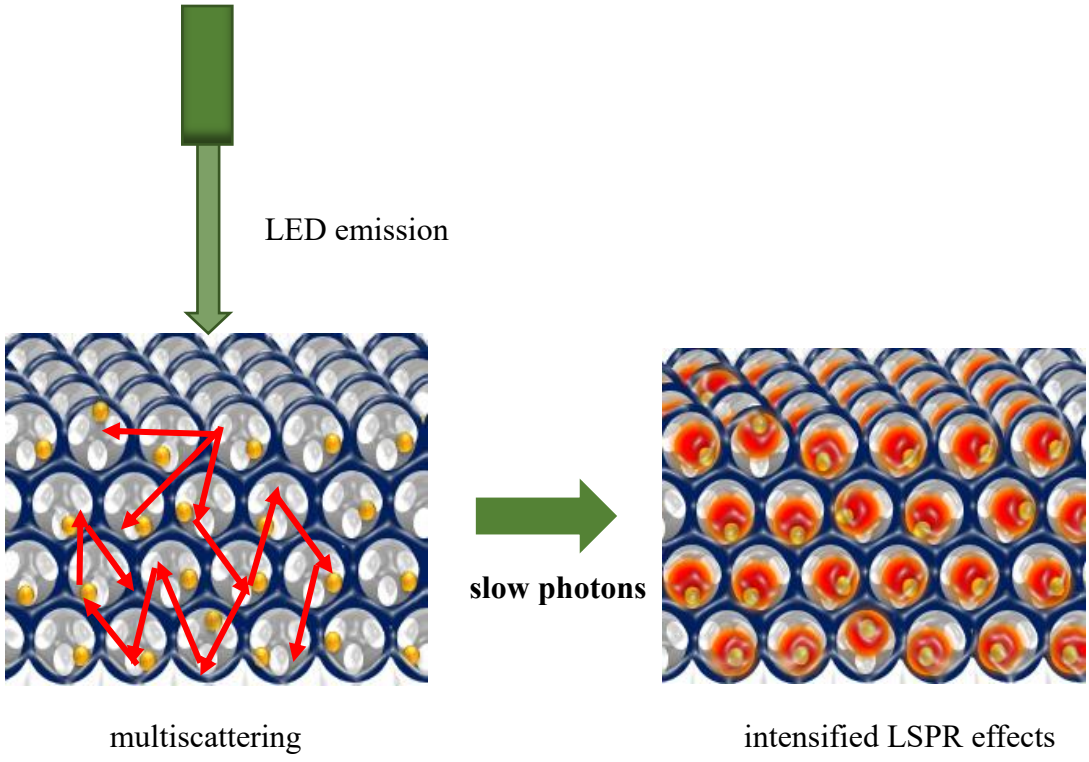

Fig. 4-12. Bright part mechanism for enhanced photocatalytic activity under 530 nm LED irradiation.

4-5 References

Dinh, C.; Yen, H.; Kleitz, F.; Do. T. Three-Dimensional Ordered Assembly of Thin-Shell Au/TiO_2 Hollow Nanospheres for Enhanced Visible-Light-Driven Photocatalysis. *Angew. Chem. Int. Ed*. **53**, 6618 –6623 (2014).

Kowalska, E.; Mahaney, O.O.P.; Abe, R.; Ohtani, B. Visible-light-induced photocatalysis through surface plasmon excitation of gold on titania surfaces. *Phys. Chem. Chem. Phys.***12**, 2344–2355 (2010).

Kraeutler, B.; Bard, A.J. Heterogeneous photocatalytic preparation of supported catalysts. Photodeposition of platinum on TiO_2 powder and other substrates. *J. Am. Chem. Soc.* **100**, 4317–4318 (1978).

Tian, Y.; Tatsuma, T. Mechanisms and applications of plasmon-induced charge separation at TiO_2 films loaded with gold nanoparticles. *J. Am. Chem. Soc.* **127**, 7632–7637 (2005).

Wang. Y.; Xiong, D-B.; Zhang, W.; Su, H.; Liu, Q.; Gu, J.; Zhu, S.; Zhang, D. Surface plasmon resonance of gold nanocrystals coupled with slow-photon-effect of biomorphic TiO_2 photonic crystals for enhanced photocatalysis under visible-light. *Catal. Today*. **274**, 15-21 (2016).

Zhao, H et al. Blue-edge slow photons promoting visible-light hydrogen production on gradient ternary 3DOM TiO_2-Au-CdS photonic crystals. *Nano Energy* **47** 266–274 (2018).

Chapter 5

Formation, characterization and photocatalytic activity of three-dimensional Au NP loaded on IOTs

5-1 Introduction

In order to confirm the importance of Au NPs incorporated inside IOT structure, Au NPs have been deposited on the surface of IOTs by two methods, i.e., hydrothermal and photodeposition method. It was estimated and measured via FAAS measurement (**Chapter 3**) that ca. 5 wt% of Au NPs have been loaded in Au-NP@IOT, thus similar amount of Au NPs was deposited on surface of IOT via hydrothermal method. In the other hand, due to unfavorable results obtained by hydrothermal method, photodeposition method was opted to load Au NPs and tested for photocatalytic activity.

5-2 Au loaded on IOT via hydrothermal method

Hydrothermal method has been attempted to load Au NPs on IOT PC, as it has been reported that stable photocatalysts could be achieved due to the interphase sintering between TiO_2 backbone [Lu 2012]. The resulting sample with greyish colour (as in **Fig. 5-1**) labelled as HM-Au/IOT has 5 wt% of Au loading to be comparable with Au NP loading amount of Au-NP@IOT (ca. 5 wt%). **Fig. 5-1** shows the images obtained from LV-SEM observation. High polydispersity of Au deposits has been noticed ranging from 150 nm to 800 nm, which indicates a mixture of Au NPs and large Au particles. Along with that, aggregation of Au NPs could be

observed in most of the observed areas which could be the hindrance for light penetration and multiscattering into the voids of IOT upon photoirradiation.

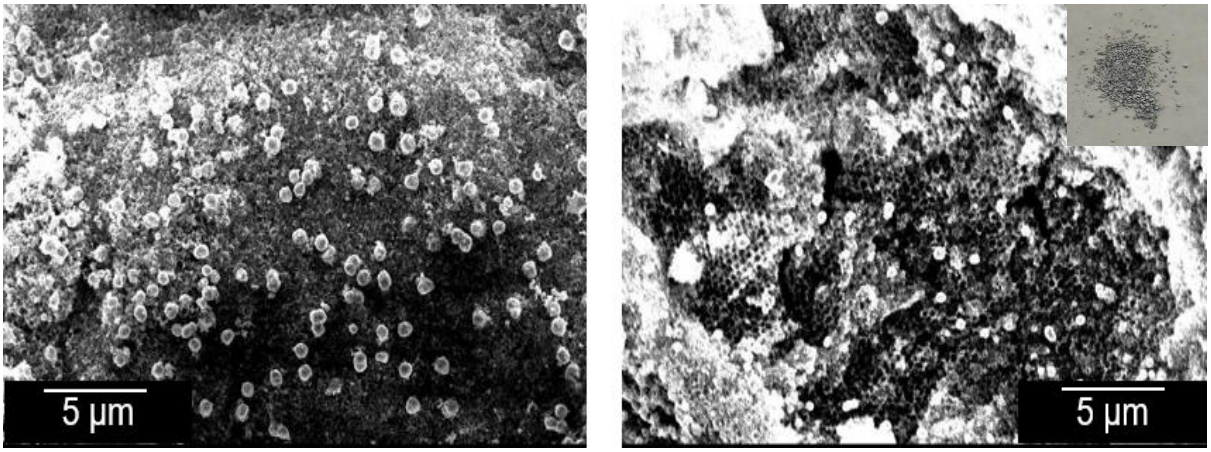

Fig. 5-1. LV-SEM images of HM-Au/IOT.

Crystallinity study has been carried out to determine the crystal planes attributed to TiO_2 anatase and Au peaks and presented as in **Fig. 5-2**. The intensity observed for all the four peaks attributed to Au has been higher compared to both Au-NP@IOT and HM-Au/IOT samples indicating very large content of Au particles and large crystallite size. Indeed, much larger crystallites of 35.1 nm were formed, as estimated from Scherrer equation.

As could be observed **Fig. 5-3**, broad absorption band in the visible wavelength range around ca. 480–750 nm has been observed confirming high polydispersity of gold deposits and their broad LSPR peak. Similar, grey photocatalyst has been reported when gold was photodeposited on large rutile titania particles, and thus resulting in high polydipersity of gold particles, indicating NPs and rod-like deposits [Kowalska 2010]. In this regard, hydrothermal method has been assumed to be not suitable to load higher amount of Au on IOT due to multiarray structure of IOT with appreciable thickness as the formation of Au NP would be limited on the surface of IOT. The formation of very large Au particles would definitely be the barrier for slow photons arise in the nanovoid.

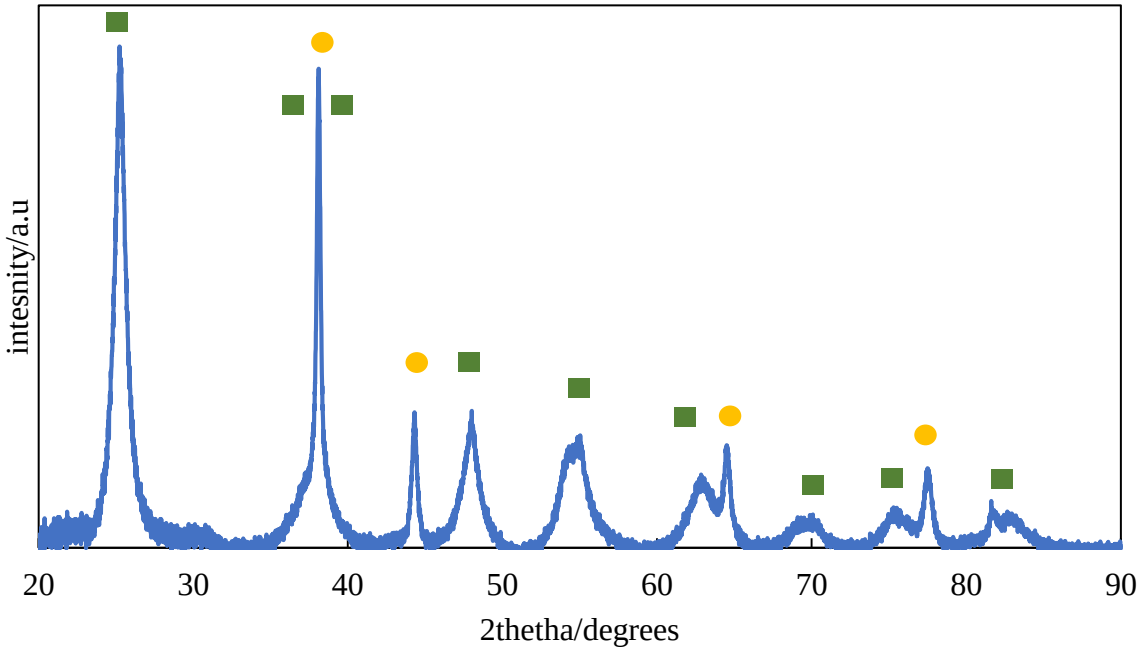

Fig. 5-2. XRD pattern of HM-Au/IOT.

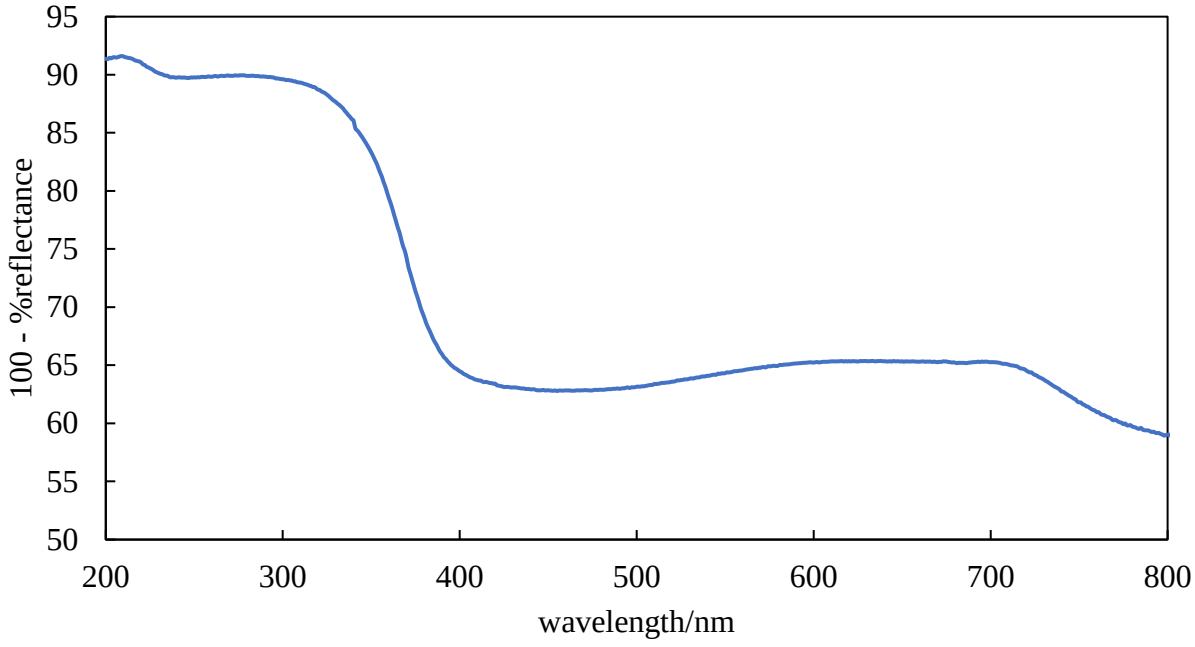

Fig. 5-3. DRS spectra of HM-Au/IOT.

5-3 Photodeposition of Au NPs on IOT

5-3-1 Characterizations

In order to confirm the importance of Au NPs incorporated inside IOT structure for plasmonic photocatalysis, Au NPs have also been deposited on the surface of IOT by photodeposition (PD) method and used as a reference sample (PD-Au/IOT). It is worth to mention that estimated gold content (FAAS measurement) in Au-NP@IOT samples was ca. 5wt% and thus here photodeposition has been started from 5 wt% of Au. Four different amounts of Au have been applied, i.e., 5wt%, 2 wt%, 0.5 wt% and 0.1 wt% in respect to TiO_2. IOT with nanovoids of ca. 270-280 nm (void distribution shown in **Fig. 5-4**) has been selected for this study since similar sample with incorporated Au NPs in void of IOT shows the highest vis activity under 530-nm LED irradiation (**Chapter 4**). The estimated values of PBG edge of both samples, i.e., with Au NPs incorporated (Au-NP@IOT) and deposited on the surface of IOT (PD-Au/IOT), are shown in **Fig. 5-5**. Indeed, similar values of PBG peaks have been obtained reaching ca. 1.88 eV and 1.81 eV for Au-NP@IOT and PD-Au/IOT, respectively corresponds to the blue-edge wavelengths range of 495-558 nm and 499-576 nm. The samples have been labelled in respect to the gold content, i.e., PD-Au5/IOT, PD-Au2/IOT, PD-Au0.5/IOT and PD-Au0.1/IOT.

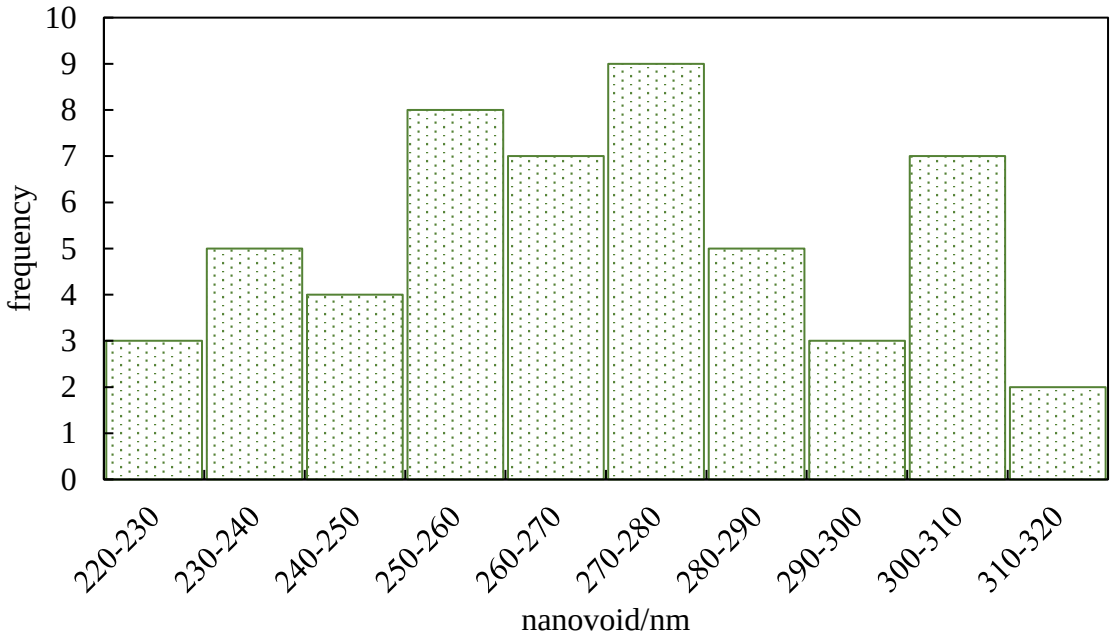

Fig. 5-4. Void-size distribution of IOT sample used for photodeposition.

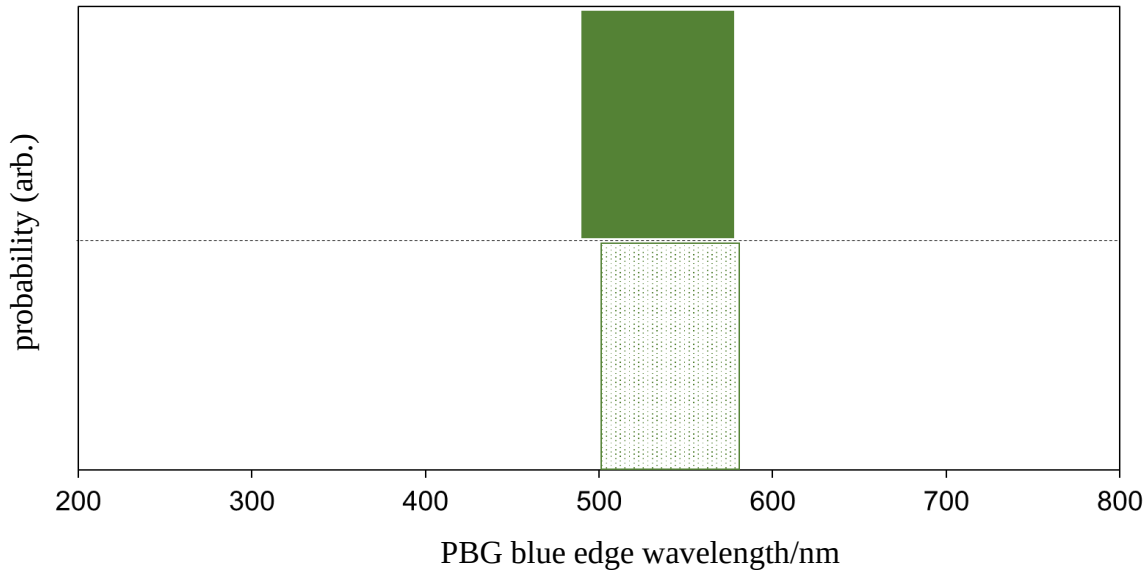

Fig. 5-5. PBG blue-edge wavelegths range of Au-NP@IOT (solid green) and PD-Au/IOT (shaded) with average nanovoid of 270 nm.

In the photodeposition process, methanol has been used as the hole scavenger to inhibit the charge-carriers' (e^- / h^+) recombination since photogenerated electrons are necessary to reduce gold cations (Au^{3+}) forming gold deposits. It has already been reported that all Au ions are efficiently reduced to their metallic state by using this loading method within 15 minutes [Kowalska 2010 / Kowalska 2012]. Hence, all three samples have been irradiated with the mercury lamp under continuous argon bubbling to avoid oxygen presence, which works as an electron scavenger for 1 hour to ensure the complete reduction of gold cations.

PD-Au/IOT samples have displayed purplish with colour intensity depending on the content of gold, i.e., darkest for PD-Au5/IOT (inset in **Fig. 5-6 (a)**) and lightest for PD-Au0.1/IOT (inset in **Fig. 5-6 (g)**). The morphology of PD-Au/IOTs samples is shown in **Fig. 5-6**. In the case of PD-Au5/IOT and PD-Au2/IOT, high polydispersity of gold deposits has been observed with Au NPs ranging from 50 nm to 250 nm and 10 nm to 170 nm, respectively covering the nanovoids and the surface of TiO_2 backbone. Moreover, the aggregation of Au NPs has been seen in many parts of the surface of IOT which might block the multiscattering effect by the PCs, as already reported [Zhang 2013]. It is worth to mention that large Au

particles (>300 nm) observed in HM-Au/IOT were absent in PD-Au5/IOT although the same amount of gold precursor has been utilized in both samples which could be attributed to the continuous argon bubbling throughout the photodeposition process in the latter sample to induce the constant movement of IOTs suspension, resulting in smaller Au particles (< 300 nm) deposition compared to stagnant condition in hydrothermal method.

In the other hand, it should be pointed out that although usually 2 wt% of Au is used for plasmonic photocatalysis resulting in high photocatalytic activity, this amount is only the best for particulate system when Au NPs might be uniformly deposited on titania NPs. In the case of IOT, only small part of bulk TiO_2, i.e., surface, is a support for Au NPs, and thus it is not surprising that significant aggregation of Au NPs has been observed. Therefore, lower content of gold 0.5 wt% has also been tested for photodeposition, which results in more uniform distribution of Au NPs on IOT surface as shown in **Fig. 5-6 (e,f)**. The further reduction in gold content causes the formation of only few Au NPs of small size (ca. 5-10 nm) in the surface and voids of IOT, as seen in **Fig. 5-6 (g,h)**.

In order to estimate the content of gold in all the PD-Au/IOT samples, FAAS measurement has been carried out after Au dissolution from the respective samples in aqua regia. **Table 5-1** shows the relationship between the photodeposited amount (gold precursor) and the detected amount via FAAS measurement. A small difference has been observed for PD-Au5/IOT as 4.5 wt% has been detected compared to the actual deposited amount (5 wt%). The other samples have been in accordance with the respective photodeposited and detected amount, which means all the precursor gold ions have been successfully reduced to metallic gold in the photodeposition procedure that has been carried out.

Table 5-1. Au NP content (wt%) measured in PD-Au/IOTs via FAAS**.**

sample	in-feed (wt%)	Au NP content (wt%)
PD-Au5/IOT	5	4.5
PD-Au2/IOT	2	1.9
PD-Au0.5/IOT	0.5	0.4
PD-Au0.1/IOT	0.1	0.1

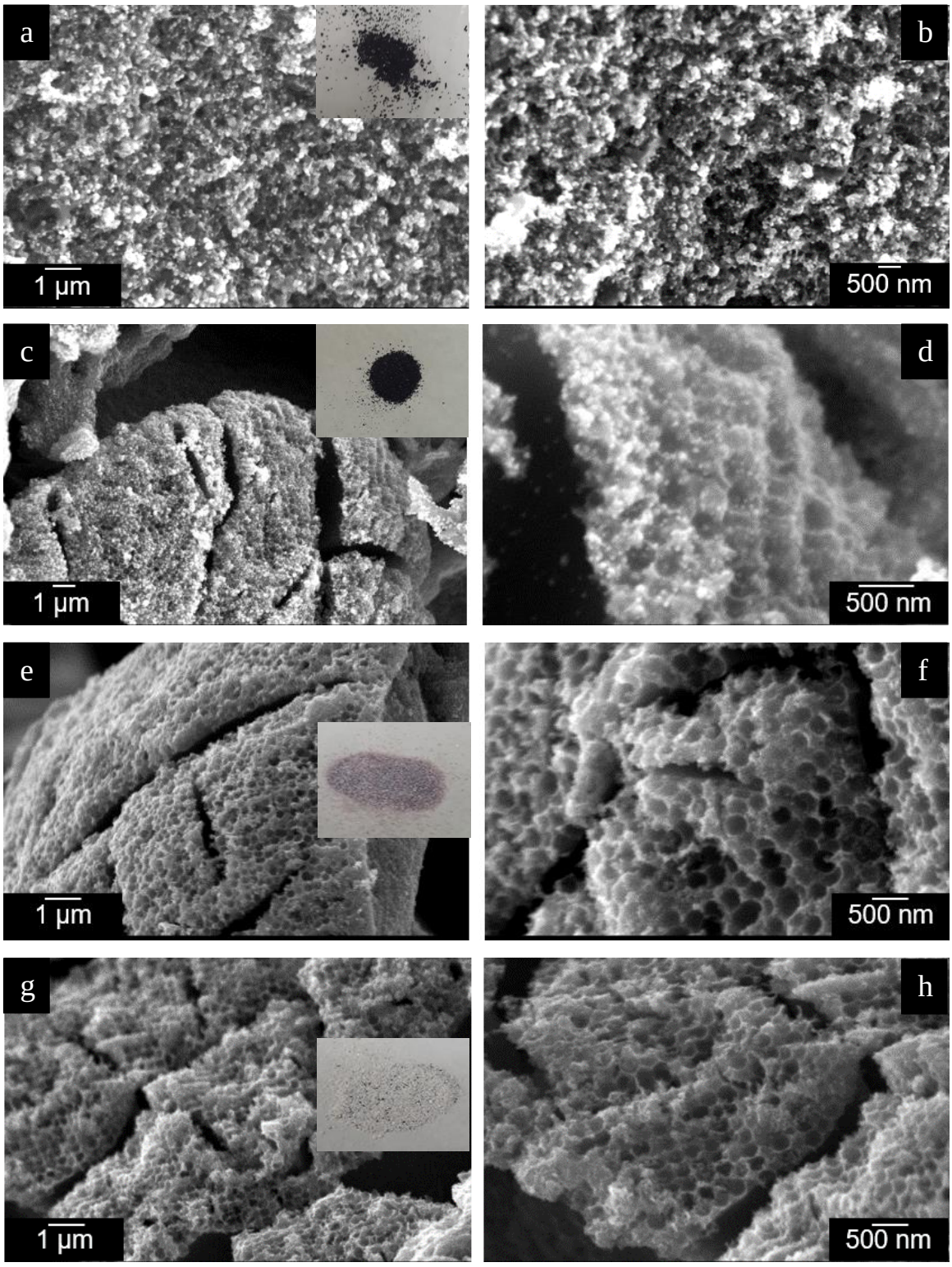

Fig. 5-6. LV-SEM images PD-Au/IOT (a, b) 5wt% (c, d) 2wt% (e, f) 0.5 wt% (g, h) 0.1 wt%.

As presented in **Section 3.2**, it should be noted that PD-Au/IOT samples have also been prepared in powdered form, hence the photonic shoulder (downward peak) has not been observed in DRS spectra (**Fig. 5-7**) due to the random scattering of incident light as IOT PCs dependent on angle of light irradiation [Wu 2014 / Kim 2017]. It should be noted that a shoulder-like flat part at 450 nm which might be attributed to photoabsorption from/to the bandgap or surface states of titania [Waterhouse, 2013] has been observed from all samples except for PD-Au5/IOT. The absence of titania related optical absorption in PD-Au5/IOT sample could be postulated by the blockage and almost total coverage of the Au NPs and Au particles on the TiO_2 backbone as observed in **Fig. 5-6 (a,b)**, hence the photoabsoprtion by TiO_2 has been hindered.

In contrast with Au-NP@IOT photoabsorption spectra that exhibited cumulative broad visible light absorption starting from 400 nm till ca. 700-800 nm, PD-Au2/IOT displayed a shoulder absorption at ca. 300-340 nm which might be attributed to very small Au NP (less than 5 nm) as reported in previous studies [Esumi, 2004] apart from broad absorption from ca. 480 nm-600 nm representing the LSPR effect. Aggregation of Au NPs on this specific sample has been quite severe leading to high polydispersity of the plasmonic NPs. On the other hand, very weak LSPR photoabsorption has been noticed for PD-Au0.1/IOT due to the smaller amount of loading.

XRD analysis has been carried out for PD-Au/IOT samples, as shown in **Fig. 5-8.** All noticeable crystal planes attributed to TiO_2 anatase peaks (JICST 7533) have been observed in all samples with the similar intensities indicating the good repeatability in IOT preparation. As expected, gold has been detected in both PD-Au5/IOT and PD-Au2/IOT samples as indicated by diffraction peaks at 2θ of 38.18°, 44.38°,64.58° and 77.3° for (111), (200), (220) and (311) planes respectively, has not been detected for PD-Au0.1/IOT sample due to too low content of gold. The estimated crystallite size for Au NP for PD-Au5/IOT and PD-Au2/IOT is about 14 nm and 8 nm, respectively whereas could not be detected for PD-Au0.1/IOT due to very low intensity of the Au peak.

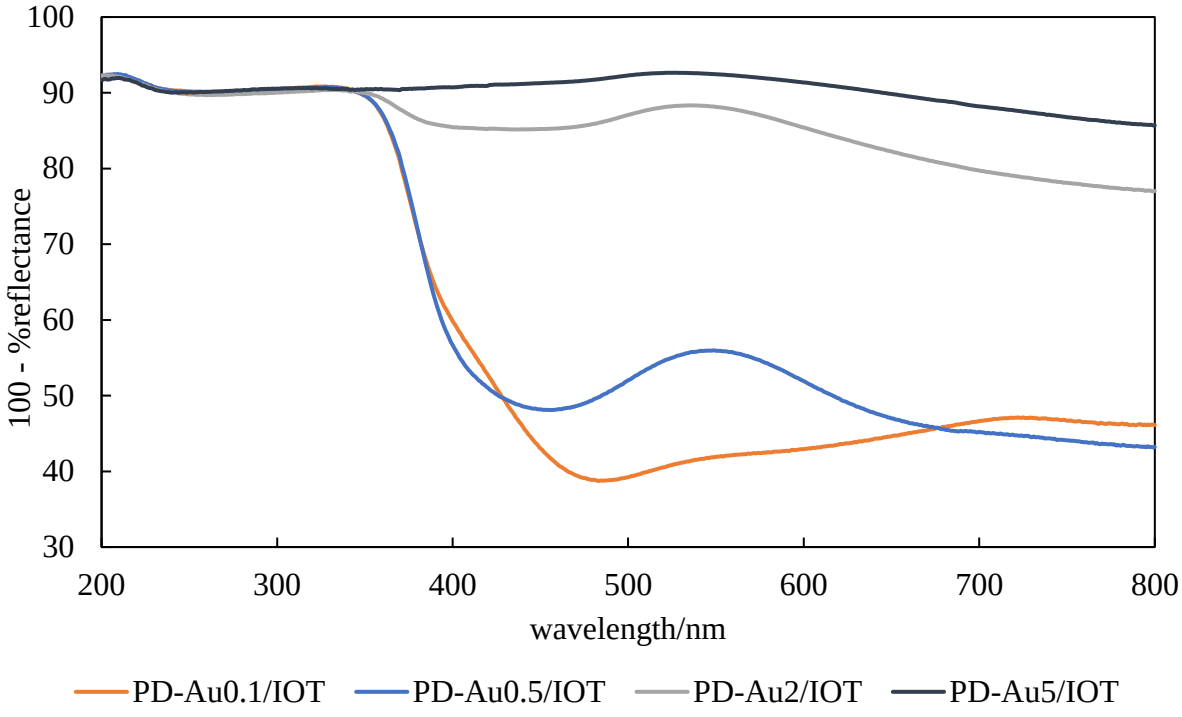

Fig. 5-7. DRS spectra of PD-Au/IOT samples.

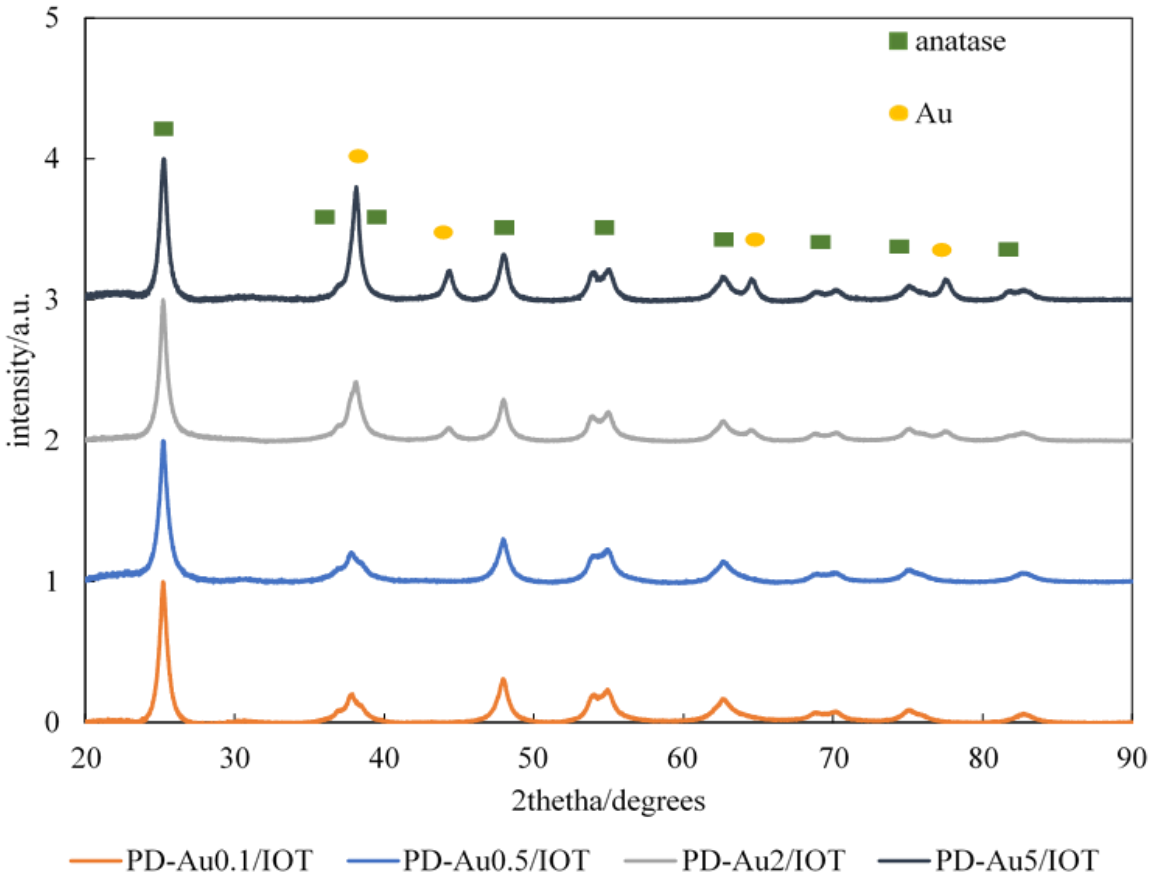

Fig. 5-8. XRD patterns of PD-Au/IOT samples.

5-3-2 Photocatalytic activity of PD-Au/IOTs

The photocatalytic activity of PD-Au/IOT samples have been investigated for oxidative decomposition of acetic acid under same conditions as those used for Au-NP@IOT samples testing (**Section 4.1**). **Fig. 5-9** shows the time-course data for all four samples during 4 hours irradiation. As could be observed, all samples exhibit very low activity, especially PD-Au2/IOT and PD-Au0.1/IOT samples.

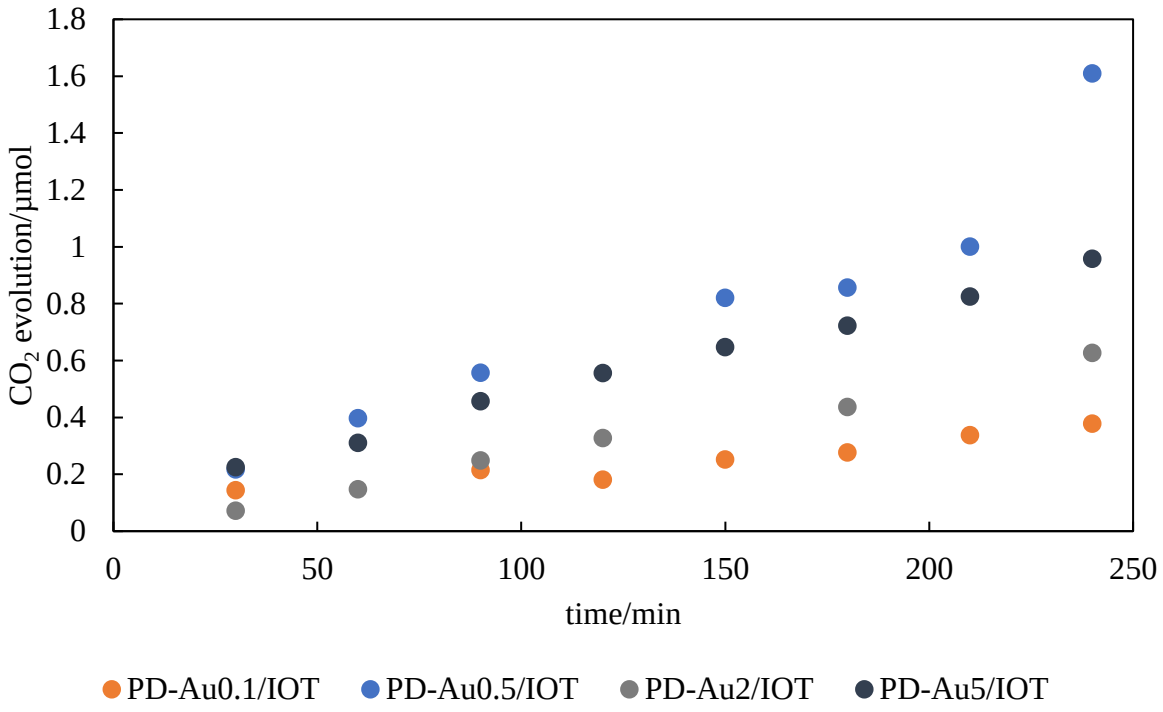

Fig. 5-9. Time-course curve of photocatalytic activity for PD-Au/IOT samples irradiated under monochromatic light irradiation of 530 nm for 4 hours.

It is known that amount of gold is crucial for vis activity. For example, an optimum gold content for fine titania NPs, and three-step increase of activity with an increase in gold content from 0.1 to 10 wt% for large titania particle have been reported for particulate system [Kowalska 2012]. It has been suggested that in the case of titania NPs, 2 wt% of gold results in dark photocatalysts and thus hindered light penetration. Interestingly, among various commercial titania samples modified with 7 wt% of gold by photodeposition, the highest activity was observed by the less intense colour (but with broad LSPR peak) [Kowalska 2010].

Indeed, PD-Au5/IOT and PD-Au2/IOT with very dark purplish colour exhibits much lower activity than PD-Au0.5/IOT sample. In this regard, although larger Au NPs with more intense photoabsorption effect which could lead to larger number of photons absorption has been formed, the importance of void spaces without much material incorporated inside PCs has been highlighted. In the case of PD-Au0.1/IOT, the possible reason for negligible LSPR effect could be attributed to the low number of Au NPs that has been photodeposited on IOT. Although there have been some Au NPs placed inside the void spaces in optimum amount (1 or 2 Au NPs and also aggregated Au NPs), most of the voids have been seen empty without the photoabsorbing material. In fact, the LSPR effect has been very weak as proven in DRS spectra at ca. 530-nm (**Fig. 5-7**) and absence of Au peaks in XRD analysis (**Fig. 5-8**). The highest activity among of the three samples has been achieved by PD-Au0.5/IOT, however the performance has been similar to the lowest activity reported by Au-NP@IOTs that did not have triplicate wavelengths matching. (**Fig. 5-10**) shows the comparison of photocatalytic performance in between Au-NP@IOTs and PD-Au/IOTs with the similar nanovoid diameter range (270 nm) and PBG blue-edge wavelengths region.

It should be noted that about 5-fold and 9-fold of photocatalytic activity amplification by Au-NP@IOT has been observed compared to PD-Au0.5/IOT and other three photodeposited Au NPs on IOTs respectively. The absence of photoabsorption enhancement in all the four photodeposited samples highlights the importance of having only one Au NP with similar size and shape in each void as the photoabsorping material. In fact, the presence of slow photons in the void spaces could be ineffective for better photoabsorption by Au NPs due to their differences in amount and size/shape on TiO_2 PC. Thus, without knowing the optimum loading amount of Au NP that could enhance the photocatalysis process by plasmonic based PCs, it is indeed difficult to understand the role of Au NPs which more likely would act as co-catalyst, i.e., mediator for better separation of photogenerated carriers [Cushing 2014] rather than successful overlapping of photonic and LSPR effects that could lead to photoabsorption enhancement. It should be pointed out that high weight percentage (5 wt%) of Au NP have been incorporated in newly designed Au-NP@IOT samples without the formation of aggregation and polydispersity. This could be contrast for the gold deposited inverse opal structure as even the equal or lower loading percentage such as 5 wt% and 2 wt% of gold could lead to unlikely phenomenon such as screening effect, aggregation and high polydispersity. Accordingly, utilization of Au-NP@IOT would be most profitable to prevent the problems on

agglomeration, large Au NP size distribution and coverage on nanovoid spaces (screening effect) similar to usual noble metals modified TiO_2 structures [Wang, 2018].

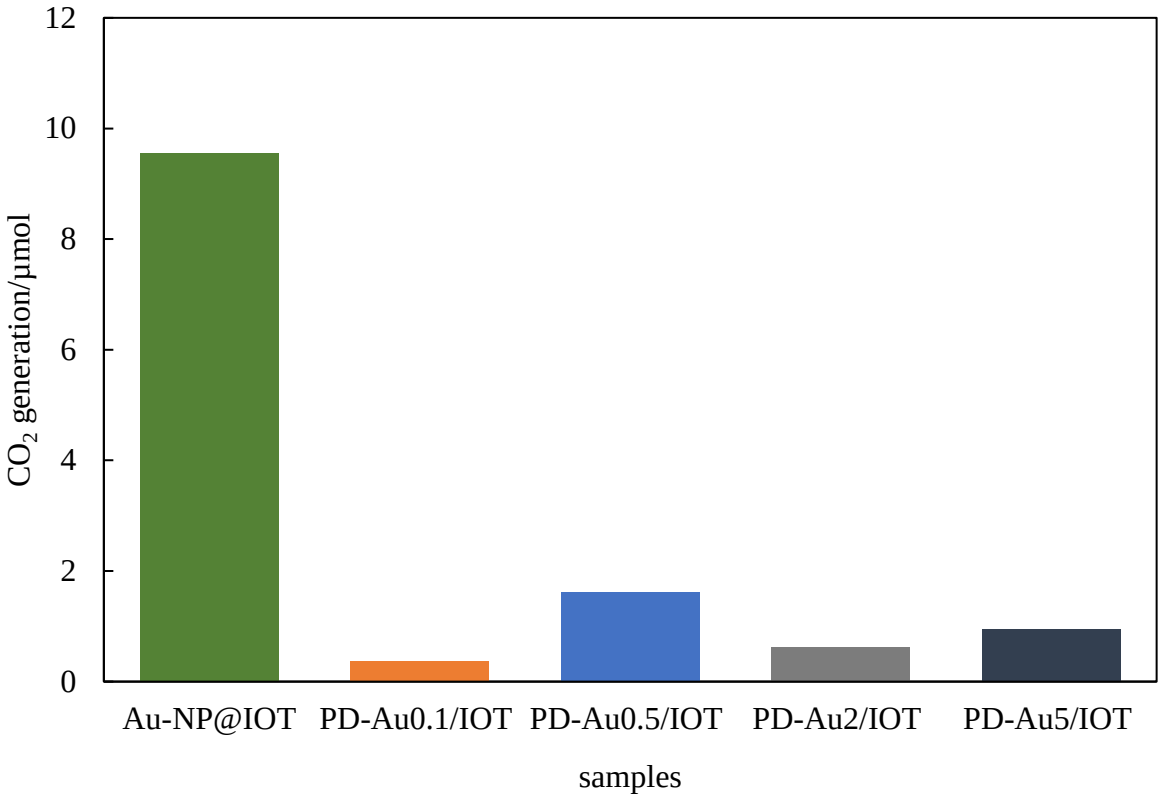

Fig. 5-10. Photocatalytic activity performance of Au-NP@IOT and PD-Au/IOTs with similar PBG blue-edge wavelengths irradiated under monochromatic light irradiation of 530 nm for 4 hours.

5-4 References

Esumi, K.; Sarashina, S.; Yoshimura, T. Synthesis of Gold Nanoparticles from an Organometallic Compound in Supercritical Carbon Dioxide. *Langmuir* **20**, 5189–5191 (2004).

Kim, W. T.; Choi, W. Y. Fabrication of TiO_2 photonic crystal by anodic oxidation and their optical sensing properties. *Sens. Actuator A: Phys.* **260,** 178–184 (2017).

Kowalska, E.; Mahaney, O. O. P.; Abe, R.; Ohtani, B., Visible-light-induced photocatalysis through surface plasmon excitation of gold on titania surfaces. *Phys. Chem. Chem. Phys.*, **12**, 2344–2355 (2010).

Li, J. T.; Cushing, S. K.; Zheng, P.; Senty, T.; Meng, F. K.; Bristow, A. D.; Manivannan, A.; Wu, N. Q. Photocatalytic Activity Enhanced by Plasmonic Resonant Energy Transfer from Metal to Semiconductor. *J. Am. Chem. Soc.*, **136**, 8438-8449 (2014).

Lu, Y.; Yu, H.T.; Chen, S.; Quan, X.; Zhao, H.M. Integrating plasmonic nanoparticles with TiO_2 photonic crystal for enhancement of visible-light-driven photocatalysis. *Environ. Sci. Technol.* **46**, 1724–1730 (2012).

Wang, K.L.; Wei, Z.S.; Ohtani, B.; Kowalska, E. Interparticle electron transfer in methanol dehydrogenation on platinum-loaded titania particles prepared from P25. *Catal. Today* **303**, 327–333 (2018).

Waterhouse, G. I. N.; Wahab, A. K.; Al-Oufi,; Jovic, V.; Anjum, D. H.; Sun-Waterhouse, D.; Llorca, J. and Idriss, H. Hydrogen production by tuning the photonic band gap with the electronic band gap of TiO_2. *Sci. Rep.*, **3**, 2849–2849-5 (2013).

Wu, M.; Liu, J.; Jin, J.;Wang, C.; Huang, S.Z.; Deng, Z.; Li, Y.; Su, B. L. Probing significant light absorption enhancement of titania inverse opal films for highly exalted photocatalytic degradation of dye pollutants. *Appl. Catal. B: Environ.* **150– 151,** 411– 420 (2014).

Zhang, Z.; Zhang, L.; Hedhili, M.N.; Zhang, H.; Wang, P. Plasmonic gold nanocrystals coupled with photonic crystal seamlessly on TiO_2 nanotube photoelectrodes for efficient visible light photoelectrochemical water splitting. *Nano Lett.* **13**, 14–20 (2012).

Chapter 6

Summary, conclusions, future aspects and achievements

6-1 Summary and general conclusions

The main purpose of this PhD is to find an effective strategy to enhance the bright part of photocatalysis, i.e., photoabsorption efficiency of photoabsorbing materials without changing their extinction coefficients. The strategy includes the development of a novel plasmonic nanostructure and to clarify the photoabsoprtion enhancement mechanism by comparison of the photocatalytic activity for different samples, i.e., with and without the plasmonic material (Au-NP), and for different photonic properties (PBG).

Firstly, a design of a novel structure by gold-modified PCs has been successfully developed, in which Au NP has been present in each void of IOT structure (Au-NP@IOT). The procedure, used for three-dimensional powdered Au-NPs@IOT preparation, consists of five steps, as discussed in previous chapters. Au NPs have been incorporated in each nanovoid, which is the key factor for achieving the effective photoabsorption enhancement as the slow photons are present only inside the nanovoids (not on its surface). The nanovoid diameter of PCs has been successfully controlled by the SiO_2 thickness in the second step without changing the overall structure, resulting in preparation of PCs with different photonic properties (PBG positions and PBG edge wavelengths—representing the slow photons propagation regions). Au NPs have retained in each nanovoid upon template removal, resulting in similar photoabsorption properties of obtained Au-NP@IOT photocatalysts with LSPR peak at ca. 530 nm. The absence of PBG peak has been attributed to the powdered form of PCs, i.e., being probably caused by the random direction of reversed opal crystal planes, leading to the broad visible light absorption at 400 nm to 700 nm for all the samples.

Secondly, it is proposed that bright-part efficiency can be enhanced by intelligent design of photocatalytic materials to match wavelengths of the irradiation, absorption and PBG edge. In the case of 530-nm LED irradiation, an amplified photocatalytic activity is observed only for the specific sample with average nanovoid of 270 nm that matches the PBG edge and photoabsoprtion by Au NPs (since LSPR position of all samples is practically same). The hypothesis is further proven by almost negligible activity of bare IOT of same void size as that in the most active Au-NP@IOT sample since only gold can absorb light at this region (inactive titania). In the case of 450-nm LED irradiation, sample with PBG edge close to 450 nm has exhibited the highest activity. Since the LSPR effect is at the minimum strength at this particular wavelength, the possibility of enhanced Au-NP photoabsorption leading to enhanced overall activity might be excluded. However, the activity of respective IOT sample (without Au NPs, but with same voids as the most active Au-NP@IOT sample at 450-nm irradiation) has been much lower than that by Au-NP@IOT, but clearly higher than that for the other Au-NP@IOT samples. Hence, it is thought that rather TiO_2 than gold should be the photoabsorping material in this system, whereas Au NPs should work as a co-catalyst for photogenerated electrons' scavenging. These findings strongly indicate that previous studies on photoreaction enhancement for plasmonic-based PCs under polychromic irradiation (> 420 nm) do not confirm that activity enhancement is necessarily caused by the overlapping of LSPR and photonic effect as PCs could also be the photoabsorbing material (like TiO_2).

Thirdly, the importance of retaining the periodic structure of PCs has been highlighted in this study. The lower photoreaction rate (2-fold) under the stirring than that in non-stirring conditions indicates the weakened multiscattering effect in the nanovoid as the layers of light propagation is disrupted.

Lastly, the importance of this novel structured material by having Au NP in each void has been highlighted by comparing with Au-NP-loaded IOTs. Accordingly, utilization of Au-NP@IOT would be most profitable to prevent the gold aggregation (and even possible loss during activity testing).

In conclusion, this study is the first report to propose a novel bright-part design in terms of the photocatalyst architecture and elucidation on the photoabsorption enhancement for the improvement of the overall photocatalytic performance. The results give general insights on (i) pathway to enhance the overall photoreaction rate by improving the initial process that takes place in photocatalysis, i.e., enhancement in photoabsorption efficiency ability without

changing the extinction coefficient of the photoabsorbing material, (ii) the ability of photoabsorping material to drive the photocatalytic reaction with the aid of slow photons from PCs, which overlap with LSPR effect and proved by monochromatic irradiation, (ii) the importance of having the photoabsorping material inside the voids space of PCs with controlled size/shape.

6-2 Future aspects

The following aspects are proposed for the extension of this thesis.

(i) Considering that slow photons are available only at an appropriate angle of incident light, only some part of the photons is slowed down. This seems similar to powder X-ray diffraction analysis and suggests that much larger enhancement might be obtained by fixed-angle irradiation to highly oriented IOT layers. Hence, two-dimensional Au-NP@IOT on substrates could be explored to study on the incident light angle dependence along with the triplicate wavelengths matching.

(ii) Precise control of uniform void size during preparation of Au-NPs@SiO_2 would lead to further enhancement of photoabsorption as appreciable nanovoid size distribution has been observed in this study.

(iii) Different materials as photoabsorber, such as other noble metals (silver, platinum) or metal oxides could be explored and carry out precise tuning to allow the triply wavelengths matching. Apart from that, other materials for photonic crystal that gives higher or lower refractive index could be investigated.

The following point are still open questions.

(iv) Clarifications on dark-part mechanism, i.e., the reaction that occurs after the photoabsorption, which leads to the utilization of the photogenerated charge carriers by the reactants. In this study, plasmonic effect has been evident for irradiation under 530 nm, thus three possible mechanisms should be considered: 1) charge transfer, i.e., the transfer of “hot” electrons, (2) energy transfer, and (3) plasmonic heating (thermal activation), as discussed in Chapter 1.

6-3 Achievements

6-3-1 Awards

Best presenter award for presentation entitled ‘Titania inverse-opal photonic crystals incorporating a gold nanoparticle in each void space for light-harvesting enhancement’ in 38th Solid-Surface Photochemistry Debate held in Miyazaki.

6-3-2 Peer-reviewed papers:

1) Raja-Mogan, T.; Ohtani, B.; Kowalska, E. Photonic crystals for plasmonic photocatalysis. ***Catalysts***, 2020, 10(8), 827 (IF=3.52) selected as ***feature paper***.
2) Wang, K.; Janczarek, M.; Wei, Z.; Raja-Mogan, T.; Endo-Kimura, M.; Khedr, T. M.; Ohtani, B.; Kowalska, E. Morphology- and crystalline composition-governed activity of titania-based photocatalysts: Overview and perspective. ***Catalysts***, 2019, 9(12), 1054; (IF=3.52) selected as ***feature paper***.
3) Raja-Mogan, T.; Lehoux, A.; Takashima, M.; Kowalska, E.; & Ohtani, B. Slow photon-induced enhancement of photocatalytic activity of gold nanoparticle-incorporated titania in-verse opal. ***Chemistry Letter***, 2021 Advance online publication. https://doi.org/10.1246/cl.200804.

Acknowledgement

First and foremost, huge gratitude and thanks to GOD, the almighty for the blessings showered on me throughout these three years of roller-coaster journey to complete my research successfully.

I would like express my genuine appreciation and gratitude to Ohtani sensei (Professor Bunsho Ohtani) for accepting me to be his PhD student in Ohtani labo. A lot of guidance and suggestions have been given by Ohtani sensei and all of those are vital for me to be a better researcher yesterday, today and in the upcoming days. It was a great privilege and honour for me to work under the guidance of him. Next, I would like to thank Ewa sensei (Professor Ewa Kowalska) from my bottom of heart for the unlimited help, guidance, advices in many ways (thesis, publications) throughout my research journey. I learnt a lot and really admire her ways in guiding and teaching me to give out better results in terms of research work and scientific writings. I would like to convey my sincere thanks to Takashima sensei (Dr. Mai Takashima) for her continuous support, guidance and help provided throughout these years.

I am extremely grateful and feel blessed to have my family during my ups and downs. Unlimited thanks and love to my parents (Mr. Raja Mogan and Mrs. Annaletchumy), my grandparents (tata and pati), brother (Trilokesh), sister (Logeswary), aunts and uncles (Letchumy, Jeya Moghan, Tamarai and list goes on), cousins for the continuous support, love and efforts to cheer me up. Love you all eternally. Heartfelt thanks and love to my greatest pillar of support, my fiancée (Mr. Mugilan) for the never-ending motivation, love, trust and support given to me all the seconds, minutes, and hours.

Not forgetting my sister from Thailand (Ing san), Robin, Shaqeer, Alice, Kak sufi, Sherine and lab mates in Japan along with friends in Malaysia for continuous support and motivate me all the time.